Opto-electronic Characterisation of Thin Film Solar Cells with Confocal Microscopy

Xiao Fu

June 2018

A thesis submitted for the degree of

Doctor of Philosophy

in Engineering of

The Australian National University

Australian National University

© Copyright by Xiao Fu 2018

All Rights Reserved

Declaration

I certify that this thesis does not incorporate, without acknowledgement, any material previously submitted for a degree or a diploma in any university, and that, to the best of my knowledge it does not contain any material previously published or written by another person except where due reference is made in the text. The work in this thesis is my own, except for the contributions made by others as described in the Acknowledgements.

Xiao Fu

June 2018

Acknowledgements

I am extremely grateful to Associate Professor Thomas P. White for his guidance in the direction of this research and his encouragement in my life in the last four years. He supported me both mentally and financially to go through the hard time of being a PhD student. It is my fortune to have him as my supervisor. I would also like to thank Prof. Kylie R. Catchpole and A/Prof. Klaus J. Weber for providing helpful advice.

I am very appreciative of my colleagues in the Perovskite group. I would like to thank Dr. The Duong and Dr. Jun Peng for assisting with the fabrication of perovskite films. I also would like to thank Dr. Daniel Jacobs for the productive collaboration of Chapter 5. Many thanks to Dr. Chog Barugkin, Dr. Heping Shen, Dr. Daniel Walter and Dr. Hement Mulmudi for valuable discussion.

I would like to thank Yiliang Wu, Nandi Wu, Ryan Sun, Harry Qian and Dr. Anyao Liu for enjoying the relaxed weekends together and making the PhD life interesting. Sincere thanks to my friends in the PV group, Dr. Di Yan, Dr. Pheng Phang, Dr. Kelvin Sio, Dr. Yimao Wan, Teng Kho, Dr. Hieu Nguyen, and Dr. Azul Osorio Mayon for the fantastic memories. It is my pleasure to work with you.

I would like to give my special gratitude to my best friend Winney Yang for the memorable moments that we shared together in the last eight years. Finally, I deeply thank my parents for their unfailing love and unconditional support. They have provided me through moral and emotional support in my life.

Abstract

The purpose of this work is to develop novel characterisation methods using confocal microscopy to investigate perovskite solar cell materials. It begins with a preliminary study of light management in silicon thin film solar cells for the purpose of demonstrating the capability of confocal scanning microscopy as a solar cell imaging tool. This is followed by several supporting studies to identify the stability of $CH_3NH_3PbI_3$ perovskite materials when exposed to the tightly-focussed, intense laser illumination of a confocal microscope. These studies include: estimation of the laser-induced heating of $CH_3NH_3PbI_3$ films during confocal measurements in order to avoid the effects of thermal-induced degradation during data collection; and measurements of films in different ambient atmospheres, showing that the film must be fully encapsulated by epoxy or kept in N_2 environment to ensure stability during the measurements. PMMA coated perovskite film are shown to be protected from moisture-induced degraded, but they also exhibit an enhancement of photoluminescence (PL) signal under light exposure.

During the PL measurements on $CH_3NH_3PbI_3$ perovskite films, the phenomenon of light- and oxygen-induced PL enhancement was observed, which led to the exploration of trap properties and recombination kinetics of perovskite films. A combination of experimental PL measurements and numerical modelling is used to investigate the dramatic enhancement in PL following prolonged light exposure with timescales ranging from minutes to hours. The time and spatial dependence of the PL enhancement is directly observed by combining localised illumination with PL imaging, which can be explained by a combination of trap de-activation and photogenerated carrier diffusion away from the light-exposed area. Further experiments demonstrate that trap de-activation is reversible once the illumination is turned off. The observed time and spatial dependence of laser induced PL enhancement in $CH_3NH_3PbI_3$ films is modelled, taking into account trap de-activation and carrier diffusion.

Following this topic, a complete physical model of recombination kinetics is implemented to extract recombination coefficients and trap parameters of $CH_3NH_3PbI_3$ and $Cs_{0.07}Rb_{0.03}(FA_{0.85}MA_{0.15})_{0.9}Pb(I_{0.85}Br_{0.15})_3$ perovskite films by fitting to excitation-

dependent steady-state and transient PL measurements simultaneously. Sensitivity analysis shows that fitting a single model to the two different PL measurements provides improved accuracy in multiple-parameter fitting. A comparison of the fitted parameters of the two perovskite films suggests that the improved performance of mixed cation perovskites may result from less active trap states rather than from a lower density of traps. This analysis technique provides a simple, non-contact method to rapidly characterise the key trap properties of perovskite films.

The general recombination model is further used to interpret carrier lifetimes in perovskite films. The origins of bi-exponential transient PL decay observed for many perovskite films are investigated by varying the recombination parameters in the recombination model. This analysis demonstrates that the fast and slow decays in the transient PL curve are dominated by trap-assisted recombination and radiative recombination, respectively. Simulations of the steady-state carrier lifetime as a function of carrier density over a wide excitation range demonstrate that radiative and Auger recombination coefficients could be extracted from experimental measurements at high excitation levels, and trap energy levels can be estimated at low excitation levels. The transient carrier lifetime extracted from the simulated PL decay curve matches the excitation-dependent minority carrier lifetime simulated for steady-state illumination conditions when the excitation level is sufficiently high. Therefore, the transient carrier lifetime extracted from time-resolved PL measurements can be used to estimate radiative and Auger recombination coefficients as long as the carrier density is known during the decay.

This thesis contributes novel characterisation methods based on confocal microscopy for improved understanding of material properties and recombination kinetics of perovskites for photovoltaic applications. Theoretical modelling is performed to support the experimental findings and gain new insights into the detailed chemical and electronic properties of these materials.

Table of Contents

Chapter 1 Introduction

1.1 Motivation

Climate change is one of the greatest challenges of this century. According to the annual statement of global climate published by the World Meteorological Organisation (WMO), the global mean temperature in 2017 was approximately 1.1 °C above the pre-industrial era reaching the warmest on record without an El Niño event [1]. A key driver for global warming is the increasing level of greenhouse gases (CO_2, CH_4, N_2O etc.). Over the past 20 years, fossil fuel burning has produced more than three-quarters of the increase in CO_2 from human activity [1]. Therefore, renewable energy such as solar energy and wind energy are expected to play an important role in minimising greenhouse gases emission.

Photovoltaics (PV) is the most common form of solar energy technology. PV refers to the conversion of light into electricity using solar cells made from semiconductor materials. First-generation conventional solar cells, which currently hold the majority of the global photovoltaic market, are mainly based on crystalline (mono or multi) silicon wafers. The highest efficiency achieved by silicon solar cells has reached 26.6% [2] which is approaching the theoretical maximum of 33% [3] dictated by the detailed balance limit [4]. Thus, the cost reduction of silicon PV modules in consumables and materials is coming to the bottleneck [5]. On the other hand, thin-film solar cells, which are made by depositing one or more thin layers of photovoltaic material on to a substrate, are classified as the second-generation solar cells. Thin-film technologies effectively reduce the material consumption, and hence lower the price; however, the efficiency of commercial thin film solar cells is lower compared to the first-generation solar cells [2]. Finally, third-generation photovoltaic cells are solar cells that could overcome the detailed balance limit including multi-layer (“tandem”) cells, quantum dot and hot-carrier cells.

Reducing the cost of commercial PV systems by reducing consumables is difficult; therefore, improving the performance of the solar cells becomes significant for further cost reduction [5]. Carrier generation and recombination are the two fundamental

processes that ultimately determine the performance of a solar cell. Improving the efficiency of solar cells requires either more charge carriers to be generated, and/or less recombined. There are many advanced techniques that have been applied to characterise solar cells or semiconductor thin films. Confocal microscopy is a frequently-used technique for characterising the optoelectronic properties of solar cells [6-8]. The reflected light or fluorescence from an illuminated sample is collected by the objective and is focussed through a pinhole at the front of the detector in order to eliminate the out-of-focus signal. This approach greatly improves the resolution and contrast of the optical signal compared to standard optical microscopy. In addition, the confocal laser scanning microscope has a potential to generate high resolution images of the detected area. Thus, it allows us to visually analyse the optoelectronic properties of semiconductor materials. For example, confocal photoluminescence (PL) measurements can be used to quantitatively analyse the efficiency of radiative recombination, which has a direct impact on the maximum open-circuit voltage attainable in a solar cell.

Mentioning the improvement of solar cell efficiency, an emerging photovoltaic technology based on organic-inorganic hybrid perovskite materials has received tremendous research attention. The perovskite materials used in these cells are structured compounds with the chemical composition ABX_3 (A = Cs^+, Rb^+, $CH_3NH_3^+$ (methylammonium cations or MA), or $CH(NH_2)_2^+$ (formamidinium cations or FA); B = Pb^{2+} or Sn^{2+}; X = I^-, Br^-, or Cl^-). In 2009, $CH_3NH_3PbI_3$ perovskite was first applied to solar cells with an efficiency of 3.8% [9]. Since then, the performance of hybrid lead halide perovskite solar cells has improved dramatically, leading to the current efficiency record of 22.7% in late 2017 [2]. This rapid improvement has been driven by developments in several research areas including cell structure, deposition methods, material composition and understanding of perovskite material properties.

However, as a new photovoltaic material, the semiconductor properties and recombination kinetics of perovskites are still not well understood. This thesis focuses on applying the confocal microscopy technique to understand the optical and electrical properties of thin film solar cells, especially the recombination kinetics of perovskite

materials. This study aims to provide new insights into the characterisation of perovskite films for a better understanding of perovskite solar cell performance.

1.2 Thesis Outline

When this thesis commenced in 2014, the original objective was to develop novel characterisation methods using confocal microscopy to investigate light management of thin film solar cells (initially thin-film Si cells, as discussed in Chapter 4). In 2014, since the research focus of the whole group turned to perovskite solar cells, a detailed stability test of $CH_3NH_3PbI_3$ films was performed as preparation for obtaining reliable and trustworthy characterisation results of the optical and electrical properties of perovskite solar cells. During the PL measurements on $CH_3NH_3PbI_3$ perovskite films, a light- and oxygen-induced PL enhancement was observed, which led to the exploration of trap properties and recombination kinetics of perovskite films, as described in Chapter 5. In exploring this topic further, a complete physical model of the recombination kinetics was implemented to extract the recombination parameters of perovskite films by simultaneously fitting the model to excitation-dependent steady-state and transient PL measurements (Chapter 6). This model was also used to interpret carrier lifetime in perovskite films (Chapter 7).

The thesis is divided as follows:

- In Chapter 1, the motivation of this thesis and the general background of photovoltaics is introduced.
- Chapter 2 starts with a review of high-resolution confocal microscopy and its application to solar cell characterisation. Then, the challenges of characterising perovskite materials are discussed particularly with respect to their instability against moisture, high temperature, light and oxygen. However, light and oxygen also have a potential to enhance the performance of perovskite solar cells. To investigate the dynamics of carriers and traps in perovskite materials, the measurements of carrier diffusion and trap properties in perovskites are reviewed. Trap states in perovskite films are important for understanding the recombination kinetics of perovskites, and a review of discussion on the recombination kinetics is provided. Finally, measuring and interpreting carrier

lifetime of silicon wafer are reviewed in order to replicate this study for perovskite films.

- Chapter 3 describes the methodology of all the experiments that have been performed in this study, including sample fabrication, characterisation and modelling.
- Chapter 4 describes a series of preliminary and supporting studies carried out in the early stages of this thesis. These are: i) experiments to evaluate the capability of confocal microscopy/scanning photocurrent measurements to spatially-resolve plasmonic light trapping in silicon thin film solar cells; ii) modelling of the laser-induced temperature rise on samples as a way to identify whether temperature is a major factor in the experiments; and iii) stability test of $CH_3NH_3PbI_3$ films under different ambient.
- Chapter 5 applies confocal PL microscopy to investigate the time and spatial characteristics of light-induced and oxygen-assisted trap de-activation in $CH_3NH_3PbI_3$ perovskite films. A model of recombination kinetics based on rate equations is applied to simulate the observed effect.
- Chapter 6 presents a method to quantify the quality of perovskite films using a combination of steady-state and transient photoluminescence measurements. The combined experimental data sets are fitted using a single, general recombination model, from which detailed trap and recombination parameters can be extracted, and the accuracy of the fitted values estimated. This approach expands the application of confocal photoluminescence measurements to include quantitative evaluation of the most relevant defect characteristics, including trap density, energy level and carrier capture coefficients.
- Chapter 7 investigates the physical origins of the bi-exponential decay observed in time-resolved PL measurements on perovskite films. The general recombination model is applied to investigate the relationship between excess carrier density and carrier lifetime in different conditions to provide an interpretation of the measured PL lifetime of perovskite films.
- Finally, a conclusion of the thesis is made in Chapter 8 along with an outlook of future work that can be continued in this field.

Chapter 2 Literature Review

This chapter first introduces confocal microscopy as a technique for solar cell characterisation, and the development of perovskite solar cells. Then, stability studies of perovskites and the dynamics of carriers and traps in perovskite materials are reviewed. Finally, different interpretations of recombination rates and carrier lifetimes are discussed with respect to the recombination mechanisms of perovskites.

2.1 Confocal microscopy

The confocal scanning microscope was first invented by Marvin Minsky in 1955 [10]. It is an optical imaging system which incorporates a point-by-point illumination source such as laser, and a pinhole at the front of the detector where the reflected light or fluorescence is collected. This configuration ensures that only the light emitted from the focus plane is detected, and any out-of-focus signal is eliminated (Figure 2.1). This approach improves the optical resolution and contrast of the scanned image with respect to the standard optical microscope [11].

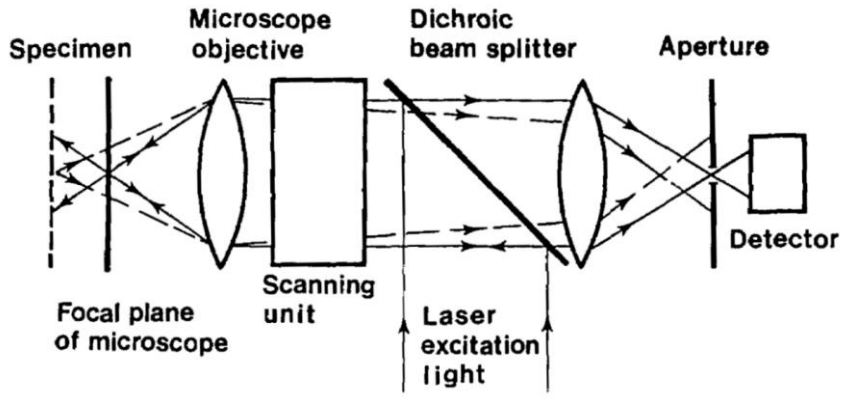

Figure 2.1 Principle setup of a confocal microscope. (Adapted from [11])

With the development of nanotechnology in solar cells, confocal microscopy has been widely used to characterise photovoltaic devices for investigating the optical and electrical effects introduced by nanostructures. For example, confocal reflectance mapping has been applied to study the local light harvest associated with surface texturing or nanoparticles [6]. Confocal microscopy is also used in other techniques that require a focussed laser beam and a precise signal, such as photoluminescence [7] and Raman [8] spectroscopies. In this thesis, all the measurements are performed

using confocal microscopes, including confocal reflectance and photocurrent mapping of a silicon thin film solar cell (Chapter 4); confocal Raman spectra measured on $CH_3NH_3PbI_3$ films (Chapter 4); confocal PL measurements on perovskite films including the extraction of PL spectra, PL intensity, PL images, and PL lifetime (Chapter 4 - 6).

2.2 The history of perovskite solar cells

As introduced in Chapter 1, the first perovskite solar cell was invented in 2009 by Kojima et al. with 3.8% conversion efficiency. This cell utilized lead halide perovskite as a sensitizer in a dye sensitized solar cell (DSSC) with liquid electrolyte [9]. In 2011, Park et al. improved the efficiency of perovskite DSSC to 6.5% by fabricating 2-3 nm sized perovskite nanoparticles on TiO_2 thin film [12]. This same group, in the next year, replaced the liquid electrolyte of the perovskite solar cell by solid hole transport material – Spiro-MeOTAD, which led to a much more stable solar cell with an efficiency of 9.7% [13]. Since then, the development of solid-state perovskite solar cell begins. Within nine years, the conversion efficiency of perovskite solar cells has been boosted up to 22% [2].

Most of the high efficiency perovskite cells utilize a mesoporous structure, where perovskite is filled into TiO_2 scaffolds [14-16]. This configuration is supposed to increase the contact area between active layer and electron transport material (ETM), as a result, the electron collection could be more efficient. However, the planar structured perovskite solar cells also achieve a high efficiency (15%) [17], which indicates that the planar perovskite film itself has excellent opto-electronic properties. In the followed chapters, planar perovskite films are characterised to evaluate the material properties of perovskites.

Since perovskite is the catch-all term for a group of materials with the same crystalline structure, the actual composition of perovskites in the reported perovskite cells are quite different. Researchers develop perovskite films with different cations and halides in order to increase the efficiency, improve the cell stability, and tune the absorption wavelengths [18-22]. Thus, comparing perovskite films with different composition may provide some suggestions of improving perovskite solar cell efficiency. In Chapter 6, $CH_3NH_3PbI_3$ and $Cs_{0.07}Rb_{0.03}(FA_{0.85}MA_{0.15})_{0.9}Pb(I_{0.85}Br_{0.15})_3$ perovskite films are

investigated. The underlying reasons of the better performance for the mixed cation perovskite cells are discussed.

It is known that the regular structure of perovskite solar cells is n-i-p structure, the efficiency of devices with this structure have reached over 20% [23]. In recent years, the inverted structured (p-i-n) perovskite solar cells have gained attention due to their easy-fabrication, compatibility with flexible substrates, suppressed hysteresis characteristics, and potential of fabricating multijunction cells [24-28]. The inverted planar heterojunction perovskite solar cells even achieved a stabilized 21%, with a high open-circuit voltage of 1.21 V [28]. This further makes the investigation of the recombination kinetics of planar perovskite films become more and more attractive.

2.3 The challenges of characterising perovskite solar cells

A key focus of this thesis is the PL measurement of perovskite films for characterising the optical and electrical properties of perovskites and potentially improving the efficiency of perovskite solar cells. However, stability is a major issue in the development of perovskite solar cells [29, 30], and impedes the characterisation of perovskite samples. Ledinský once pointed out that some reported Raman spectra of perovskite films were measured on degraded samples [31]. On one hand, perovskite solar cells generally undergo rapid degradation on exposure to moisture, high temperature, UV light and oxygen [29, 30, 32-38]; on the other hand, some post-treatments of light and oxygen has been shown to benefit the performance of perovskite films [39-46].

2.3.1 Degradation

Moisture induced degradation

Moisture is the most common factor that induces the degradation of perovskites [32-34]. The first step of the moisture induced degradation of $CH_3NH_3PbI_3$ is the perovskite hydration process rather than simply resulting in PbI_2, which produces monohydrate $CH_3NH_3PbI_3{\cdot}H_2O$. Then, the dihydrate $(CH_3NH_3)_4PbI_6{\cdot}2H_2O$ can be produced by additional hydration with the formation of PbI_2 (see Equation 2.1) [32, 33].

$$\begin{aligned} 4(CH_3NH_3)PbI_3 + 4H_2O &\rightleftarrows 4[(CH_3NH_3)PbI_3 \cdot H_2O] \\ &\rightleftarrows (CH_3NH_3)_4PbI_6 \cdot 2H_2O + 3PbI_2 + 2H_2O \end{aligned} \quad 2.1$$

The decomposition of perovskite is a reversible reaction; however, the migration of metal halide may lead to device degradation [47]. Density functional theory analysis further proves that the reason for moisture induced degradation is the reduction of hydrogen bonding between PbI_6 and $CH_3NH_3^+$ cation [48]. Moreover, the humidity level directly affects the rate of degradation. For example, the perovskite films fabricated by Yang *et al* can survive tens of days under 50% relative humidity level and less than 3 days under 80% relative humidity level [34].

Temperature induced degradation

Thermal annealing is always required during the fabrication of perovskite films to improve the crystallinity [49]. However, post-treatment of perovskite films with high temperatures will induce degradation. In high resolution characterisation of perovskite thin films, a focussed laser beam is usually applied to generate an opto-electronic response. This may introduce strong local heating of the thin film, which acts as localised post-annealing. Therefore, thermal stability of perovskite thin films should be considered during the characterisation. The thermal instability of $CH_3NH_3PbI_3$ perovskite may originate from two aspects. One is its irreversible phase transition from tetragonal to cubic at around 57 °C [30]. This phase transition is expected to have a negative impact on the photovoltaic performance of perovskite solar cells [50]. Another is the temperature induced decomposition of $CH_3NH_3PbI_3$, which forms CH_3NH_2, HI and PbI_2 [38]. These constituents have poor optical and electrical behaviours.

The required ambient temperature of thermal induced degradation can be analysed by calculating the formation energy of perovskite polycrystals per unit cell. When the thermal energy of ambient temperature is higher than the crystal formation energy, the degradation of the perovskite film is very likely to occur [51]. Furthermore, the thermal conductivity of hybrid metal halide perovskites is quite low. This may lead to a slow distribution of heat across the film and concentrated heating in localised regions, which increases the potential of temperature induced mechanical stress [52].

UV light induced degradation

Perovskite solar cells tend to degrade even under AM1.5G, 1-Sun illumination. The commonly used electron transport layer TiO_2 in perovskite solar cells might be the reason for the light induced degradation, as it is photocatalytically active under UV light [35]. Thus, UV induced degradation of perovskite solar cells can be considered as the surface chemistry associated with TiO_2.

For the perovskite bulk layer, $CH_3NH_3PbI_3$ can also be broken down into PbI_2 irreversibly under UV illumination [36, 37, 49]. In addition, exposing the Pb-X bond in organolead halide perovskite materials ($MAPbX_3$) leads to a breakdown into dihalogens (I_2, Br_2, and Cl_2) due to the generation of halogen free radicals. The well-ordered inorganic matrix formed by inorganic Pb^{2+} and X^- even enhances the absorption and re-emission of light [29]. Therefore, halogen elimination might be another possible reason for the light-induced degradation of perovskite solar cells.

Oxygen induced degradation

The presence of UV illumination can also promote reactions between oxygen and organic molecules, forming peroxide or superoxide compounds [53-55]. Those compounds result in the decomposition of perovskite active layers. This process was introduced as the UV and oxygen induced degradation of perovskite solar cells.

2.3.2 Enhancement of opto-electronic performance

On the other hand, certain post treatment on the as-prepared perovskite solar cells or perovskite films could benefit their photovoltaic performance.

Light soaking

The post-treatment of solar cells under a certain amount of light exposure for improving cell performance is the so-called light soaking process. As shown in Figure 2.2, the measured device parameters of an as-prepared organic solar cell with a structure of ITO/TiO_x/P3HT:PCBM/PEDOT:PSS/Ag[1] exhibited an S-shape J-V curve with an extremely low fill factor (Fig. 2(a) in [56]). However, after 20 minutes white light illumination, the fill factor, as well as the open-circuit voltage, were both dramatically

[1] ITO stands for Indium tin oxide; P3HT stands for Poly(3-hexylthiophene); PCBM stands for Phenyl-C_{61}-butyric acid methyl ester; PEDOT:PSS stands for poly(3,4-ethylenedioxythiophene) polystyrene sulfonate.

improved [56]. The shape of J-V curve also recovered back to that expected for this type of solar cells (see the red curve in Figure 2.2). This light soaking phenomenon has been observed in organic solar cells, where photo-induced rearrangement of Fermi levels could occur at the TiO_x and ITO interface [56].

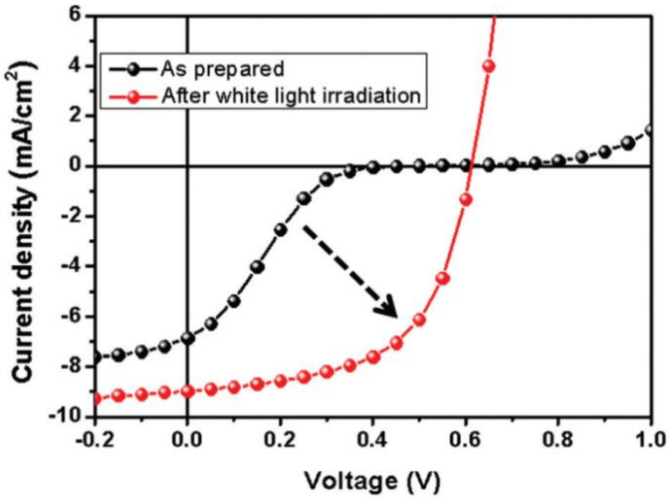

Figure 2.2 The J-V characteristics of polymer solar cells before (black) and after (red) white light irradiation. (Adapted from [56])

TiO_x and ITO are also commonly used in perovskite solar cells as the electron transport material and the cathode, respectively. Thus, light soaking effect has also been observed in perovskite solar cells using TiO_2 as electron transport material [39, 40]. It is demonstrated in Figure 2.3 that the efficiency of an as-prepared perovskite solar cell with the configuration of FTO/bl-TiO_2/mp-TiO_2/$CH_3NH_3PbI_3$/Spiro-MeOTAD/Ag[2] was almost doubled after 15 minutes of light soaking effect (FIG. 2 in [39]). This enhancement of device performance was shown to be partially irreversible since the efficiency remained at 70% of the maximum after storing the device in the dark for 4 days (Figure 2.3d).

[2] FTO stands for fluorine doped tin oxside; bl stands for blocking layer; mp stands for mesoporous; Spiro-MeOTAD stands for 2,2',7,7'-Tetrakis-(N,N-di-4-methoxyphenylamino)-9,9'-spirobifluorene.

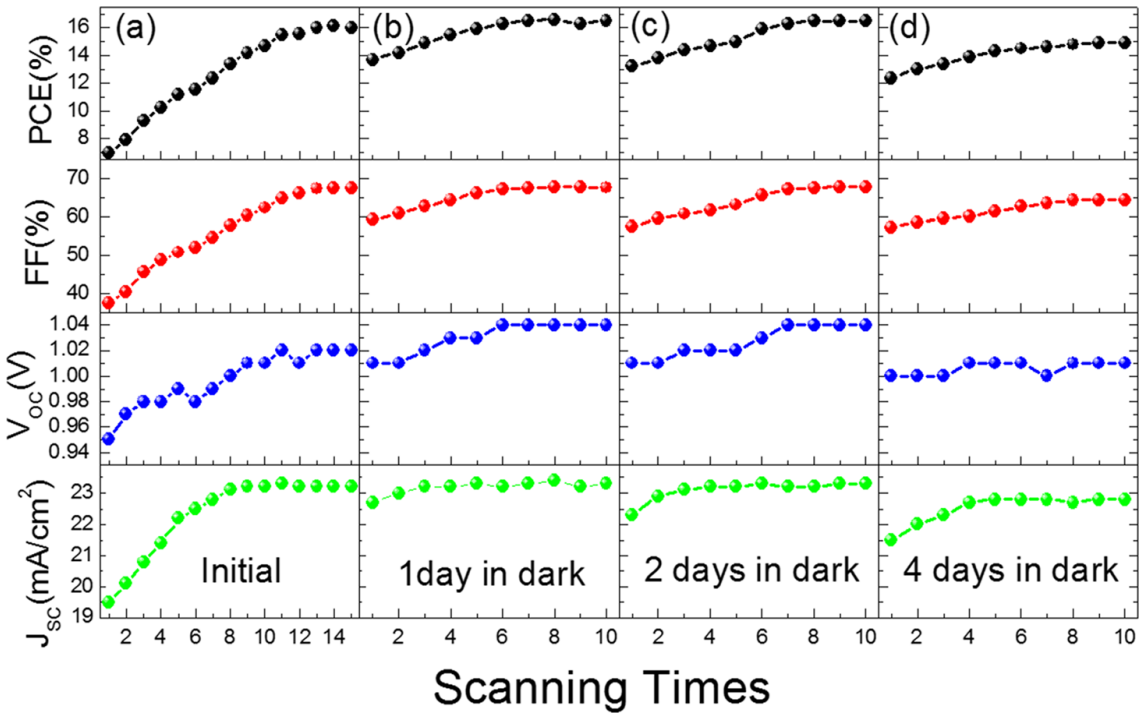

Figure 2.3 Relationship between the performance parameters (from top to bottom: PCE, FF, V_{OC}, and J_{SC}) and scanning times obtained in: (a) fresh device and the same device stored in the dark for (b) 1, (c) 2, and (d) 4 days. (Adapted from [39])

With further investigation, Liu *et al* indicated that light exposure could increase the concentration of oxygen vacancies in TiO_2, which is analogous to an increase of doping density in conventional semiconductors [39]. As a result, the conductivity of TiO_2 layer, as well as the charge extraction rate at the mp-TiO_2/perovskite interface could be enhanced, which eventually led to an improvement in power conversion efficiency of the perovskite solar cell.

Combining the PL intensity and lifetime measurements of perovskite solar cells along with the standard J-V measurements under different light exposure conditions, Deng studied the light soaking phenomenon of perovskite solar cells from the perspective of ion migration and accumulation [40]. Figure 2.4 shows the time-dependent J-V curves after light soaking process in (a) open-circuit and (b) short-circuit conditions (Fig. 2b and 6b in [40]). The small light soaking effect on the J-V curves in the short-circuit condition implied that this light induced enhancement of perovskite solar cells can be associated with ion migration, because no electric field was applied to the solar cell. Deng *et al* concluded that positive ions such as iodide vacancies were accumulated near the interface between the hole transport layer and the perovskite bulk layer in the as-prepared solar cells, which resulted in a reduction of charge carrier separation.

Thus, the surface recombination is increased, and the performance of the perovskite solar cell is suppressed. Light soaking effect could effectively enhance ion migration under an electric field (open-circuit condition), where the positive ions drift away from the spiro-MeOTAD/perovskite interface, leaving behind negative ions which accumulate at that interface [40].

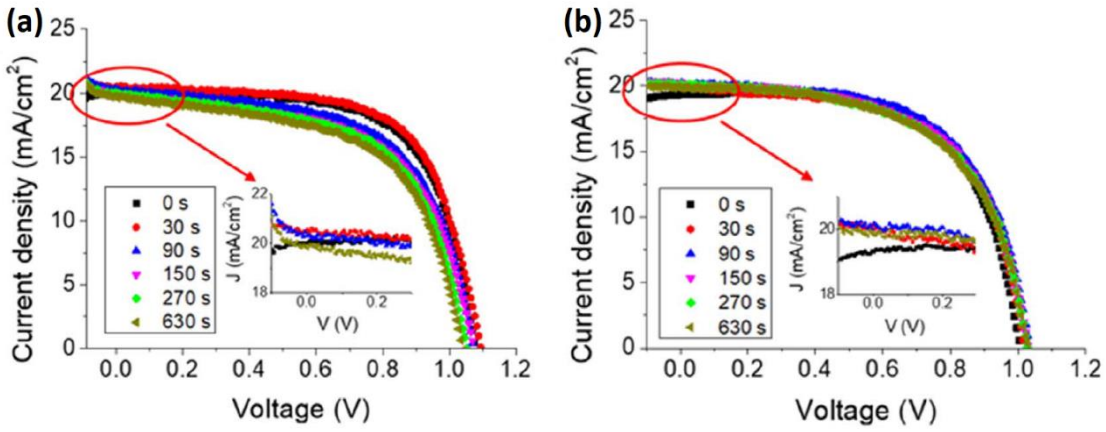

Figure 2.4 J-V measurements for $CH_3NH_3PbI_3$ solar cells light soaked in (a) open-circuit and (b) short-circuit conditions. (Adapted from [40])

Oxygen-related PL enhancement

Apart from the effects on the interfaces of the perovskite solar cells, light-induced enhancement on perovskite films has also been observed by comparing the PL intensity and lifetime under different atmospheres [41, 42]. Figure 2.5 demonstrates the time-dependent PL intensity of $CH_3NH_3PbI_3$ films measured in air, nitrogen gas and oxygen gas environment in a sequence. After a rapid increase in the first 2 minutes, the PL intensity of perovskite film measured in air dropped back for over more than 10 minutes. Changing the measurement atmosphere to N_2, the PL intensity was slightly recovered and then stabilised. Moving the stable perovskite film into an O_2 environment, the measured PL intensity of perovskite film still increased up to 1500 counts with much a slower drop off afterwards [41]. The fast reduction of PL intensity measured in air could result from the moisture induced degradation of perovskite films, as mentioned above.

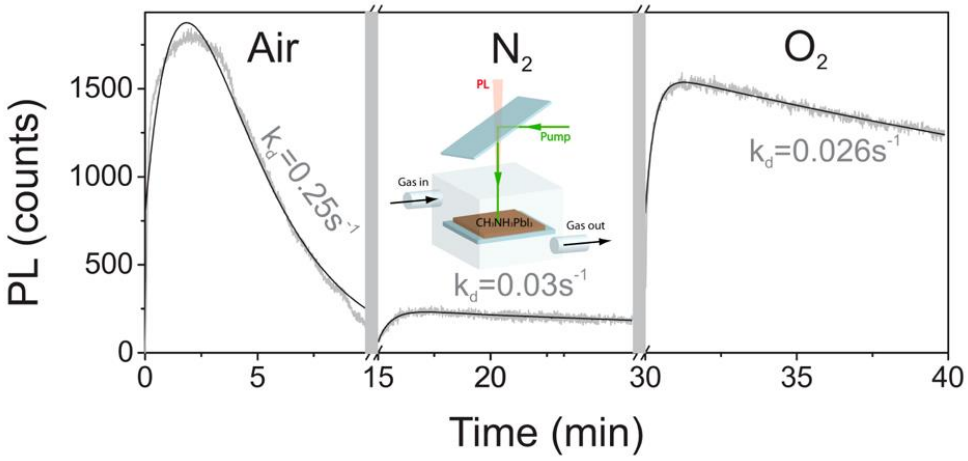

Figure 2.5 Evolution of the PL intensity with the sample exposed to different atmospheres – air, N_2 and O_2. Grey (black) curves correspond to experimental data (fits). (Adapted from [41])

Tian also measured the PL lifetime of perovskite films during the period of PL intensity enhancement [42]. The effective carrier lifetime of $CH_3NH_3PbI_3$ perovskite films increased from a few nanoseconds to hundreds of nanoseconds over 5 minutes under illumination (Figure 2.6). This work indicated that the non-radiative recombination rate of the light-exposed perovskite film can be effectively reduced due to the removal of trapping sites assisted by the photochemical reaction involving oxygen [42].

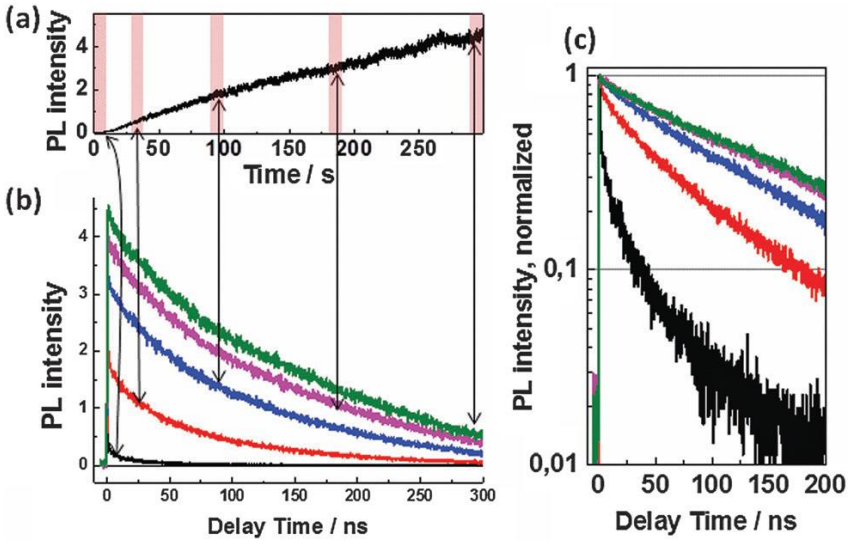

Figure 2.6 (a) Steady-state PL intensity as a function of light exposure time. (b) The corresponding PL decays through the enhancement process measured at the indicated times. (c) The same data of (b) on the logarithmic scale. (Adapted from [42])

The origins of oxygen-assisted light-induced PL enhancement observed on perovskite films have been investigated by many researchers. It has been suggested that oxygen molecules could react with trapped photocarriers which may de-activate the traps. With effective defect passivation, trap-assisted recombination could be reduced to

enhance the band-to-band radiative recombination [41-43]. The de-activated traps were specified to be surface traps according to the investigation of the PL enhancement on $CH_3NH_3PbBr_3$ single crystals due to the limited penetration of oxygen gas into perovskite crystals [44]. In a study of oxygen-induced enhancement of perovskite PL quantum yield, the de-activation mechanism of deep traps was proposed and modelled by density functional theory. It was suggested that stable oxidised products were formed due to the reaction between oxygen molecules and iodide interstitials [45]. However, this result was not in agreement with the reversible process of trap passivation observed in previous studies [41-44]. Meggiolaro also suggested a method to experimentally detect the oxidised defect products using vibrational analysis in the 300-700 cm^{-1} frequency range [45].

A detailed study was also carried out to investigate oxygen related PL enhancement in perovskite single crystals using confocal fluorescence microscopy [46]. The time- and depth-dependent PL intensity of perovskite single crystals were measured at different excitation wavelengths, excitation energies and gas environments. Similarly, it was concluded that the PL intensity of perovskite materials could be enhanced by the exposure of light and oxygen. Moreover, it indicated from the depth-dependent PL measurement that the dominant mechanism for oxygen related PL enhancement was the penetration of oxygen species instead of the diffusion of oxygen gas. Therefore, unlike superoxide-induced degradation described in Section 2.3.1, Feng proposed that the superoxides O^{2-} formed from the reaction between O_2 and free carriers could passivate the defects in perovskites in order to enhance the radiative recombination [46].

From the investigation of the reversible oxygen assisted PL enhancement of perovskite materials, Stoeckel proposed the application of perovskite devices as oxygen sensors [57]. The first reversible, fast and wide-range perovskite oxygen sensor was demonstrated in ref. [57] through the measured current of this device (Figure 2.7).

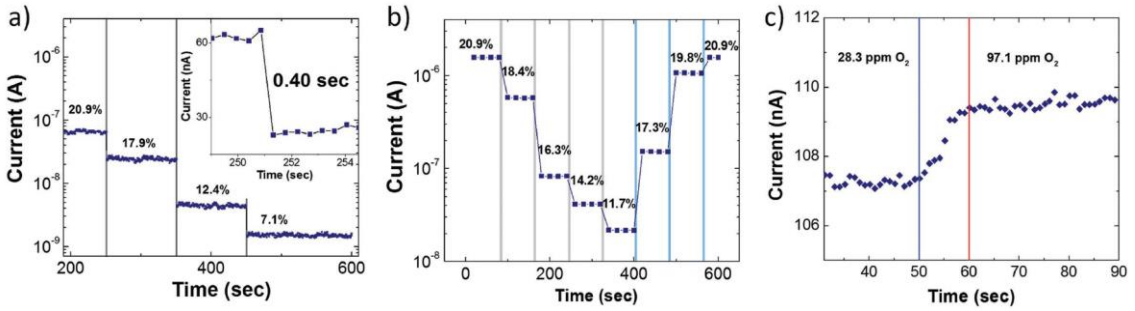

Figure 2.7 (a) Real time change in the current measured in a perovskite film in response to O_2 concentration. Inset: speed of the sensor response. (b) Reversibility of the sensor. The O_2 concentration is initially decreased from 20.9% to 11.7% and then increased back to 20.9%. (c) Fast response of the sensor. The blue line indicates the instant in which oxygen gas is introduced in the chamber. After this moment, the oxygen content in the proximity of the sample increases slowly until it reaches an equilibrium state (marked by the red line). (Adapted from [57])

As discussed above, the stability of perovskite materials is a big issue in characterisation. A detailed stability test of the perovskite films fabricated in our lab has been demonstrated in Section 4.3. To investigate the optical and electrical properties of those materials, one has to ensure that the samples are measured in a controlled environment, for example nitrogen atmosphere, where the detected parameters are not affected by the ambient during the experiment. The perovskite samples measured in Chapter 5 and 6 are protected from degradation during the measurements. Moreover, the investigation of the transient behaviours of perovskite materials, for instance the PL enhancement caused by light and oxygen, is also an important field in characterising perovskite materials, and is discussed in detail in Chapter 5.

2.4 Properties of carriers and traps

During the investigation of PL enhancement in perovskites, a lateral extension of PL enhanced area is observed from the confocal PL images (Chapter 5). To understand the cause of the spreading PL signal, the dynamics of carriers and traps inside the materials should be studied. The following section reviews the measurements of carrier diffusion length and trap properties on perovskite single crystals and/or films.

2.4.1 Carrier diffusion

It is known that the diffusion length (L_D) of photogenerated carriers depends on the carrier mobility (μ) and carrier lifetime (τ)

$$L_D = \sqrt{D\tau} = \sqrt{\frac{\mu k_B T}{q}\tau}, \qquad 2.2$$

where D is the diffusivity, k_B is Boltzmann constant, T is the absolute temperature and q is the electric charge.

Time-of-flight methods have been frequently used to measure the drift mobility of minority carriers in semiconductors [58-62]. A detailed configuration of the measurement is discussed in [63]. This method has been applied to the measurements of carrier mobility on perovskite single crystals [62, 64]. The carrier lifetime of perovskites can be measured through time-resolved PL decay [62, 64-66]. Thus, the carrier diffusion length in perovskite single crystals can be calculated using Equation 2.2. The reported diffusion length was around 175 µm for the $CH_3NH_3PbI_3$ single crystals grown by solution-growth [64].

Unlike perovskite single crystals, perovskite thin films used in solar cells are polycrystalline in most cases. Thus, the carrier diffusion length in perovskite films should be much shorter than that in perovskite single crystals. Handloser directly observed the carrier diffusion by extracting PL images using a time-resolved laser scanning confocal PL microscope [67]. The schematic in Figure 2.8 illustrates the experimental approach: the excitation was fixed at the centre of scanned area, while the PL intensity was detected by scanning across the film. Therefore, the carrier diffusion length of perovskite films could be roughly estimated by the furthest distance from the centre where a PL signal could still be detected [67].

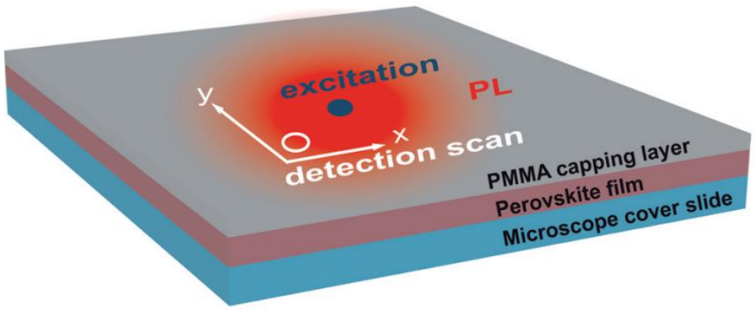

Figure 2.8 Schematic illustration of the experimental approach and the sample layout. In detection scans, the excitation and sample position are fixed while the detection is scanned. PL (red area) observed at remote detection areas clearly indicates charge carrier transport within the film. (Adapted from [67])

In addition, the steady-state photocarrier grating (SSPG) technique introduced by Adhyaksa has also been used to extract carrier diffusion length in perovskite films [68]. This technique detects the change in photoconductivity associated with a periodic optical grating created by two interfering laser beams. By solving the one-dimensional steady-state diffusion equation (Equation 2.3), it was found that the photoconductivity is strongly related to the laser grating period, and the carrier diffusion length (L_D) could be directly extracted from the gradient of $\left(\frac{1}{1-\beta}\right)^{1/2}$ as a function of $\left(\frac{1}{\Lambda}\right)^2$ (Figure 2.9), where β is the ratio between photoconductivity with and without grating, Λ is the period of laser grating and Z is a fitting parameter associated with the grating formation.

$$\left(\frac{1}{1-\beta}\right)^{1/2} = \frac{(2\pi L_D)^2}{(2Z)^{1/2}}\left(\frac{1}{\Lambda}\right)^2 + \frac{1}{(2Z)^{1/2}} \qquad 2.3$$

Carrier diffusion lengths of a few hundred nanometres were estimated for $CH_3NH_3PbI_3$ and $CH_3NH_3PbBr_3$ perovskite films using this method (see Figure 2.9) [68]. However, the limitation of this method is that conductivity measurements require a bias voltage to be applied across the film, which may introduce ion migration [69].

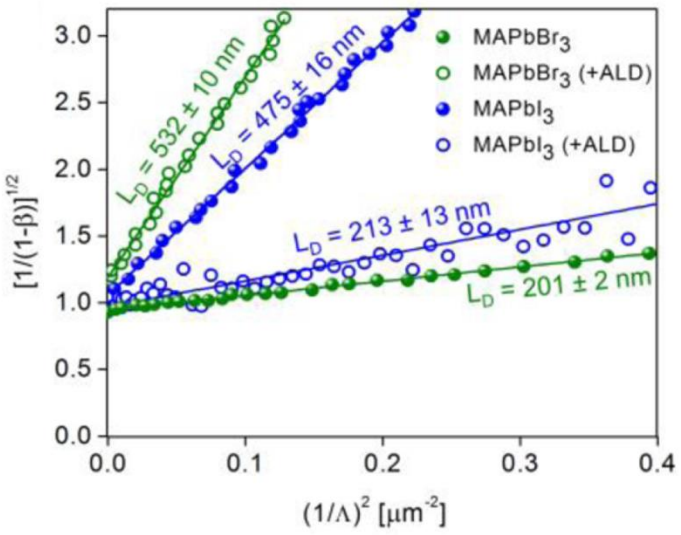

Figure 2.9 Experimental data of a transform of the photoconductivity ratio (β) as a function of grating period (Λ) before (filled dots) and after (unfilled dots) passivation measured on $MAPbBr_3$ (green dots) and $MAPbI_3$ (blue dots) samples. The lines are the linear fitting of each corresponding data. (Adapted from [68])

Moreover, Webber *et al* applied the femtosecond four-wave mixing (FWM) method on perovskite films to measure the diffusion length of photocarriers [70]. In the

experiment, three noncollinear optical pulses were focussed on to the sample as demonstrated in Figure 2.10.

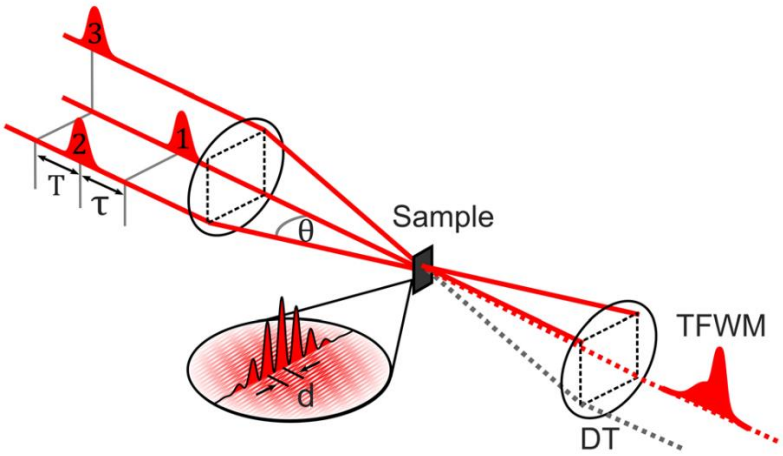

Figure 2.10 Schematic diagram of the FWM setup. (Adapted from [70])

The interference between pulse 1 and pulse 2 generate a periodic spatial modulation of carrier density, forming a transient grating. Pulse 3 is then used to detect the diffracted signal as a function of delay time T between pulse 2 and 3. Thus, the intensity of FWM signal (I) depending on the delay time can be expressed as

$$I(T) \propto \exp(-T/T_s). \tag{2.4}$$

T_s is the time constant extracted from the exponential decay of the FWM signal (Figure 2.11a) for the corresponding grating constant $d = \frac{\lambda}{2\sin\theta/2}$, where λ is the laser wavelength and θ is the angle between the focussed pulse 1 and 2. The decay constant T_s can also be determined by

$$\frac{1}{T_s} = \frac{2}{T_L} + \frac{8\pi^2 D}{d^2}, \tag{2.5}$$

where T_L is the carrier lifetime and D is the carrier diffusivity. Therefore, by plotting the extracted decay constant T_s as a function of the laser grating for the corresponding FWM decay measurement, the carrier lifetime and diffusivity can be extracted from the vertical intercept and gradient of the line, respectively (Figure 2.11b) [70].

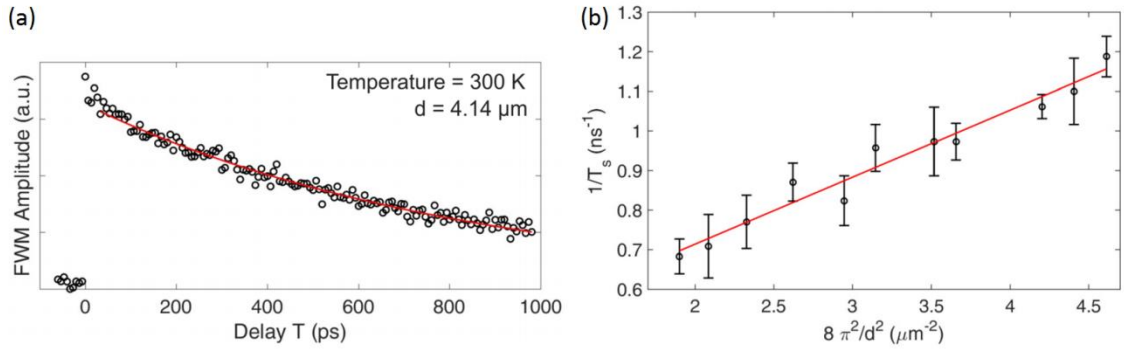

Figure 2.11 (a) FWM signal as a function of delay time T at 300 K for d = 4.14 µm. The solid curve is a least-square fit to Equation 2.4. (b) Inverse signal decay time $1/T_s$ as a function of $8\pi^2/d^2$ measured at 300 K. The solid line is a fit of the data to Equation 2.5. (Adapted from [70])

This method of determining carrier diffusion is non-contact, and hence eliminates the interference from interfaces and avoids the impact of an electric field. The carrier diffusion length of solution-processed $CH_3NH_3PbI_3$ films measured in this work was around 0.95 ± 0.07 µm [70].

2.4.2 Trap density, trap energy levels and capture cross-section

Many different methods have been used to measure the trap density, trap energy levels and capture cross-section of electrons and holes in perovskite materials. Temperature derivative capacitance-frequency measurement is used to determine the trap density in amorphous silicon solar cells [71]. Fitting the results of PL lifetime and PLQE measurements to a recombination model provides an estimation of the trap density in perovskite films [72, 73]. In this section, the methods that are commonly applied to directly measure trap properties of perovskite films are reviewed and the parameter extraction from model fitting are discussed along with the recombination kinetics of perovskites in Section 2.5.2 and 2.5.3.

The density of traps in perovskite solar cells can be determined by thermal stimulated current (TSC) analysis [74-76]. In this method, a temperature-dependent current was measured inside a vacuum chamber, giving a spectrum of thermal stimulated current. The trap density is estimated from the integration of measured spectrum (Figure 2.12a), and the TSC spectrum was then fitted to several Gaussian distributions in order to identify different trap states (see the peaks in Figure 2.12a). For each type of traps, the activation energy (E_a) can be extracted from the Arrhenius plot $k = Ae^{\frac{-E_a}{k_B T}}$ (Figure

2.12b), where k is the rate constant, A is the pre-exponential factor, k_B is the Boltzmann constant and T is the absolute temperature (in Kelvin).

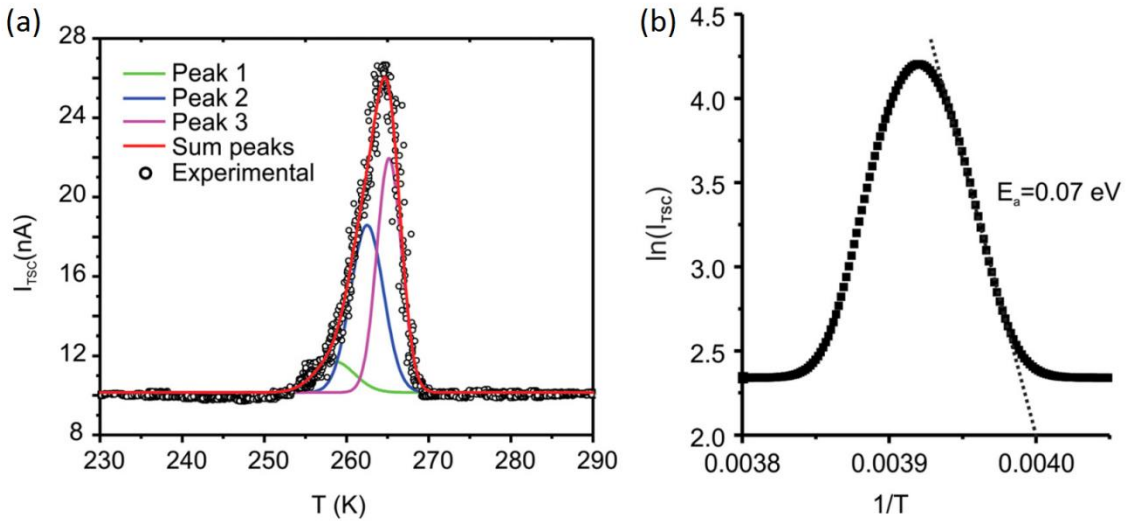

Figure 2.12 (a) Deconvolution of the TSC curve obtained from measurements. The red line is the sum of the three peaks used to deconvolute the experimental TSC curve. (b) Arrhenius plot showing the activation energy. (Adapted from [74])

On the other hand, capacitance measurements have been applied to determine the relative dielectric constant of perovskite solar cells [76]. At low frequencies, all traps should respond to an applied voltage. Thus, the saturated capacitance, which implies that the depletion region has extended to the interface, is given by $\varepsilon A/t$ (t is the thickness of perovskite layer, A is the measured area and ε the dielectric constant). From the result plotted in Figure 2.13, Samiee determined that the relative dielectric constant of $CH_3NH_3PbI_xCl_{3-x}$ perovskite solar cells was around 18 [76]. Therefore, the capture cross-section of traps can be estimated from the static dielectric constant using a Coulomb model [77].

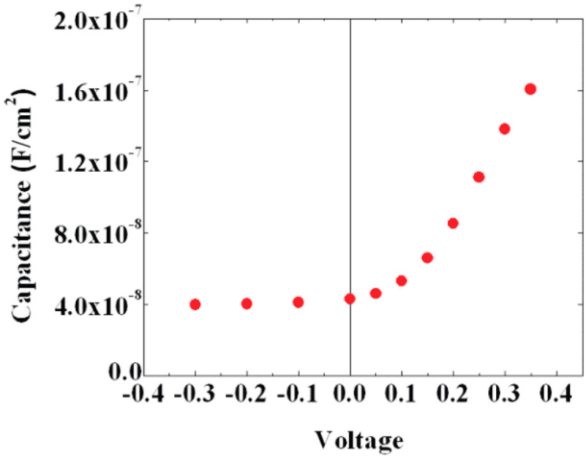

Figure 2.13 Capacitance vs. voltage data under forward and reverse bias. (Adapted from [76])

2.5 The interpretation of recombination rates

Theoretical analysis of the recombination rates has been used to explain oxygen-assisted light-induced PL enhancement in perovskite films (Chapter 5), which encouraged the investigation of recombination kinetics in perovskites through PL measurements. The estimation of parameters associated with traps has been reviewed previously in Section 2.4.2. In this section, the interpretation of recombination rates extracted from both steady-state and transient measurements on perovskites will be discussed.

The two types of recombination mechanisms in semiconductor materials include radiative recombination and non-radiative recombination (trap-assisted recombination and Auger recombination). Suppressing the non-radiative recombination in perovskite layer is clearly beneficial; however, before optimising the bulk material, it is necessary to evaluate the rates of each recombination mechanism.

Perovskite solar cells are expected to work under steady-state conditions. Thus, the steady-state PL intensity as a function of continuous-wave excitation intensity can be used to study the recombination kinetics, because the PL intensity directly reflects the radiative recombination rate. And the PL intensity of a perovskite film is related to the potential maximum voltage the solar cell can achieve. In addition, transient PL decay is a valuable tool to identify the recombination mechanisms that occur during excited-state relaxation processes. The carrier lifetime extracted from the decay curve is an indicator of the perovskite film quality, since a longer carrier lifetime can allow free carriers to be collected by the corresponding electrodes before being recombined. Furthermore, transient absorption spectroscopy enables the characterisation of band edge recombination on an ultrafast timescale, providing insight into the relaxation pathway of photogenerated charges. These measurements can provide information of recombination kinetics in perovskite materials to some extent, thus, different interpretations of experimental data will be reviewed in this section.

2.5.1 Steady-state measurements for identifying recombination kinetics

The measured steady-state PL intensity of perovskite films strongly depends on the excitation intensity (I). A simple way to describe this relationship is the power law dependence (Equation 2.6).

$$PL = I^{x} \tag{2.6}$$

As reported in [78], the PL intensity scales with $I^{3/2}$ for a wide range of excitation from laser intensities much lower than one sun to intensities large enough to create population inversion and optical gain (Figure 2.14a).

This 3/2 power law has been attributed to the trapping effect of intra-gap defects. Assuming the trapped species are electrons, Figure 2.14c demonstrates the recombination pathway at low excitation levels during which the electrons fall into traps before recombining with holes from the valence band. Combining the monomolecular trapping process ($n_e \propto I$) and the remaining radiative bimolecular recombination ($n_h \propto \sqrt{I}$), the steady-state PL at low excitation levels follows the relationship: $PL \propto k_b n_e n_h \propto k_b I^{\frac{3}{2}}$ [78]. At high excitation levels, the densities of photogenerated carriers are much larger than the trap density. As a result, the traps are filled at steady-state condition and bimolecular recombination becomes dominant. Thus, the power law slowly changes to a linear one, where $n_{h(e)} \propto \sqrt{I}$ [78].

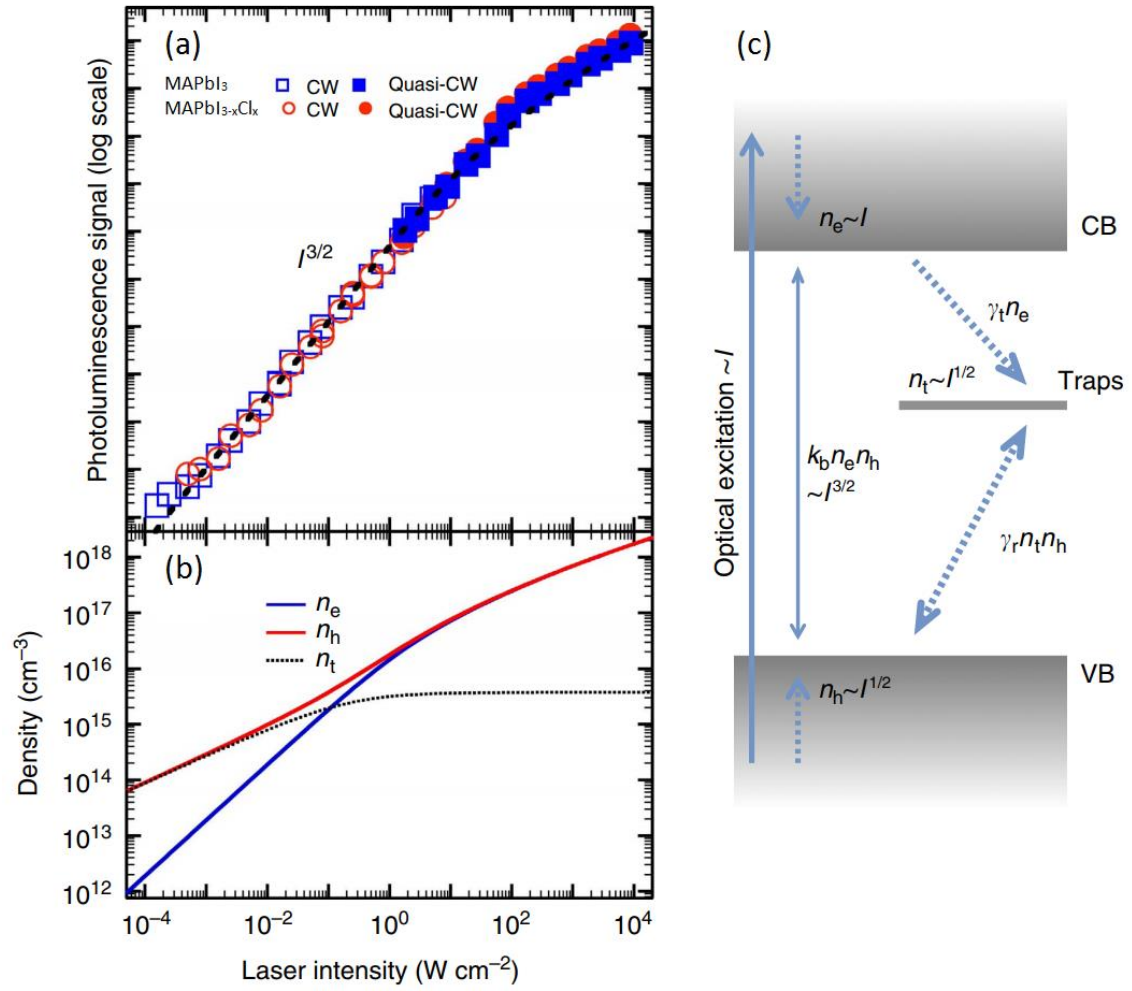

Figure 2.14 (a) Steady-state PL signal as a function of laser intensity. (b) Electron density (blue line), hole density (red line) and the density of filled traps (dotted line) as a function of laser intensity. (c) Schematic diagram of the relaxation of optical excitations under steady-state conditions. (Adapted from [78])

Sutter-Fella performed similar steady-state PL measurements on $CH_3NH_3PbI_{3-x}Br_x$ perovskite materials [79] as a function of the photocarrier generation rate. By varying the ratio of I^- and Br^-, the fits resulted in different power laws (Figure 2.15). In this work, the excitation levels are represented as carrier generation rates, and the PL intensity, which is proportional to radiative recombination rate, was characterised by power law fits. For steady-state condition, total recombination rate (combining radiative recombination, SRH recombination and Auger recombination) equals to the carrier generation rate. Thus, power law dependence equal to 1 reflects direct electron-hole recombination (radiative recombination) [79]. SRH recombination is dominated at lower excitation levels, where traps are not fully filled; and Auger recombination will be dominating at higher excitation levels.

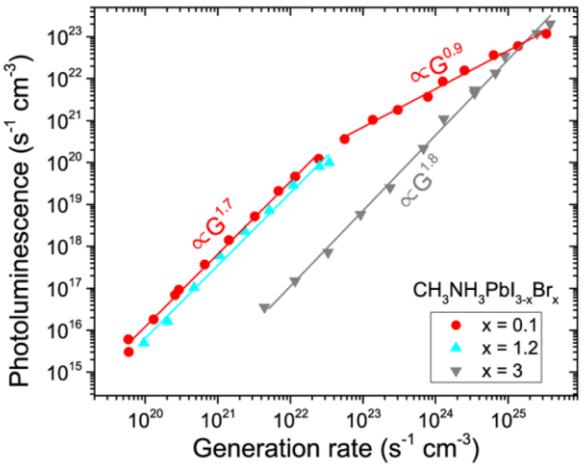

Figure 2.15 Steady-state PL signal as a function of generation rate for three Br concentrations. Solid lines are fit of the data. (Adapted from [79])

Comparing the transition of recombination kinetics among different perovskite materials, it is found that the pure Br perovskite could have a higher trap density than mixed-halide perovskites. However, the exact value of the trap density could not be extracted from this plot.

Blancon *et al* further investigated the excitation-dependent PL intensity with the extracted equivalent excitation density from time-dependent PL intensity at the band-edge [80]. In this case, the measured PL intensities were plotted as a function of correlated excitation densities (Figure 2.16). Power law fits were then applied to the experimental data showing a transition of gradient from monomolecular recombination ($I_{PL}{\sim}N_0$) to bi-molecular recombination ($I_{PL}{\sim}N_0^2$) at the excitation density of $2.5 \times 10^{15} cm^{-3}$. This allowed for an estimation of intrinsic trap density $N_t \approx 2.5 \times 10^{15} cm^{-3}$ [80].

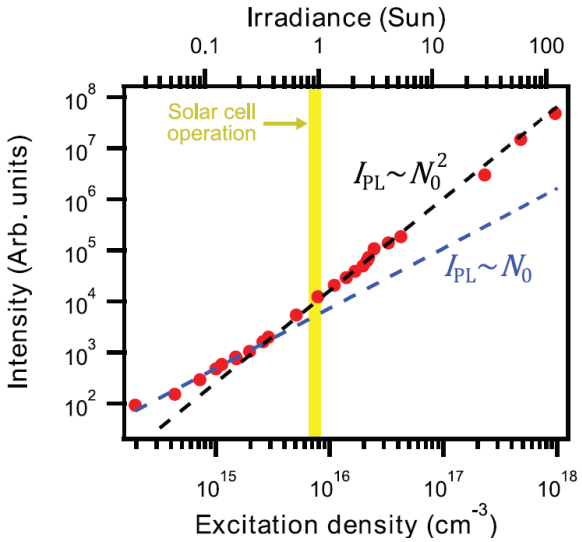

Figure 2.16 Steady-state PL signal as a function of excitation density. Dashed lines are fits of the data. (Adapted from [80])

Here, it is found that the trend of power law dependences is different with previous studies (Figure 2.14 and Figure 2.15). However, both trends can be observed if the range of excitation intensity is sufficiently large (Chapter 6 Figure 6.5). The modelled result in Chapter 7 (Figure 7.6) also describes the domination of recombination kinetics at different excitation levels in detail. The power law fit of excitation-dependent steady-state PL intensity has the potential to qualitatively identify the dominant of SRH-like monomolecular recombination and radiative bimolecular recombination. However, it is difficult to use this method to quantify recombination rates.

2.5.2 Transient measurements for extracting recombination properties

Apart from the steady-state PL intensity measurement, recombination properties are also analysed based on the results of transient measurements. The recombination kinetics of perovskite films were investigated by analysing the band-edge transitions at various optical pump intensities [81, 82]. From Terahertz photoinduced transient absorption decay, the kinetics of the band-to-band transition can be modelled by the simple polynomial equation (Equation 2.7).

$$-\frac{dn}{dt} = An + Bn^2 + Cn^3 \qquad 2.7$$

n is the photogenerated carrier density and t is time. The three terms were ascribed to three charge carrier annihilation processes: (1) first-order trap-assisted recombination; (2) second-order radiative band-to-band recombination; and (3) third-order Auger recombination.

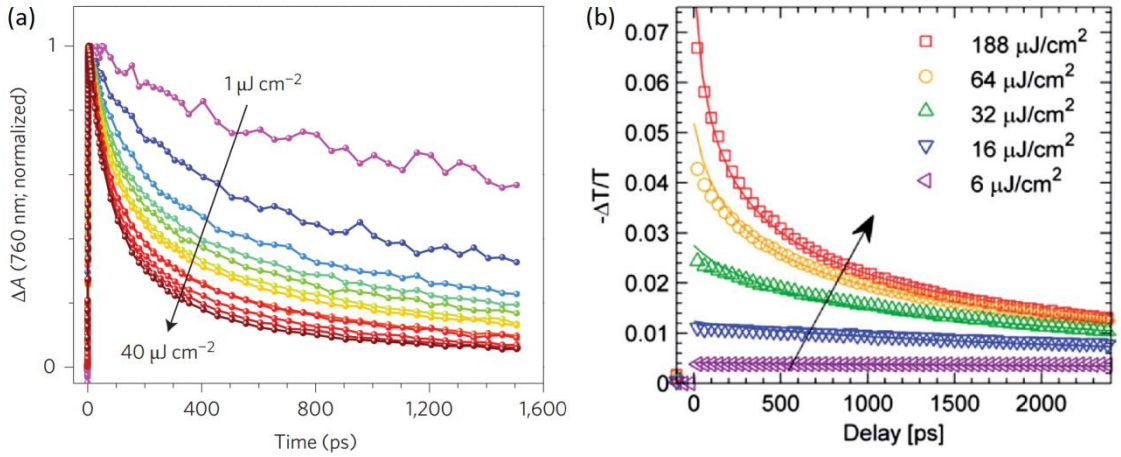

Figure 2.17 (a) Normalised THz photoinduced transient absorption of $CH_3NH_3PbI_3$ for excitation wavelength 760nm. (Adapted from [81]) (b) THz photoinduced transient absorption of $CH_3NH_3PbI_{3-x}Cl_x$ films for excitation wavelength 550 nm. (Adapted from [82])

With the estimated effective carrier mobilities extracted from ultrafast THz absorption spectra, Wehrenfennig extracted the decay constants of $CH_3NH_3PbI_{3-x}Cl_x$ perovskite from transient absorption measurements [82]. Although the decay constants cannot be directly assigned to the corresponding recombination rates, this polynomial fit can still be used to compare the recombination kinetics between different perovskite films. The limitation of this model is that it assumes an equal density of electrons and holes, and thus more complicated models must be used to describe the transient densities of electrons and holes separately.

The above methods are simple numerical analysis of recombination kinetics in perovskites; however, it is also necessary to understand the recombination kinetics based on the underlying physics. Stranks and Manger investigated the transient PL intensity decay by fitting experimental data using rate equations that account for the dynamics of excitons, charge carriers and traps [72, 73]. Both studies considered geminate and non-geminate recombination mechanisms in the models. Geminate recombination is associated with the formation, dissociation and recombination of excitons, which is an issue for organic solar cells as it is difficult to separate the dissociated charges [83]. Non-geminate recombination is associated with the free charge carriers such as radiative, trap-assisted and Auger recombination.

The transient density of electrons (n_e), excitons (n_x) and filled traps (n_T) are expressed in Equation (2.8-2.10) (Equation (1-3) in [72]). R_f, R_d and R_x are the rates of exciton formation, dissociation and decay. R_{eh}, R_{pop} and R_{dep} are the rates of radiative recombination, trap population and depopulation. N_T is the total density of traps in the perovskite films. Using rate equations, Stranks successfully extracted the recombination rates and total trap density from the time-resolved PL measurements at three excitation levels (the fitted curve is shown in Figure 2.18) [72].

$$\frac{dn_e}{dt} = \frac{I}{d} + R_d n_x - R_f n_e n_h - R_{eh} n_e n_h - R_{pop} n_e (N_T - n_T) \quad 2.8$$

$$\frac{dn_x}{dt} = R_f n_e n_h - R_d n_x - R_x n_x \quad 2.9$$

$$\frac{dn_T}{dt} = R_{pop}(N_T - n_T) n_e - R_{dep}(n_T^2 + n_T n_e) \quad 2.10$$

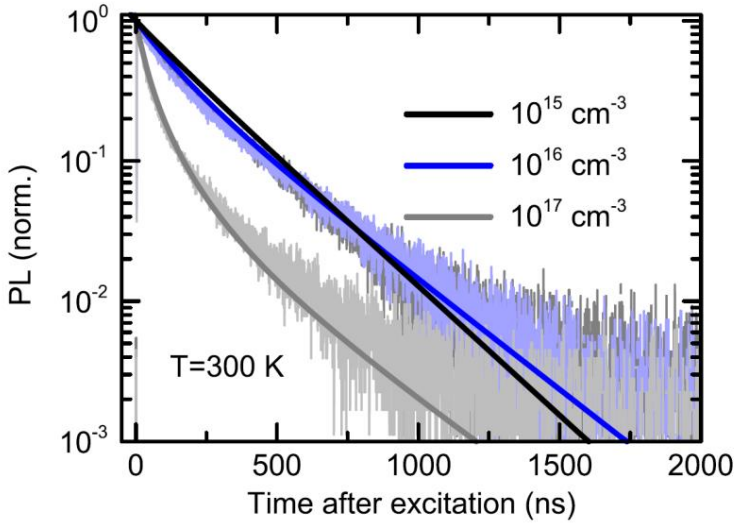

Figure 2.18 PL decays detected at 780 nm for $CH_3NH_3PbI_{3-x}Cl_x$ films with different initial photoexcitation density. Solid lines are fits of the data. (Adapted from [72])

In Figure 2.19, Manger summarised the potential relaxation pathways of photocarriers in perovskite films: dissociation of spatially correlated electron-hole pairs (k_{dis}), recombination of the electron in a hole-catalysed spatially correlated pair (k_{hcat}), third-order Auger recombination (k_{Aug}), radiative recombination between free electrons and holes (k_{rec}), the trapping of free electrons (k_{trap}) and the non-radiative recombination of the de-trapped electrons with free holes (k_{dtrp}).

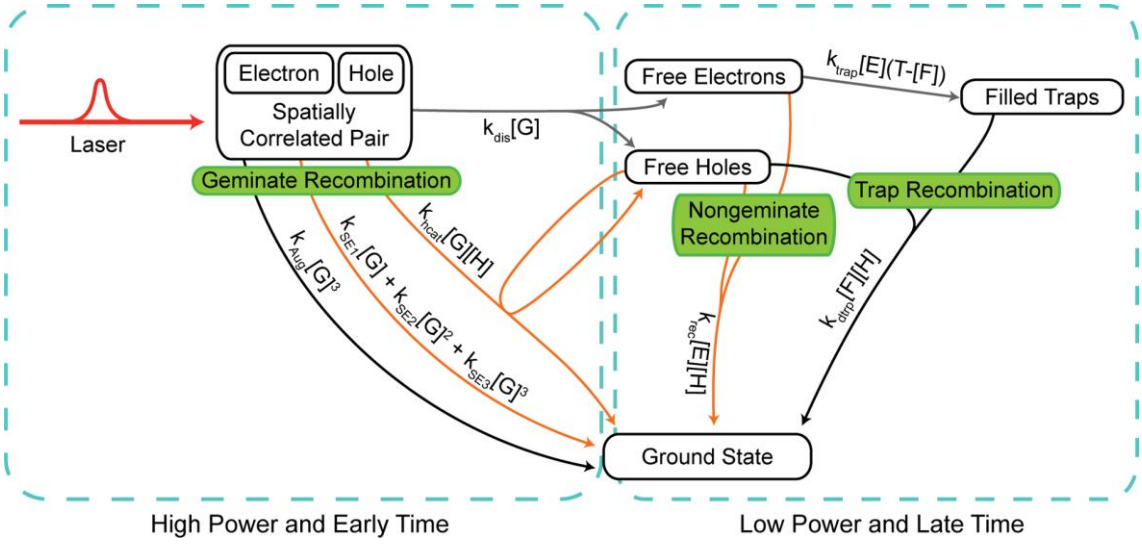

Figure 2.19 Recombination pathways in perovskites. (Adapted from [73])

The recombination kinetics are expressed by the differential equations below:

$$\frac{dG}{dt} = pulse(t) - k_{SE1}G - k_{SE2}G^2 - k_{SE3}G^3 - k_{dis}G - k_{hcat}GH - k_{Aug}G^3 \quad 2.11$$

$$\frac{dE}{dt} = k_{dis}G - k_{rec}EH - k_{trap}E(T - F) \quad 2.12$$

$$\frac{dH}{dt} = k_{dis}G - k_{rec}EH - k_{hcat}GH - k_{dtrp}FH \quad 2.13$$

$$\frac{dF}{dt} = k_{trap}E(T - F) - k_{dtrp}FH \quad 2.14$$

G is the spatially correlated pairs, E and H are the density of free electrons and holes, T is the total density of traps and F is the density of filled traps. Those equations were applied to fit the experimental results of excitation-dependent time-resolved PL measurements and PL quantum yield measurements, giving the fitted recombination rates listed in Table 2 in [73]. In this work, the fitting error had been estimated by generating a Hessian matrix from the partial derivatives of the error function [73].

2.5.3 General solution of trap-assisted recombination

From the studies of recombination kinetics reviewed above, it can be concluded that the trap-assisted recombination is a major relaxation pathway for free carriers, since the trap density in perovskite materials is always very high (from both measured and fitted results) [72-76]. Trap-assisted recombination is also called Shockley-Read-Hall (SRH) recombination because this recombination mechanism was first investigated by Shockley and Read [84] and experimentally confirmed by Hall [85]. In the Shockley and Read model, four parameters of traps – trap density (N_t), trap energy level (E_t), as well as capture coefficients of electrons and holes ($\langle c_n \rangle = \sigma_n v_{th}, \langle e_n \rangle = \sigma_p v_{th}$) were included, where σ_n and σ_p are the capture cross-section of electrons and holes respectively, and v_{th} is the thermal velocity.

The widely-used expression for the SRH recombination rate at steady-state condition ($U = C_n C_p (pn - p_1 n_1) / \left[C_n(n + n_1) + C_p(p + p_1)\right]$) was derived in the original paper by Shockley and Read (Equation (4.4) in [84]), where n_1 is the number of electrons in the conduction band for the case in which the Fermi level falls at E_t, and p_1 is the number of holes in the valence band for the case in which the Fermi level falls at E_t. The SRH recombination coefficients are related to trap density and capture cross-sections ($C_n = N_t \sigma_n v_{th}, C_p = N_t \sigma_p v_{th}$); n_1 and p_1 are expressed in terms of trap energy level E_t. In the appendix of their paper, Shockley and Read also discussed the

trap-assisted recombination kinetics in the general case where the density of traps is larger than the carrier density [84]. This general model is not typically used for silicon solar cells because the trap density in silicon wafers is normally very low due to the high material purity and crystallinity [86]. Perovskites were reported to have a high density of traps, thus the general model of SRH recombination kinetics is a valuable tool for investigating the trap properties of perovskite materials. More details of the general SRH model and its application in the study of recombination kinetics of perovskite materials will be discussed in Chapter 6.

Recently, this general SRH model had been applied to the characterisation of perovskite materials [87]. Figure 2.20 demonstrated the measured excitation-dependent steady-state PL intensity for perovskite films fabricated by spin coating (SC) and gas-assisted solution processing (GA). By fitting the SRH recombination model to the experimental data, the trap density, electron density and trapping time of free electrons and holes can be extracted [87]. However, this work requires parameters (capture and emission coefficients of electrons) to be taken from literature to estimate the actual values of trap properties. Also, some parameters associated with trapping process may not be very sensitive to steady-state measurements, which makes it difficult to ensure the accuracy of extracted parameters by fitting a single curve. The sensitivity analysis of each parameter in this model will be demonstrated in Chapter 6, which indicates that transient PL measurements are more sensitive to the variation of trap properties including trap density, trap energy level and capture coefficients.

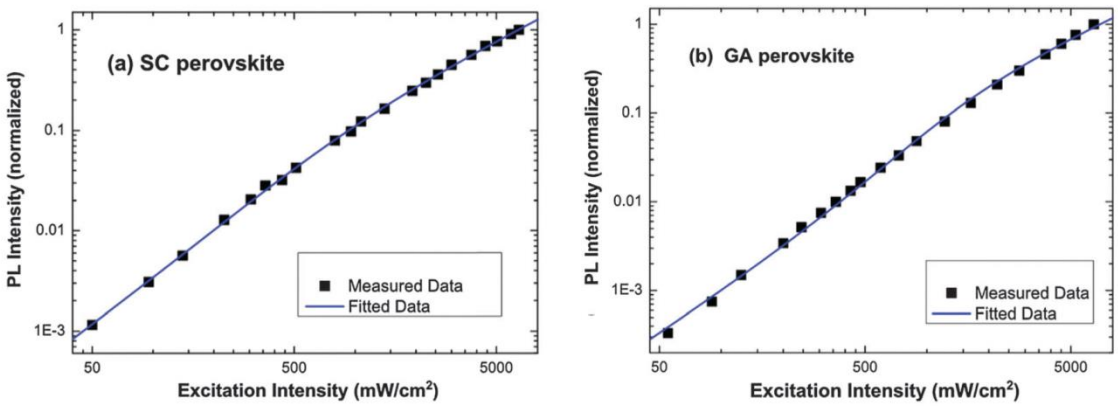

Figure 2.20 Steady-state PL intensity as a function of excitation intensity measured for $CH_3NH_3PbI_3$ perovskite films fabricated by (a) spin coating (SC) and (b) gas-assisted (GA) solution processing technique. Solid lines are fit to the data. (Adapted from [87])

In Chapter 6, this general recombination model is fitted to the results of excitation-dependent steady-state and transient PL measurements simultaneously. Recombination coefficients and trap properties are extracted for $CH_3NH_3PbI_3$ and $Cs_{0.07}Rb_{0.03}FA_{0.765}MA_{0.135}PbI_{2.55}Br_{0.45}$ perovskite films. With this comprehensive recombination model, many theoretical works can also be performed to investigate the physics in perovskite materials by simulating the optoelectronic performance with various input parameters. This model has been applied to analyse the carrier lifetime of perovskites in Chapter 7.

2.6 The interpretation of carrier lifetime

The effective carrier lifetime is one of the most important electronic properties of semiconductor materials for photovoltaic devices. The concept of an effective carrier lifetime is described as the average time for free carriers to remain after generation, which is adequate to visualise the recombination process in semiconductors [88]. From the study of carrier lifetime of silicon wafers, it became clear that using a single, constant lifetime was an oversimplification for interpreting recombination [88]. Usually, each of the trap energy levels is dominant in a certain carrier density or temperature range, and this allows their discrimination. Thus, the measured effective carrier lifetime strongly depends on the experimental conditions.

The most commonly-used method of measuring the carrier lifetime in silicon wafers is the Quasi-steady-state photoconductance (QSSPC) measurement [89], which combines the best of both steady-state and transient photoconductance measurements. However, there are some limitations in adapting the QSSPC method to the measurement of carrier lifetime on perovskite films. Unlike silicon wafers, the resistivity of perovskite films is very high, leading to an ultralow photoconductance of ~10^{-5} S/cm [90], which makes it difficult to be detected. Furthermore, extremely slow photoconductivity response has been observed in perovskite films, as a result of the dipole alignment in the material induced by a combination of illumination and applied bias [91].

In the studies of perovskite solar cells, the most appropriate method of extracting carrier lifetime is the time-resolved PL measurement [62, 64-66]. Because metal halide perovskite materials are direct bandgap semiconductors [92], their PL signal is

sufficiently strong to be easily detected. From the results of PL decay measurements, it has been found that the PL decay curve of perovskite films could not be fitted well by a single time constant in most cases (Figure 2.21). Thus, a second exponential term is often introduced to the curve fitting, resulting in two extracted lifetimes τ_1 and τ_2 [93]. This further proves the necessity of better understanding the transient carrier lifetime in perovskite materials.

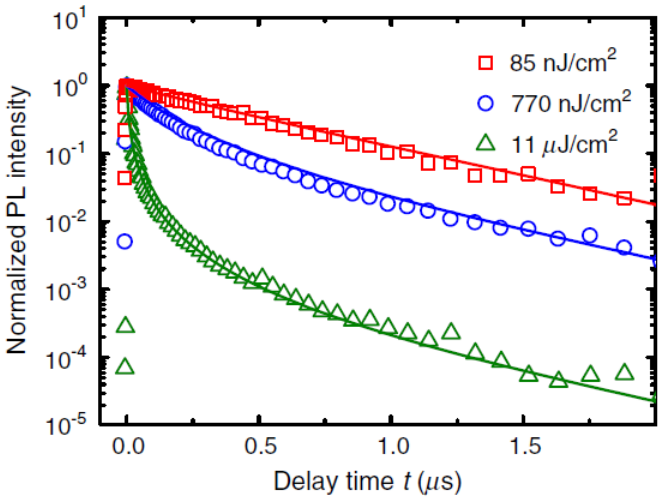

Figure 2.21 Normalised PL decays from measurements of a $CH_3NH_3PbI_{3-x}Cl_x$ perovskite film under different excitation fluences. Solid lines are fits to the data. (Adapted from [94])

Reviewing the studies of transient carrier lifetime on silicon wafers, the relationship between the excess carrier density and effective lifetime has been investigated (Figure 2.22). These studies demonstrated the domination of different recombination kinetics at different carrier injection levels [88]. At low excitation levels, large amount of free carriers are recombined through the SRH pathway due to the low excess carrier density compared with the trap density, leading to a short SRH lifetime that dominates the total effective lifetime. With the increase of excitation density, the second-order radiative recombination and then the third-order Auger recombination start to dominate the recombination kinetics. Under the excitation of standard solar cell operation condition (AM1.5G, 1-Sun), a domination of radiative recombination with long carrier lifetime would be expected for a good solar cell. Thus, this measurement can be applied on silicon wafers to estimate the potential performance of solar cells produced by the wafers [88]. When Auger recombination is dominating at high excitation levels, the slope of the total effective lifetime curve in Figure 2.22 can be used to extract the Auger recombination coefficient [88].

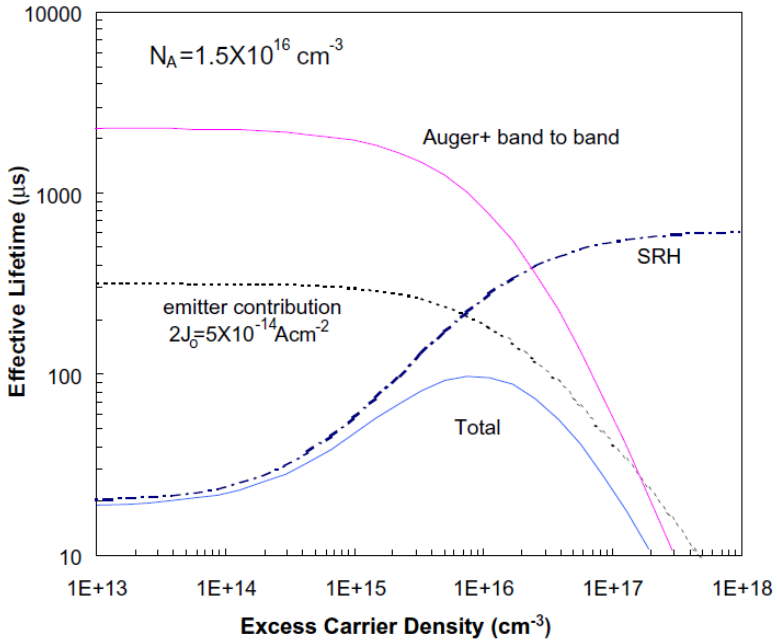

Figure 2.22 Typical curves of lifetime as a function of excess carrier density due to a combination of radiative, SRH and Auger recombination. (Adapted from [88])

Replicating this study for perovskite materials could provide a better understanding of their recombination kinetics in order to further improve the power conversion efficiency of perovskite solar cells.

2.7 Summary

Confocal microscopy has been applied on semiconductor thin film materials. Due to the instability of perovskite materials as reviewed in Section 2.2, the stability of perovskite films must be ensured during the measurements before characterising the optical and electrical properties of perovskites. The observed oxygen-induced PL enhancement of perovskite films leads to the investigation of carrier and trap dynamics as well as the interpretation of recombination rates in perovskite materials. Here, recombination models are used to explain experimental observations. Finally, the study of carrier lifetime on silicon wafers, which is an important indicator of recombination, is discussed. The interpretation of carrier lifetime, which can be directly measured through time-resolved PL decay, has a significant implication on the recombination kinetics of perovskites.

Chapter 3 Experimental and Numerical Methods

This chapter describes the experimental and numerical methods used in this thesis, including fabrication processes of perovskite films, characterisation methods using confocal microscopy, and the theory of modelling laser heating and recombination kinetics.

3.1 Fabrication

Perovskite samples are prepared in the Perovskite Chemical Lab at ANU, Research School of Engineering. Preparation of perovskite solutions and deposition of perovskite films are performed in a glove box filled with N_2 gas. The N_2 gas flow is temporarily paused only when measuring the weight of powders using an analytical balance.

3.1.1 Substrate preparation

Soda-lime glass substrates are cut into 1 cm × 1 cm square. They are washed sequentially with dishwashing liquid (20 min), acetone (10 min), isopropanol (10 min) and ethanol (10 min) in an ultrasonic bath and then treated under UV ozone for 30 min to remove residues.

3.1.2 $CH_3NH_3PbI_3$ film fabrication

The perovskite solution with 1 M concentration is prepared by dissolving a stoichiometric amount of methylammonium iodide (MAI, Dyesol) and lead iodide (PbI_2, 99%, Sigma Aldrich) in a mixture of dimethylformamide (DMF) and dimethyl sulfoxide (DMSO) (7:3 vol/vol). The solution is spin coated on to cleaned glass substrate at a speed of 4000 rpm with a ramp rate of 4000 rpm s^{-1} for 60 s. Chlorobenzene is dropped onto the substrate 10 s before the end of the spin coating to speed up the crystallisation process. The sample is then annealed at 100 °C for 10 min.

Figure 3.1 shows the image of a $CH_3NH_3PbI_3$ perovskite film as captured by Scanning Electron Microscope (SEM). The average crystal size is around 200 nm.

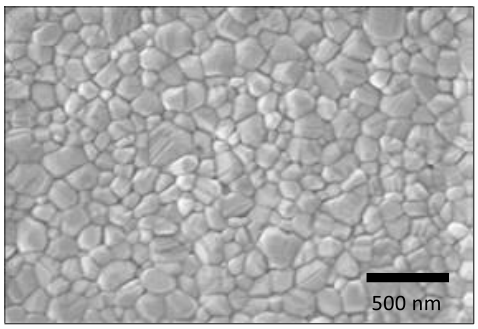

Figure 3.1 SEM image of $CH_3NH_3PbI_3$ film deposited on glass.

Figure 3.2 shows a representative light IV curve of standard $CH_3NH_3PbI_3$ perovskite cells fabricated at ANU with structure ITO/compact-TiO_2/mesoporous-TiO_2/$CH_3NH_3PbI_3$/Spiro-MeOTAD/Au [95]. The inset shows the figures of merit of this cell.

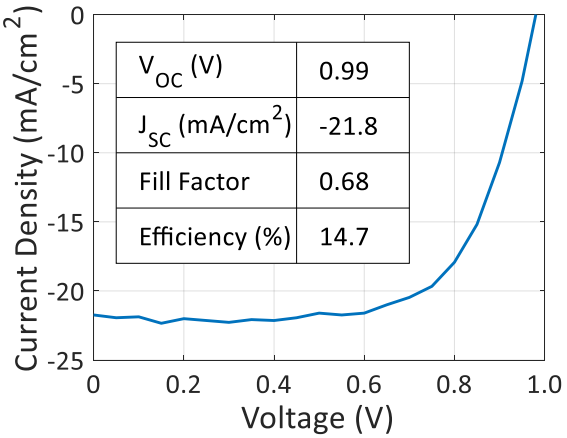

Figure 3.2 Light IV curve of $CH_3NH_3PbI_3$ perovskite cell. The inset table shows the performance parameters of this cell. (Adapted from [95])

3.1.3 $Cs_{0.07}Rb_{0.03}FA_{0.765}MA_{0.135}PbI_{2.55}Br_{0.45}$ film fabrication

The perovskite precursor solution contains 1.2 M lead iodide (PbI_2, 99%, Sigma Aldrich), 1.1 M formamidinium (FAI, Dyesol), 0.2 M lead bromide ($PbBr_2$, 99.999%, Sigma Aldrich), 0.2 M methylammonium bromide (MABr, Dyesol), 0.091 M cesium iodide (CsI, 99.999%, Sigma Aldrich), and 0.039 M rubidium iodide (RbI, 99.9%, Sigma Adlrich) in 1 mL anhydrous DMF:DMSO (4:1, v/v, Sigma Aldrich). The listed stoichiometries are those of the precursors. The solution is spin coated onto cleaned glass substrates by two steps: first at a speed of 2000 rpm with a ramp rate of 200 rpm s^{-1} for 10 s, and then at a speed of 4000 rpm with a ramp rate of 2000 rpm s^{-1} for 20 s. Chlorobenzene is dropped onto the substrate 5 s prior to the end of the second step to speed up the crystallisation process. The sample is then annealed at 100 °C for 45 min.

Figure 3.3 shows a representative light IV curve of standard $Cs_{0.07}Rb_{0.03}FA_{0.765}MA_{0.135}PbI_{2.55}Br_{0.45}$ perovskite cells fabricated at ANU with structure FTO/compact indium-doped TiO_x/mesoporous-TiO_2/PCBM:PMMA (1:3) passivation layer/$Cs_{0.07}Rb_{0.03}FA_{0.765}MA_{0.135}PbI_{2.55}Br_{0.45}$/Spiro-MeOTAD/Au [96]. The figures of merit of this cell are shown in the inset.

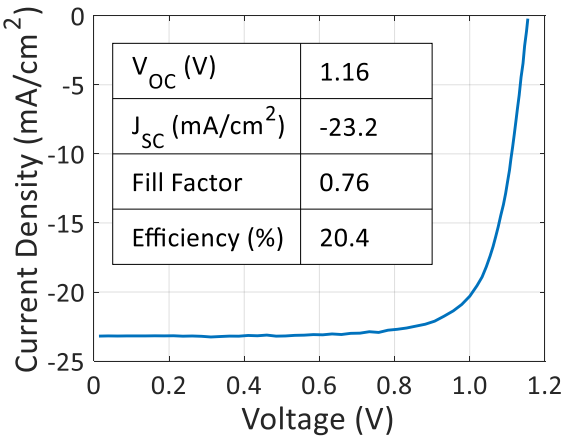

Figure 3.3 Light IV curve of $Cs_{0.07}Rb_{0.03}FA_{0.765}MA_{0.135}PbI_{2.55}Br_{0.45}$ perovskite cell. The inset table shows the performance parameters of this cell. (Adapted from [96])

3.1.4 Poly(methyl methacrylate) coating

The perovskite films used in some experiments are coated with a layer of Poly(methyl methacrylate) (PMMA). The PMMA solution (Micro Chem 495 PMMA A2) is spin coated onto the perovskite film at a speed of 3000 rpm for 30 s. The film is then annealed again at 100 °C for 5 min. The thickness of the PMMA film is around 200 nm, which is estimated from cross-section scanning electron microscope (SEM) image.

3.2 Characterisation

3.2.1 The WITec system

The WITec alpha300 S system was used to perform reflectance mappings and photocurrent mappings on a silicon thin film solar cell (Section 4.1), as well as PL mappings and time-dependent PL intensity measurements on $CH_3NH_3PbI_3$ perovskite films (Chapter 5).

The WITec alpha300 S system combines the advantages of Scanning Near-field Optical Microscopy (SNOM), Confocal Microscopy and Atomic Force Microscopy (AFM) in a single instrument. It comes with a single photon-counting Si avalanche photodiode (APD) detector. The highly-linear, piezo-driven, and feedback-controlled scan stage

provides high accuracy and stability and eliminates the hysteresis, creep and non-linearity that may arise from multiple scanning. The objective lenses used in this system are an Olympus MPlanFL N 10× and an MPlanFL N 100×. The focus was adjusted to give the highest PL signal, rather than the smallest spot size during the measurements. Thus, the focus was adjusted in the same way when measuring the laser spot (laser spot profiles are shown in Figure 3.4).

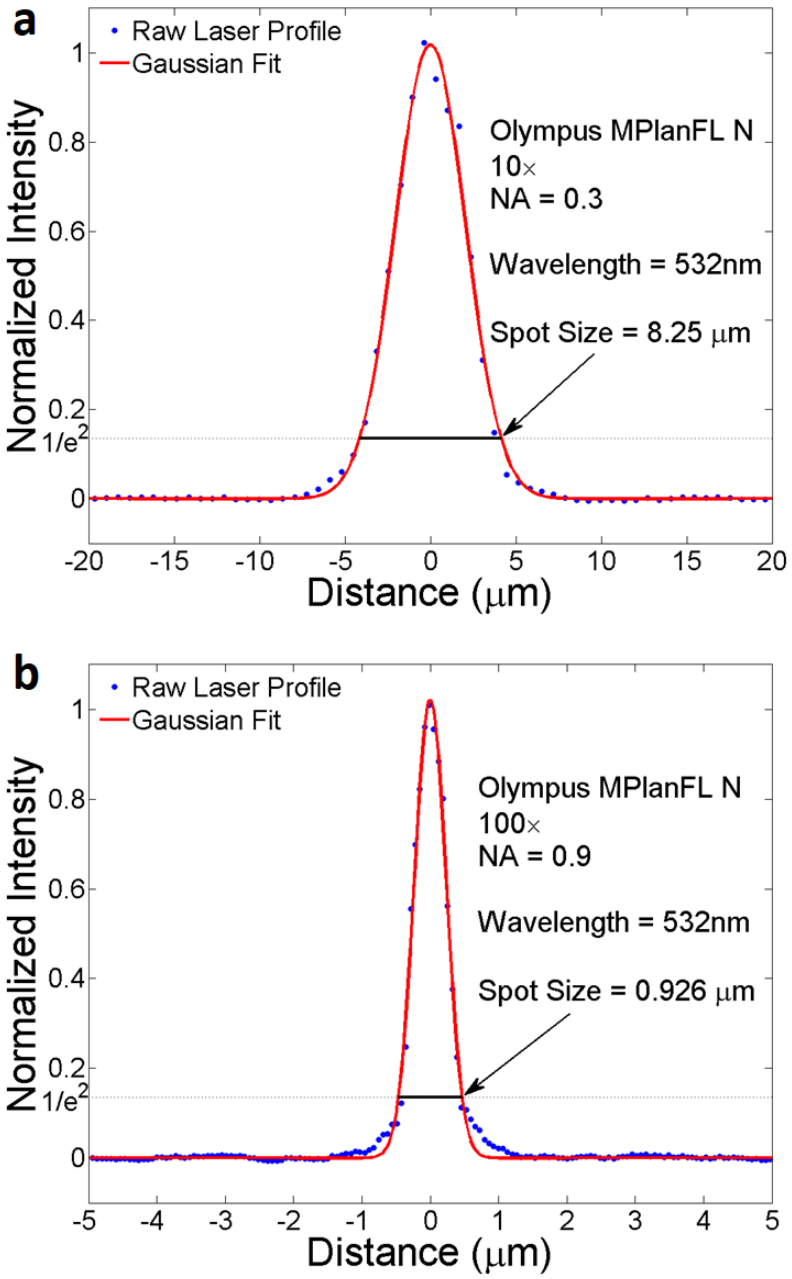

Figure 3.4 Cross-section plots of the Gaussian beam captured by CCD camera using (a) Olympus MPlanFL N 10× objective lens and (b) Olympus MPlanFL N 100× objective lens.

There are two laser sources in this lab: a Fianium Whitelase Supercontinuum laser (Model SC400-2) and a continuous wave 532 nm diode laser. An Acousto-Optic Tunable Filter (AOTF) is connected to the output of Supercontinuum laser to select up to 8 simultaneous tunable wavelengths from the laser source. The AOTF crystals in this lab cover the spectral range from 400 nm to 1100 nm.

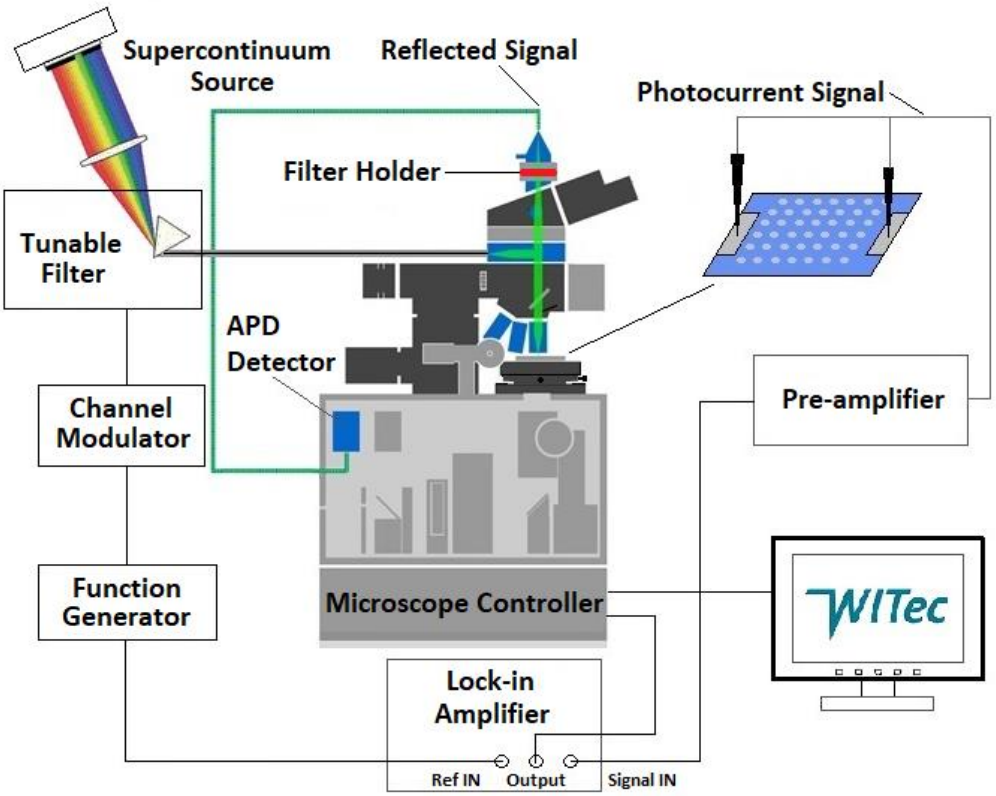

Figure 3.5 The schematic diagram of measurements using WITec alpha300 S system. Adapted from WITec alpha300 S user manual [97].

The experimental methods of reflectance mapping, photocurrent mapping, PL mapping and time-dependent PL measurement are described below.

Reflectance mapping

In reflectance mapping, the 100× objective lens is used to extract high resolution image. The reflected light is collected by the APD detector and then the signal is transmitted to a computer through the microscope controller to generate the image (shown in Figure 3.5). Figure 3.6 shows an example of the output reflectance image.

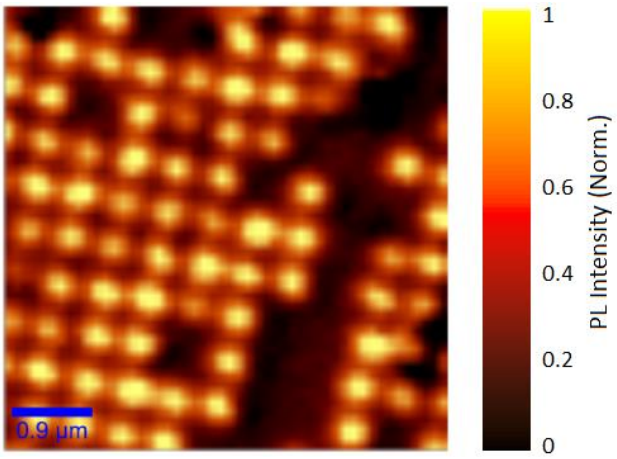

Figure 3.6 Reflectance image of a Silicon thin film solar cell coated with silver nanoparticles extracted by WITec system (bright areas correspond to higher reflectance). The integration time of each pixel is 3 ms and there are 10 pixels per nanometre.

Photocurrent mapping

As demonstrated in Figure 3.5, white light generated by the Fianium Whitelase Supercontinuum laser source is filtered to a narrow band (~8-10nm) source by the AOTF. A square wave created by Function/Arbitrary Waveform Generator (model Agilent 33220A) is used to modulate the AOTF output (on/off) through a channel modulator which is connected to the corresponding channel of the AOTF output. At the scan stage, two needle contacts are connected to the anode and cathode of the solar cell. The photogenerated current is amplified by a Low-Noise Current Pre-amplifier (model SR570) and then fed into a DSP Lock-in Amplifier (model SR850). In the meantime, the function generator provides the reference signal to the lock-in amplifier for synchronising the photocurrent signal when the laser is turned on in order to remove noise signal. The modulation frequency of the function generator is 333.3 Hz (3 ms period) and the lock-in time constant is 30 µs. The output photocurrent image is shown in Figure 3.7.

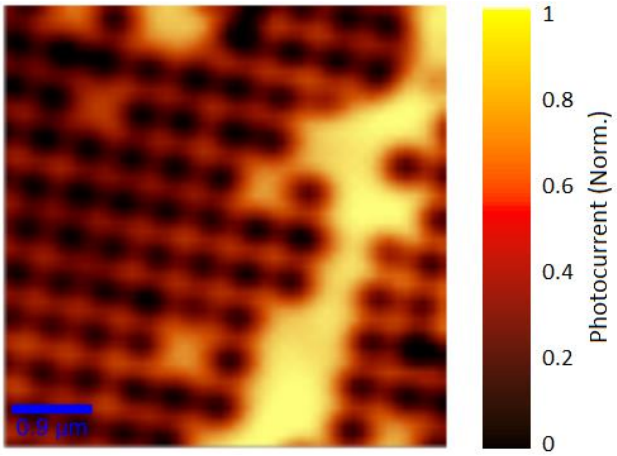

Figure 3.7 Photocurrent image of a Silicon thin film solar cell coated with silver nanoparticles extracted by WITec system (bright areas correspond to higher photocurrent). The integration time of each pixel is 3 ms and there are 10 pixels per nanometre.

Since the optical signal of the reflectance and the electrical signal of the photocurrent are detected independently, this system can collect the reflectance and photocurrent data during a single scan. As shown in Figure 3.6 and Figure 3.7, the same area of the silicon thin film solar cell is scanned, and the reflectance mapping and photocurrent mapping are generated simultaneously.

PL mapping

The configuration of PL mapping is similar to the reflectance mapping. However, a long-pass filter with a cut-off edge larger than the laser wavelength is inserted in front of the detector (Filter Holder in Figure 3.5) to block the reflected excitation light and to transmit the emitted photoluminescence. Figure 3.8 shows a PL image of a large crystal perovskite film.

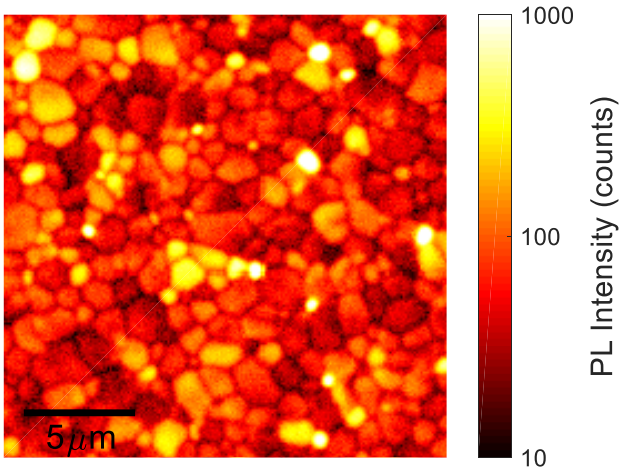

Figure 3.8 PL image of a large crystal perovskite film extracted by WITec system. The integration time of each pixel is 1 ms and there are 10 pixels per nanometre.

Time-dependent PL intensity

Due to the instability of perovskite films, the PL intensity changes with time. To quantify such phenomenon, time-dependent PL intensity is used to track the change of a single point. The real-time signal is sampled by an avalanche photodiode detector (APD) with millisecond resolution in the WITec system. The experimental result shown in Figure 3.9 illustrates the stability of perovskite films.

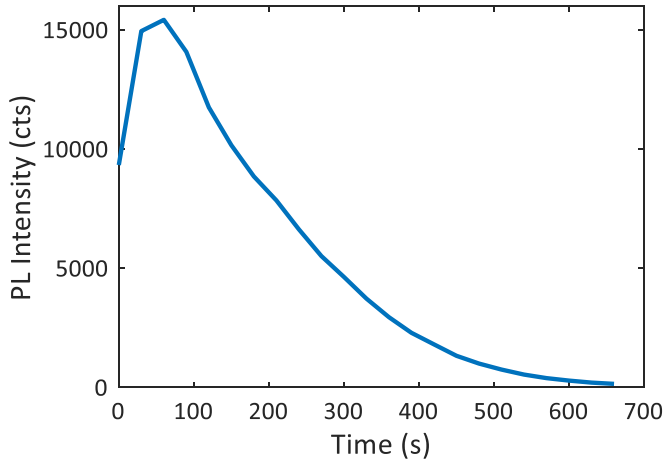

Figure 3.9 Time-dependent PL intensity of a perovskite film measured by WITec system. Laser wavelength is 532 nm and laser intensity is 150 W/cm².

The measurement demonstrated in Figure 3.9 can successfully trace the time-dependent change in PL for a single point. Thus, combining both PL mapping and time-dependent PL intensity measurement, a continuous scan across an area is employed to visualise the change of the scan area (Figure 3.10).

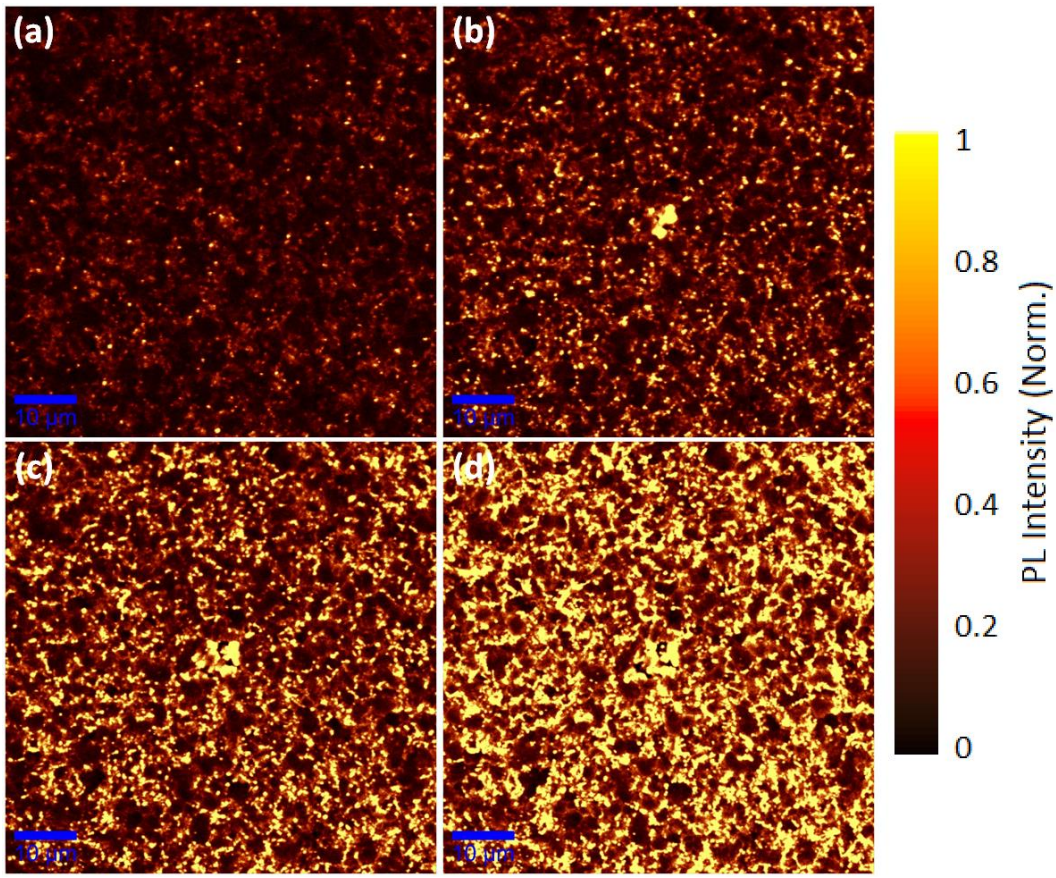

Figure 3.10 Continuous PL mapping of the same area on a perovskite film. (a) is the first scan, (b) is the second scan, (c) is the third scan, and (d) is the fourth scan. Each image requires 2 min to be extracted. The integration time of each pixel is 1 ms and there are 10 pixels per nanometre.

3.2.2 The Horiba system

The Horiba LabRAM HR Evolution system is used to measure the PL spectrum and time-resolved PL lifetime of perovskite films (Chapter 6). A Linkam FTIR600 stage is attached onto the microscope sample stage. During the measurements, the perovskite samples are kept inside the stage chamber with N_2 gas flowing across. A 532 nm DPSS-laser is used to measure the PL spectrum and a 508 nm diode laser (DD-510L, Horiba) with pulse duration of 110ps is used to measure the PL lifetime. Both the incident light and the emitted light go through a 50x objective lens (LEICA PL FLUOTAR L 50×/0.55). The laser focus was adjusted to give the highest PL signal, rather than the smallest spot size during the measurements. Thus, the focus was adjusted in the same way when measuring the laser spot. The measured laser spot size is shown in Figure 3.11. The 508 nm pulsed laser was illuminated through a beam splitter, which leads to the odd shape of the laser spot (Figure 3.11b).

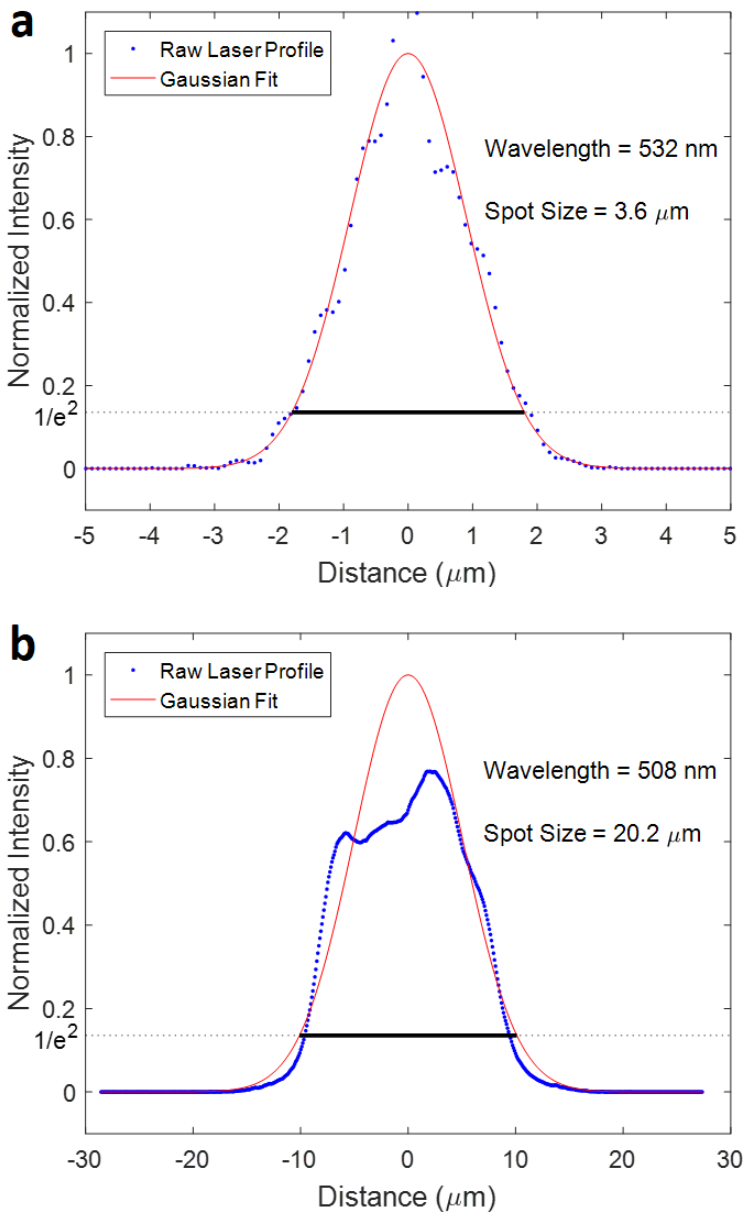

Figure 3.11 Cross-section plots of the Gaussian beam through the 50x objective lens (LEICA PL FLUOTAR L 50×/0.55) using (a) 532 nm DPSS-laser and (b) 508 nm diode laser (DD-510L, Horiba), respectively.

The experimental details for measuring the PL spectrum and PL lifetime are explained below.

PL spectrum measurement

In this experiment, the sample is illuminated by a 532 nm DPSS-laser and the PL signal is extracted using a Syncerity CCD deep cooled camera with a grating of 150 grooves/mm. The spectral response of the entire system is determined with a calibrated halogen-tungsten light source. To change the excitation level, an absorptive neutral density filter (AR-coated for 350-700 nm) – ND1, ND2, ND3, ND4 or ND5 are

inserted in front of incident light. To protect the detector, an absorptive neutral density filter (AR-coated for 650-1050 nm) – ND1, ND2, ND3, ND4 or ND5 is inserted in front of the detector.

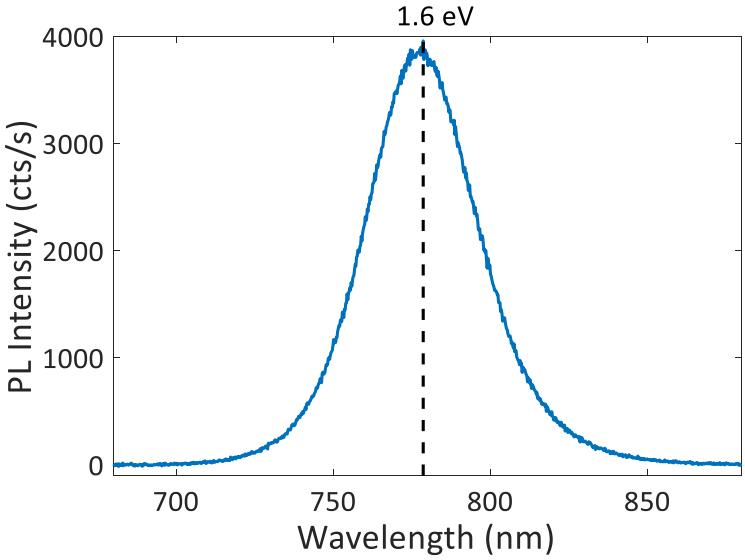

Figure 3.12 PL spectrum of a $CH_3NH_3PbI_3$ perovskite film measured by HORIBA system.

PL lifetime measurement

Time-resolved photoluminescence decay measurements are performed using a time-correlated single photon counting (TCSPC) system (DeltaPro-DD, Horiba) along with the LabRAM HR Evolution system. The sample is illuminated by a Horiba DD-510L diode laser with $508 \pm 10\,nm$ peak wavelength, $110\,ps$ pulse width and $100\,MHz$ maximum repetition rate. The maximum excitation intensity of the pulse laser is $4.8 \times 10^{15}\,cm^{-3}$. To change the excitation level, a neutral density filter (ND0.3 or ND0.6) is inserted in front of incident light.

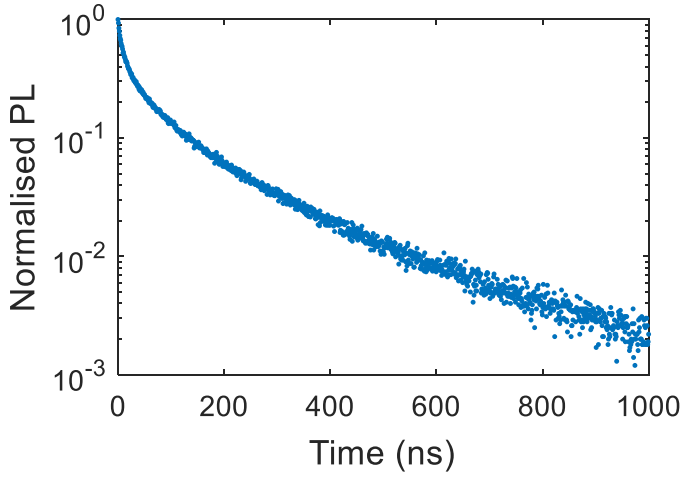

Figure 3.13 Time-resolved PL decay of a $CH_3NH_3PbI_3$ perovskite film measured by HORIBA system.

3.3 Modelling

3.3.1 Laser heating model

An analytical solution of laser-induced heating can be applied to estimate the local temperature of perovskite films under laser exposure. In this section, the model to calculate the temperature rise due to laser heating as derived by D. W. Bäuerle is presented [98]. Table 3.1 defines the parameters that will be used in the derivation.

Table 3.1 Symbols of laser heating model

$P\ (W)$	Laser power
$D(cm^2 s^{-1})$	Heat diffusivity
$\alpha\ (cm^{-1})$	Absorption coefficient
$h_s\ (cm)$	Thickness of the thin film
$w_0\ (cm)$	Gaussian beam width
$\eta\ \left(W/(cm^2 \cdot K)\right)$	Surface conductance
$\kappa\ \left(W/(cm \cdot K)\right)$	Thermal conductivity
R	Reflectivity

For convenience, the dimensionless variables are introduced. The normalised coordinates are

$$x^* = \frac{x}{l};\ y^* = \frac{y}{l};\ z^* = \frac{z}{l} \tag{3.1}$$

where l is the characteristic length. In this problem, the width of laser beam w_0 and the thickness of the thin film h_s are the appropriate normalisation factors. Thus, the characteristic length in this model is defined as the minimum value between w_0 and h_s.

The dimensionless time t^*, absorption coefficient α^*, thickness h_s^*, as well as the heat transfer coefficients η_0^* and η_h^*, thermal conductivities κ_0^* and κ_h^* at top and rear surface of the thin film are introduced in Equations 3.2 and 3.3.

$$t^* = \frac{D}{l^2}t;\ \alpha^* = \alpha l;\ h_s^* = \frac{h_s}{l} \tag{3.2}$$

$$\eta_0^* = \frac{\eta_0 l}{\kappa};\ \eta_h^* = \frac{\eta_h l}{\kappa};\ \kappa_0^* = \frac{\kappa_0}{\kappa};\ \kappa_h^* = \frac{\kappa_h}{\kappa} \tag{3.3}$$

To simplify the calculation, a finite but temperature-independent absorption coefficient is assumed and the interference phenomena within the film are ignored. Also, equal surface conductance at both side of the film is assumed, so that $\kappa_0^* = \kappa_h^* = 1$ and $\eta_0^* = \eta_h^* = \eta^*$. The laser beam switches on at $t = 0$ in the position $x = y = 0$. The solution of increased temperature θ can be written as

$$\theta(x^*, y^*, z^*, t^*) = \frac{l}{\kappa} I_a \int_0^{t^*} q(t^* - t_1^*) \mathcal{g}(x^*, y^*, t^*, t_1^*) \mathcal{F}(z^*, t_1^*) dt_1^*, \qquad 3.4$$

where $I_a = I_0(1 - R) = \frac{2P}{\pi w_0^2}(1 - R)$ is the maximum laser intensity that is not reflected from the surface.

The q-function defines the shape of laser pulse. For a static CW-laser beam, the q-function is equivalent to the Heaviside step function $\mathcal{H}$.

$$q(t) = \mathcal{H}(t) = \begin{cases} 0 \text{ if } t \leq 0 \\ 1 \text{ if } t > 0 \end{cases} \qquad 3.5$$

$\mathcal{g}$ and $\mathcal{F}$ describe the temperature field within the xy-plane and in the z-direction, respectively,

$$\begin{aligned} \mathcal{g}(x^*, y^*, t^*, t_1^*) & \\ &= \frac{1}{4\pi t_1^*} \int_{-\infty}^{+\infty} dx_1^* \int_{-\infty}^{+\infty} dy_1^* \, g(x_1^*, y_1^*) \\ &\times \exp\left(- \frac{(x_1^* - x^*)^2 + (y_1^* - y^*)^2}{4t_1^*} \right). \end{aligned} \qquad 3.6$$

For a Gaussian beam,

$$g(x^*, y^*) = \exp\left(-x^{*2} - y^{*2}\right). \qquad 3.7$$

Thus,

$$\mathcal{g}(x^*, y^*, t^*, t_1^*) = \frac{1}{1 + 4t_1^*} \exp\left(- \frac{x^{*2} + y^{*2}}{1 + 4t_1^*} \right). \qquad 3.8$$

The temperature distribution along the axis of laser-beam propagation (z-direction) is determined by the $\mathcal{F}$-function only. This function depends on the absorption coefficient α^*, the heat loss described by η^*, and the thickness of the substrate h_s^*. The $\mathcal{F}$-function can be written in the form

$$\mathcal{F}(z^*, t_1^*) = \alpha^* \sum_{n=-\infty}^{\infty} F_n(z^*, t_1^*) = \alpha^* \left(F_0(z^*, t_1^*) + 2 \sum_{n=1}^{\infty} F_n(z^*, t_1^*) \right) \quad 3.9$$

with

$$F_n(z^*, t_1^*) = A_n f_n(z^*, t_1^*). \quad 3.10$$

Here,

$$A_n = \int_0^{h_s^*} Z_n(z_1^*) \exp(-\alpha^* z_1^*)\, dz_1^* = \frac{1}{\alpha^{*2} + \nu_n^2} \left[(\alpha^* + \eta^*)(1 - \cos(\nu_n h_s^*) \exp(-\alpha^* h_s^*)) + \frac{\nu_n^2 - \alpha^* \eta^*}{\nu_n} \sin(\nu_n h_s^*) \exp(-\alpha^* h_s^*) \right] \quad 3.11$$

$$f_n(z^*, t_1^*) = B_n Z_n(z^*) \exp(-\nu_n^2 t_1^*) \quad 3.12$$

$$B_n = \frac{\nu_n^2}{h_s^* \left(\nu_n^{*2} + \eta^{*2} \right) + 2\eta^*} \quad 3.13$$

$$Z_n = \cos(\nu_n z^*) + \frac{\eta^*}{\nu_n} \sin(\nu_n z^*), \quad 3.14$$

ν_n are the roots of

$$\tan(h_s^* \nu_n) = \frac{2\eta^* \nu_n}{\nu_n^2 - \eta^{*2}}. \quad 3.15$$

Substitute Equations 3.5-3.15 into Equation 3.4, the laser-induced temperature increase on the sample can be calculated.

3.3.2 Recombination model

In 1952, W. Shockley and W. T. Read investigated the Fermi-Dirac statistics of the recombination of electrons and holes through traps [84]. In this section, the fundamental theory of recombination dynamics in the general case is presented. Table 3.2 lists the symbols used in the analytic solution and the equations related to SRH recombination as derived by Shockley and Read (Equation 3.23-3.34).

Table 3.2 Symbols of recombination model

$n\ (cm^{-3})$	Electron density in the conduction band
$p\ (cm^{-3})$	Hole density in the valence band
$G(cm^{-3}s^{-1})$	Generation rate
$U_{rad}(cm^{-3}s^{-1})$	Radiative recombination rate
$U_{SRH_n}(cm^{-3}s^{-1})$	Shockley-Read-Hall recombination rate of electron
$U_{SRH_p}(cm^{-3}s^{-1})$	Shockley-Read-Hall recombination rate of hole
$U_{Aug}(cm^{-3}s^{-1})$	Auger recombination rate
$B\ (cm^3s^{-1})$	Radiative recombination coefficient
$n_i\ (cm^{-3})$	Intrinsic carrier density
$\Gamma_n\ (cm^6s^{-1})$	Auger recombination coefficient of electron
$\Gamma_p\ (cm^6s^{-1})$	Auger recombination coefficient of hole
$C_n(s^{-1})$	Shockley-Read-Hall recombination coefficient of electron
$C_p(s^{-1})$	Shockley-Read-Hall recombination coefficient of hole
f_t	Fraction of traps occupied by electrons
$N_t\ (cm^{-3})$	Trap density
$E_t\ (eV)$	Trap energy level (below the conduction band)
$n_1\ (cm^{-3})$	The number of electrons in the conduction band for the case in which the Fermi level falls at E_t
$p_1\ (cm^{-3})$	The number of holes in the valence band for the case in which the Fermi level falls at E_t
$\langle c_n \rangle\ (cm^3s^{-1})$	Capture coefficient of electron
$\langle e_n \rangle\ (cm^3s^{-1})$	Emission coefficient of electron (or Capture coefficient of hole)
$\sigma_n\ (cm^2)$	Capture cross-section of electron
$\sigma_p\ (cm^2)$	Capture cross-section of hole
$v_{th}\ (cm/s)$	Thermal velocity
$N_A\ (cm^{-3})$	Acceptor Density

The density of electrons and holes follows the differential equations

$$\frac{dn}{dt} = G - \left(U_{rad} + U_{SRH_n} + U_{Aug}\right), \tag{3.16}$$

$$\frac{dp}{dt} = G - \left(U_{rad} + U_{SRH_p} + U_{Aug}\right). \quad 3.17$$

The carrier generation rate G depends on the excitation energy,

$$G = \frac{\int_0^t \alpha\varphi_0 e^{-\alpha x} dx}{t} = \frac{\varphi_0(1 - e^{-\alpha t})}{t}, \quad 3.18$$

where φ_0 is the photon flux at the surface; α is the absorption coefficient; x is the distance into the film; and t is the thickness of the film.

The photon flux is calculated from laser power P, wavelength λ and spot size w_0:

$$\varphi_0 = I_0 / \frac{hc}{\lambda}, \quad 3.19$$

$$I_0 = \frac{2P}{\pi w_0^2}, \quad 3.20$$

where I_0 is the laser intensity; h is the Planck constant; and c is the speed of light.

The radiative recombination rate (U_{rad}) [99] and Auger recombination rate (U_{Aug}) [100] are given by

$$U_{rad} = B(np - n_i^2), \quad 3.21$$

and

$$U_{Aug} = \Gamma_n n(np - n_i^2) + \Gamma_p p(np - n_i^2). \quad 3.22$$

Shockley and Read provided a detailed derivation of the SRH recombination rate [84]. In their theory, the net capture rate of electrons and holes of the SRH recombination in non-degenerate semiconductors can be written as

$$U_{SRH_n} = C_n(1 - f_t)n - C_n f_t n_1, \quad 3.23$$

and

$$U_{SRH_p} = C_p f_t n - C_p(1 - f_t)p_1. \quad 3.24$$

Under steady-state conditions, the net rate of capture of electrons must be equal to that of holes ($U_{SRH_n} = U_{SRH_p}$), which can be used for solving f_t. Substituting the expression of f_t into either Equation 3.23 or 3.24, the steady-state SRH recombination rate is obtained:

$$U_{SRH} = \frac{C_n C_p (np - n_1 p_1)}{C_n (n + n_1) + C_p (p + p_1)}. \tag{3.25}$$

However, the SRH recombination rates of electrons and holes (U_{SRH_n} and U_{SRH_p}) are not necessarily equal in the transient condition. Therefore, in the general case the rate of electrons being trapped by the defect state U_{SRH_n} and the rate of the trapped electrons being emitted from the defect state and relaxing to the valence band U_{SRH_p} are expressed respectively by small deviations Δn, Δp and Δf_t from the equilibrium values n_0, p_0 and f_{t0}

$$\begin{aligned} U_{SRH_n} &= [C_n(1 - f_t)n - C_n f_t n_1] - [C_n(1 - f_{t0})n_0 - C_n f_{t0} n_1] \\ &= C_n[(1 - f_t)\Delta n - (n_0 + n_1)\Delta f_t], \end{aligned} \tag{3.26}$$

and

$$\begin{aligned} U_{SRH_p} &= \left[C_p f_t n - C_p(1 - f_t)p_1\right] - \left[C_p f_{t0} n_0 - C_p(1 - f_{t0})p_1\right] \\ &= C_p[f_t \Delta p + (p_0 + p_1)\Delta f_t]. \end{aligned} \tag{3.27}$$

The equilibrium value f_{t0} can be derived when

$$C_n(1 - f_{t0})n_0 - C_n f_{t0} n_1 = C_p f_{t0} n_0 - C_p(1 - f_{t0})p_1 = 0. \tag{3.28}$$

Thus,

$$f_{t0} = \frac{1}{1 + n_1/n_0} = 1 - \frac{1}{1 + p_1/p_0}. \tag{3.29}$$

The requirement of electrical neutrality in the measurement without applied electric field gives the relationship between Δn, Δp and Δf_t,

$$\Delta f_t = f_t - f_{t0} = \frac{\Delta p - \Delta n}{N_t}. \tag{3.30}$$

Further information in the SRH recombination has been derived [84]. Firstly, C_n and C_p will be affected by the trap density and the capture cross-section area of electrons and holes,

$$C_n = N_t\langle c_n\rangle = N_t\sigma_n v_{th}, \quad 3.31$$

$$C_p = N_t\langle e_n\rangle = N_t\sigma_p v_{th}. \quad 3.32$$

Also, n_1 and p_1 are strongly related to trap energy level:

$$n_1 = N_C \exp\left(\frac{E_t - E_C}{kT}\right), \quad 3.33$$

$$p_1 = N_V \exp\left(\frac{E_V - E_t}{kT}\right). \quad 3.34$$

Therefore, all variables used in the equations of SRH recombination can be expressed by the trap density (N_t), trap energy level (E_t) and the capture coefficients of electrons and holes ($\langle c_n\rangle$ and $\langle e_n\rangle$).

3.4 Summary

In this chapter, the experimental and numerical methods used in this thesis are described, including the chemical processes of fabricating perovskite films, the optical and electrical characterisation by two confocal microscope systems, and the modelling of laser heating and recombination kinetics. The fabricated perovskite films are used in the experiments discussed in Chapter 4 - 6. The WITec system was used in the preliminary studies (Section 4.1 and 4.3) and the investigation of oxygen-induced PL enhancement in Chapter 5. The Horiba system was used for measuring the steady-state PL spectra and time-resolved PL lifetime demonstrated in Chapter 6. In Section 4.2, the laser heating model is applied to estimate the laser-induced temperature rise in perovskite films during the measurements. Lastly, the recombination model is used to fit the experimental results measured in Chapter 6 and to investigate the interpretation of carrier lifetime in Chapter 7.

Chapter 4 Preliminary and supporting studies

This chapter is a collection of several supporting studies carried out in the early stages of the thesis. The first section describes the use of confocal scanning microscopy to spatially image the reflection and photocurrent of a silicon thin-film solar cell. The second section estimates the laser induced local temperature rise of perovskite films during confocal PL measurements. In the last section, a detailed stability analysis of perovskite films in different measurement environments is shown.

4.1 High-resolution reflectance and photocurrent imaging

This work has been presented at the 2014 OSA Light, Energy and the Environment Conference. It has been published in the following conference paper: X. Fu, E.-C. Wang, K. R. Catchpole and T. P. White, "High-resolution photocurrent imaging of light trapping by plasmonic nanoparticles on thin film Si solar cells," in *Light, Energy and the Environment*, OSA Technical Digest JW6A.27., 2014.

4.1.1 Introduction

Photocurrent imaging is a useful tool for studying film uniformity in perovskite cells. After setting up the measurement equipment, a Si thin-film solar cell coated by Ag nanoparticles was used to test the system. In this section, reflectance and photocurrent mapping, as obtained by a scanning confocal microscope, provide a direct observation of the influence of Ag nanoparticle arrays at the wavelength scale. Plasmonic light trapping effects are demonstrated by both experimental and modelling results.

4.1.2 Experiments and discussion

A WITec alpha300 S scanning confocal microscope combined with a broadband tunable light source and a lock-in amplifier are used to enable simultaneous reflectance and photocurrent imaging down to the diffraction limit. Detailed descriptions of this experiment (Section 3.2.1) have been shown in Chapter 3. A thin film polycrystalline Si solar cell (Figure 4.1) [101] with a Ag nanoparticle array was tested using the photocurrent mapping technique described above. This thin film solar cell was fabricated for previous work for investigating light trapping effect [101]. Figure

4.2 shows the structure of this cell. The substrate consists of $\sim 3\ mm$ glass and $100\ nm$ Si_3N_4. Above these layers are a $2\ \mu m$ Si active layer and a $10\ nm$ SiO_2 layer. A square array of Ag nanoparticles with $400\ nm$ diameter and $513\ nm$ period was formed on the top of this cell by nanoimprint lithography and thermal evaporation [101]. This configuration is proved to effectively enhance light absorption of this thin film solar cell in the 550-850 nm wavelength range [101].

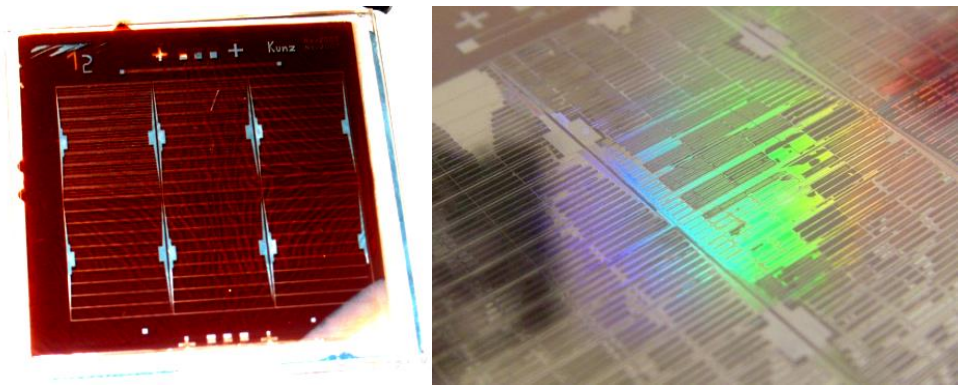

Figure 4.1 Photos of the Si thin film solar cell.

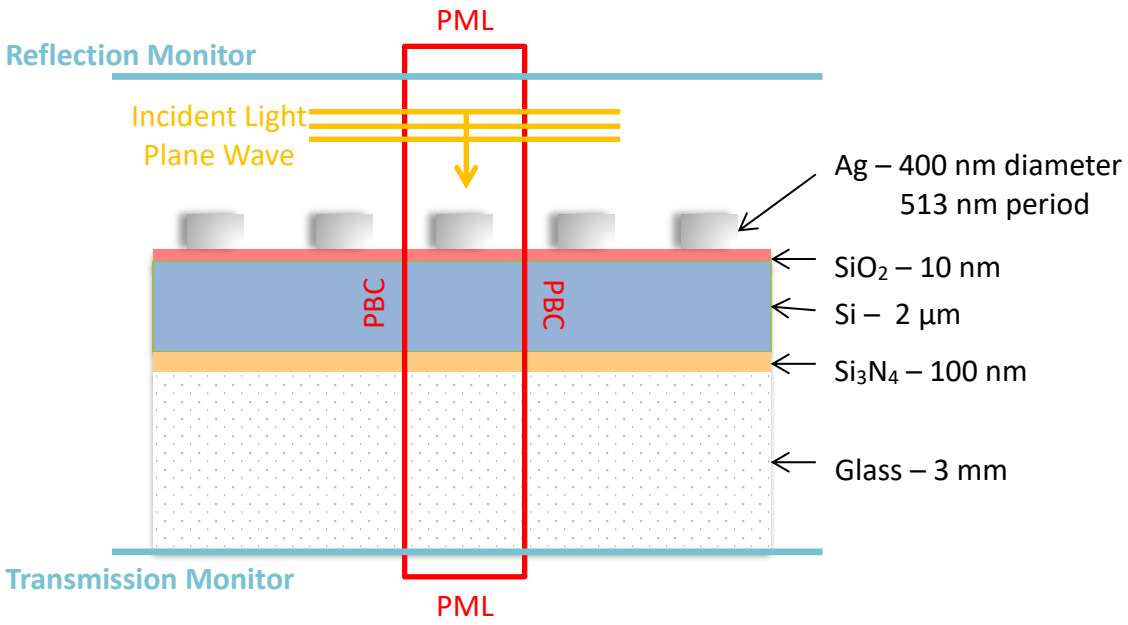

Figure 4.2 The structure of the measured Si thin film solar cell and the configuration of modelling.

Reflectance and photocurrent images of this cell are shown in Figure 4.3 for four representative wavelengths: $550\ nm$, $690\ nm$, $760\ nm$ and $1000\ nm$. The selected area of the cell has a number of particles missing, providing a direct comparison between regions with and without the nanoparticles. It can be seen that the Ag particles have a high reflectance under short wavelength (visible) light, which negatively affects the photocurrent generation. However, under long wavelength (near

infrared) laser exposure, both the reflectance and photocurrent generation are higher for the region covered by Ag array. Note that, above $800\ nm$, the individual particles can no longer be resolved due to their subwavelength dimensions, however the area without the nanoparticles is clearly seen as a dark band on the right-hand side of the figures.

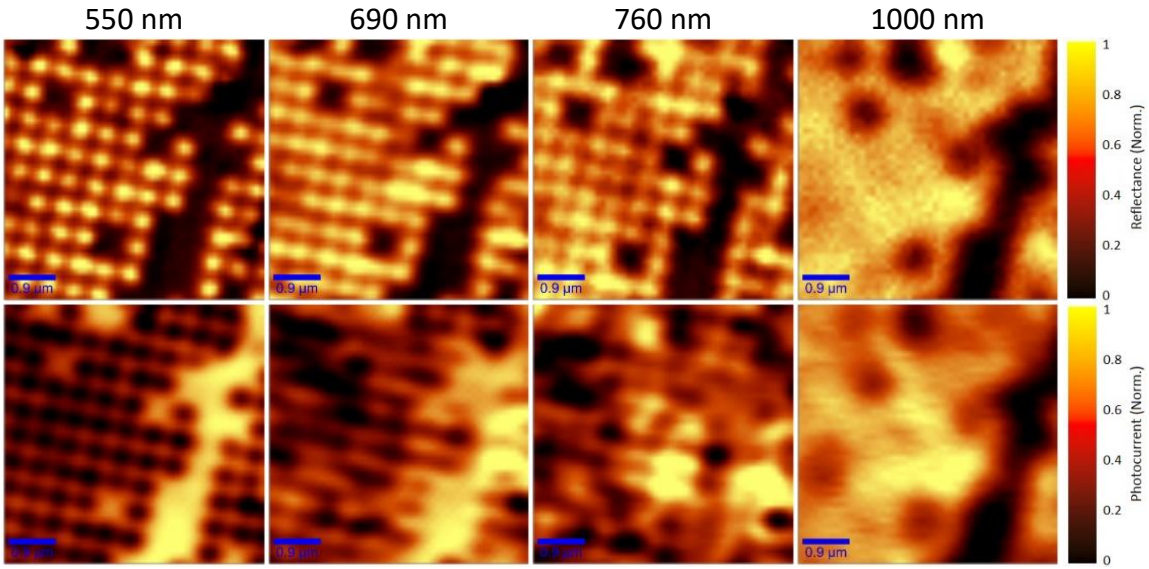

Figure 4.3 The images of reflectance (the first row) and photocurrent (the second row) of Si thin film solar cell measured under laser wavelengths of 550 nm, 690 nm, 760 nm and 1000 nm. The area with the missing particles is considered as 'exposed (planar) cell surface'. The integration time of each pixel is 3 ms and there are 10 pixels per nanometre.

In order to compare the experimental results with theoretical predictions, a finite difference time domain model (Lumerical FDTD Solutions) was applied to simulate the reflectance and absorptance of this cell structure. A unit cell with one Ag particle on top of the Si thin film cell is illustrated in the simulation window (Red rectangle in Figure 4.2) and is extended horizontally using the Periodic Boundary Condition (PBC). The front light source is set to be a plane wave with wavelengths from 400 nm to 1000 nm. A reflection monitor and a transmission monitor are placed on the top and rear of the cell, respectively, in order to detect the reflectance (R) and absorptance ($A = 1 - R - T$) of the cell under the incident light with different wavelengths, where T is the detected transmittance. Outside the monitors, the boundary conditions are set to be the Perfect Match Layer (PML), which act as ideal absorbing boundaries. The photogenerated current of a solar cell is approximately proportional to the efficiency of light absorption [102]. Thus, the absorptance of the solar cell is used as an indicator of photocurrent in the simulation.

From the scanned images, the average reflectance and photocurrent for the region covered by Ag particles (R_p and I_p of particle area) are calculated and compared with the values in the region where there are no Ag particles (R_s and I_s of surface area). The ratios of reflectance and photocurrent calculated from the experimental data are plotted in Figure 4.4 a and b respectively. It is shown that the Ag array reflects more light than the Si surface at all wavelengths; however, the photocurrent generated by the Ag covered region is higher at long wavelengths. In Figure 4.4 c and d, the result simulated by FDTD displays a similar trend for both reflectance and absorptance ratios (R_p and A_p are the reflectance and absorptance of the unit cell with Ag particle; R_s and A_s are the reflectance and absorptance of the unit cell without Ag particle), consistent with the calculations by Spinelli [103]. The fluctuations in those results are caused by optical interference within the 2 μm Si layer. This result demonstrates that despite the increased reflectance of the nanoparticle region at all wavelengths, the total absorption is increased at longer wavelengths due to effective light trapping by the Ag nanoparticles [103].

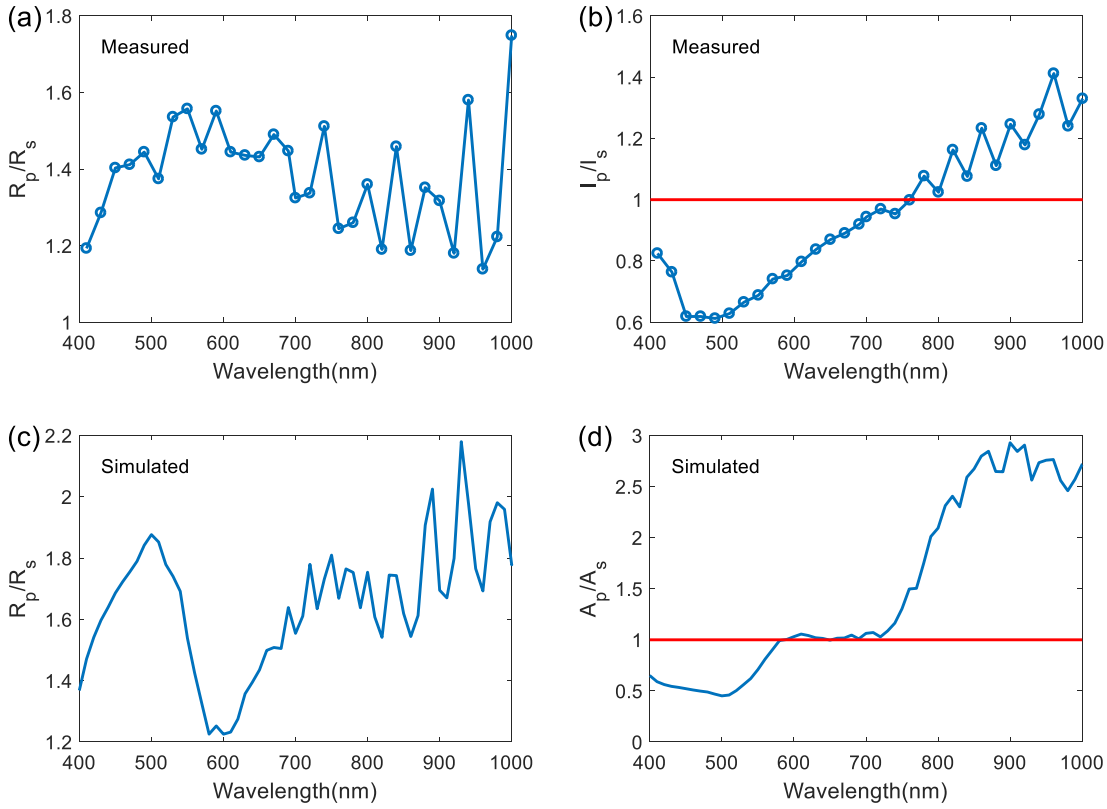

Figure 4.4 (a) The ratio of reflectance and (b) the ratio of photocurrent for the region covered by Ag particles and the region without Ag particles based on experiment data. (c) The ratio of reflectance and (d) the ratio of photocurrent for the region covered by Ag particles and the region without Ag particles based on simulation. The red line indicates the critical level where the generated photocurrents are the same at both regions.

A 2D simulation of extinction spectrum is performed where the (400 nm diameter, 50 nm high) cylindrical particles are approximated by their rectangular cross-section as indicated in Figure 4.2. The extinction cross-section of the Ag nanoparticles is calculated using the commercial Finite Element Method software COMSOL Multiphysics V5.4. Figure 4.5 shows the normalised scattering, absorption and extinction (scattering + absorption) cross-sections for a 400 nm wide Ag particle on top of a Si substrate coated with a 10 nm SiO_2 layer. It is calculated for 'TM' polarisation, where the electric field is in the simulation plane. This allows the incident light to excite surface plasmon polaritons similar to those that would be excited in the actual 3D geometry [104]. Thus, this simplification should give qualitative agreement with the full 3D geometry.

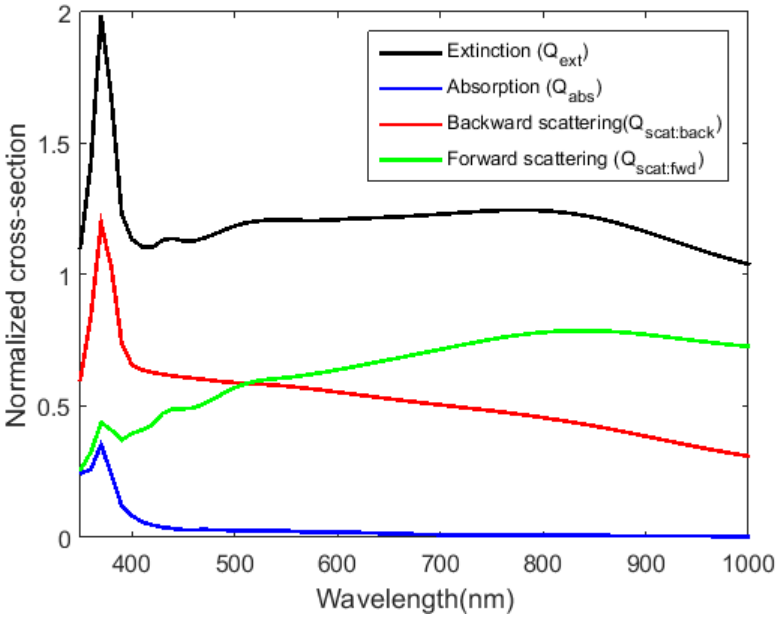

Figure 4.5 Simulated scattering, absorption and extinction cross-sections of Ag nanoparticles.

Figure 4.5 demonstrates that the extinction cross-section is quite flat across most of the spectrum, with the only distinct feature being a strong plasmonic resonance below 400nm. The broad, relatively weak response is a result of the particles being quite large, so they support a number of overlapping resonances rather than a small number of discrete resonances as in the case of Fig. 1 of ref. [104]. At shorter wavelengths the backward scattering dominates, consistent with the high reflection that is observed experimentally, but forward scattering begins to take over for wavelengths beyond 500nm, and by 1000nm, the forward scattering is almost double the back scattering.

This is also consistent with the experimental data that shows reduced reflection and increased photocurrent at longer wavelengths.

4.1.3 Conclusion

In summary, the optical absorption and photocurrent enhancement by Ag nanoparticles in Si thin film solar cells is demonstrated by combined reflectance and photocurrent scanning microscopy. Plasmonic light trapping is one of several promising approaches for increasing the efficiency of thin film Si solar cells. Although metal nanoparticles on top of the solar cell are known to have a detrimental effect on light absorption at short wavelengths due to increased reflection losses, these particles can enhance absorption and photocurrent at long wavelengths due to light trapping.

This experiment demonstrates the capability of confocal scanning microscope as an imaging tool. However, photocurrent mapping on perovskite solar cells was not used in the rest of the thesis. Since the front side of the perovskite cell is behind the glass substrate, the achievable resolution was limited, and does not allow individual perovskite grains to be resolved. Instead, confocal PL mapping was applied on perovskite film in the studies demonstrated in Chapter 5.

4.2 Laser heating

4.2.1 Introduction

One of the key features of confocal microscopy is that a focussed laser beam is used for excitation, which leads to a concern of the local heating induced by laser excitation on the perovskite films. As shown in the relevant literature (Section 2.3.1), perovskite films easily degrade under high temperature. Very high excitation intensities can occur in a confocal microscope since the laser spot sizes are only few micrometres as shown in Figure 3.4 and Figure 3.11. Also, sometimes relatively high intensities are required to extract a strong signal for PL and/or Raman measurements. This leads to the possibility of thermal damage, and thus it is important to understand the potential heating of samples under focussed laser light, and the thresholds beyond which the samples start to degrade. In addition, in the following work on the modelling of the recombination kinetics (Chapter 6), many parameters such as n_1 and p_1 are temperature dependent. The operation temperature must be clarified when using the recombination model to

fit the experimental data. Therefore, an analytical solution is used to estimate the temperature increase caused by laser heating.

4.2.2 Modelling results

The equations used for estimating laser-induced heating have been listed in Section 3.3.1. To validate the model, the result from the textbook (Figure 7.2.3 in [98]) is reproduced based on the provided parameters of a Si thin film (Figure 4.6).

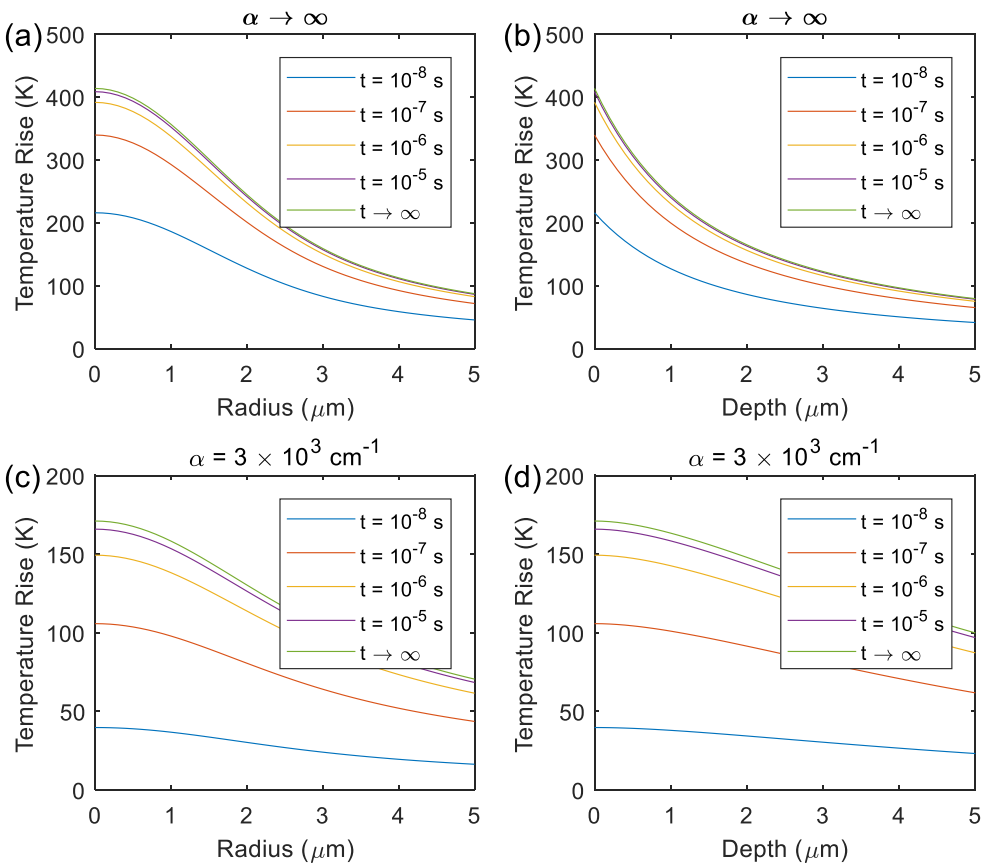

Figure 4.6 Temperature distribution in (a and c) radial and (b and d) axial directions for various durations of laser irradiation. Upper part (a and b): strong absorption with $\alpha \to \infty$. Lower part (c and d): finite absorption with $\alpha = 3 \times 10^3\ cm^{-1}$.

For the simulation on perovskite films, the optical properties including absorption coefficient α [105] and reflectivity R [106], can be found in the literature. However, the thermal properties of perovskite films have not been fully elucidated. More importantly, the thermal properties of the glass substrate (1 mm thick), where the thin layer of perovskite film (300 nm thick) is always deposited, are likely to dominate the thermal dynamics of perovskite films. Thus, the parameters of substrate thermal conductivity κ_{sub}, substrate density ρ, and specific heat capacity of substrate C_p in this

model are the properties of the soda-lime glass substrates [107]. Thus, surface conductance $\eta = \kappa_{air}/l$, and heat diffusivity $D = \kappa_{sub}/(\rho \cdot C_p)$. The values of those constants are listed in Table 4.1. Here, the smallest laser spot size $w_0 = 0.9 \times 10^{-4}\ cm$ achievable in experiment (see Figure 3.4a) is used for calculating the potential laser intensity.

Table 4.1 Input parameters in the model of laser heating on perovskite films.

$\alpha\ (cm^{-1})$ @ $532\ nm$	1.5×10^4
R	0.21
$\kappa\ (W/(cm \cdot K))$	2.4×10^{-4}
$\eta\ (W/(cm^2 \cdot K))$	4.8
$D(cm^2 s^{-1})$	4.8×10^{-3}
$h_s\ (cm)$	0.10

With the parameters listed in Table 4.1, Figure 4.7a demonstrates that the temperature increases by only $6\ K$ at the centre of the laser exposed area under an extremely high laser intensity of $10^4\ W cm^{-2}$. The temperature of the film is expected to saturate after $1\ ms$ of illumination (Figure 4.7b). The surface temperature profile exhibits a Gaussian characteristic due to the shape of laser beam. The surface temperature rise reduces to zero when the distance away from the centre is greater than $10\ \mu m$ (Figure 4.7c). The laser induced heat is exponentially reduced along the depth of the film, so that within the thickness of the perovskite layer ($200\ nm$) the increased temperature varies between $1 \sim 2\ °C$ (Figure 4.7d).

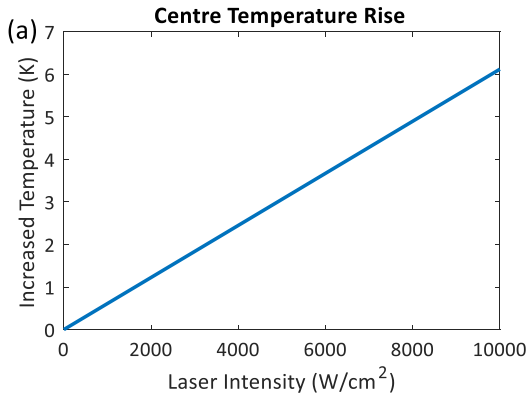

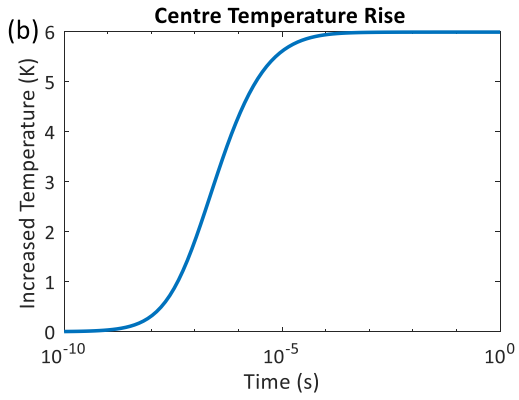

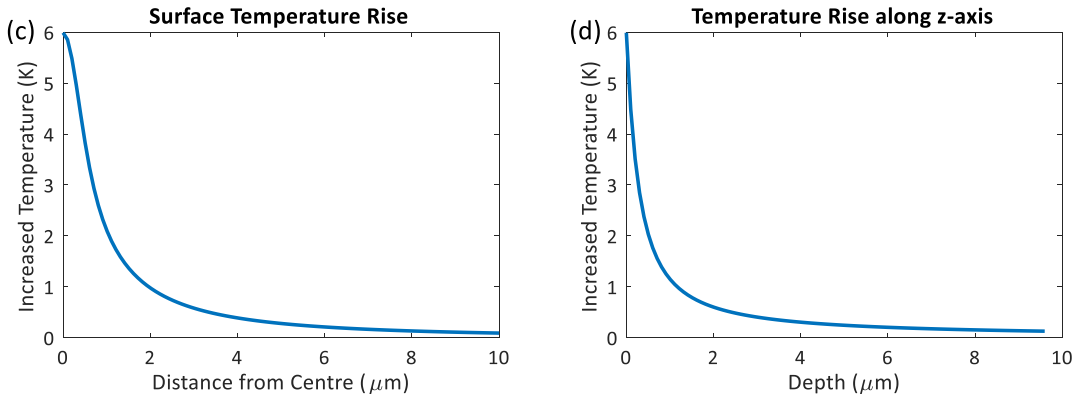

Figure 4.7 Temperature distribution of a perovskite film under laser exposure: (a) centre temperature rise as a function of laser intensity; (b) centre temperature rise as a function of laser exposure time; (c) surface temperature distribution under laser exposure; and (d) centre temperature rise as a function of depth.

This level of temperature variation is negligible during the measurements of perovskite films, and thus the thermal-induced degradation is unlikely to occur. Therefore, when modelling the recombination kinetics of perovskite films under the measurement condition, temperature-dependent parameters can be considered as constants at room temperature.

4.2.3 Conclusion

In conclusion, an analytical solution of laser heating on thin films is applied to estimate the potential local temperature increase of perovskite films in the experimental conditions using confocal microscope. It demonstrates that thermal-induced degradation is not a major concern in the characterisation of perovskite films, provided that the laser intensity and spot size are chosen appropriately. The estimated operation temperature is also useful for modelling the recombination kinetics of perovskite materials in Chapter 6.

4.3 Perovskite film stability

4.3.1 Introduction

The challenges of characterising perovskite solar cells have been discussed in Section 2.2, particularly in relation to the stability of the films during measurements. Thus, it is necessary to investigate the perovskite film stability and ensure that the film is not degraded during the measurements.

4.3.2 Experiments and discussion

In this section, the Raman and PL intensities are used as indicators of the film quality. First, the results for a bare $CH_3NH_3PbI_3$ perovskite film deposited on a glass substrate are presented as measured by a Renishaw inVia confocal Raman microscope. The Raman spectra are extracted every 10 min. The vibrational frequency of the inorganic cage (Pb-I) of $CH_3NH_3PbI_3$ polycrystal is below 150 cm^{-1} [108]. As shown in Figure 4.8, over 50 min, the peak at around 110 cm^{-1} appears and continuously increases indicating the decomposition of $CH_3NH_3PbI_3$ into $CH_3NH_3I_2$ and PbI_2. This result agrees well with the Raman spectra reported by Ledinský (Figure 2 in [31]).

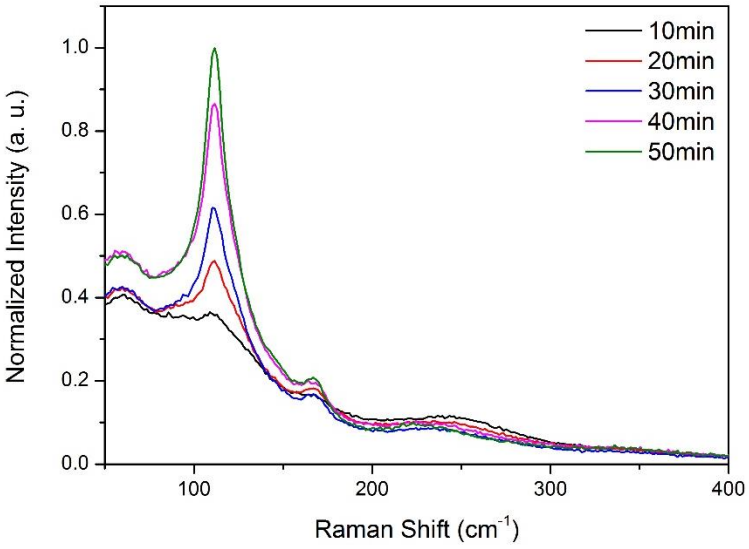

Figure 4.8 Raman spectra of a $CH_3NH_3PbI_3$ perovskite film measured after 10 min, 20 min, 30 min, 40 min and 50 min laser exposure.

Similarly, the PL intensity is detected over tens of minutes to investigate the film stability. For the bare perovskite film, the PL intensity of the $CH_3NH_3PbI_3$ peak (1.6 eV) is reduced dramatically under illumination (black curve in Figure 4.9). After 30 min, the PL intensity drops to zero, indicating almost complete degradation of the perovskite film. However, an unexpected increase during the first 10 min is detected for almost all samples.

Next, perovskite films coated by 200 nm thick PMMA are measured for comparison, since the PMMA layer should protect the perovskite films from moisture [109]. The red curve in Figure 4.9 indicates that the PMMA coating can effectively protect the

perovskite film over at least 40 min without any degradation, but the PL enhancement still occurs.

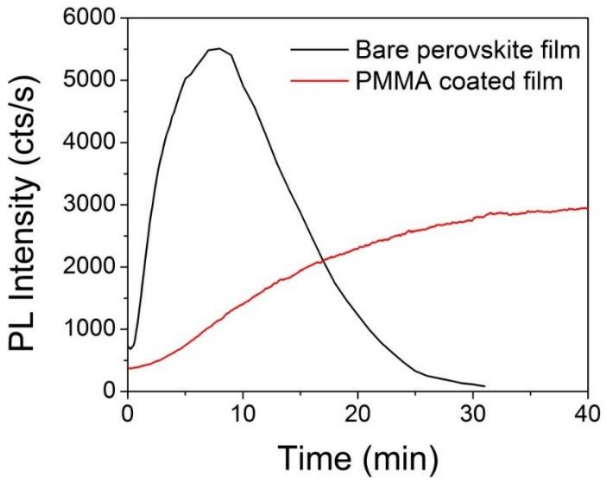

Figure 4.9 Time-resolved PL changes of a bare perovskite film (black) and a film coated with PMMA (red).

Although the PMMA layer can prevent moisture from entering the perovskite film, it is possible that other gases in air can still penetrate through PMMA. Further investigation has been performed by measuring the PMMA coated perovskite films and fully encapsulated perovskite films. In order to eliminate the effects of interfaces and make sure the films absorb the same amount of photon flux, the laser is excited from the glass side and additional layers of epoxy and glass are added in front of the light (Figure 4.10 a and b). The measured PL intensity shows that the fully encapsulated film is very stable while the PMMA coated film shows an obvious increase in PL intensity (Figure 4.10c). This experiment indicates that there should be one or more types of gases in air which can diffuse into perovskite films and have a positive impact on the PL performance of perovskite films. The coated PMMA layer with different thicknesses leads to different timescales of PL enhancement of perovskite films. This indicates that the thickness of PMMA coating affects the penetration of gases into the perovskite film.[3]

[3] A PMMA film with denser molecular weight can also reduce the penetration of air into the perovskite layer.

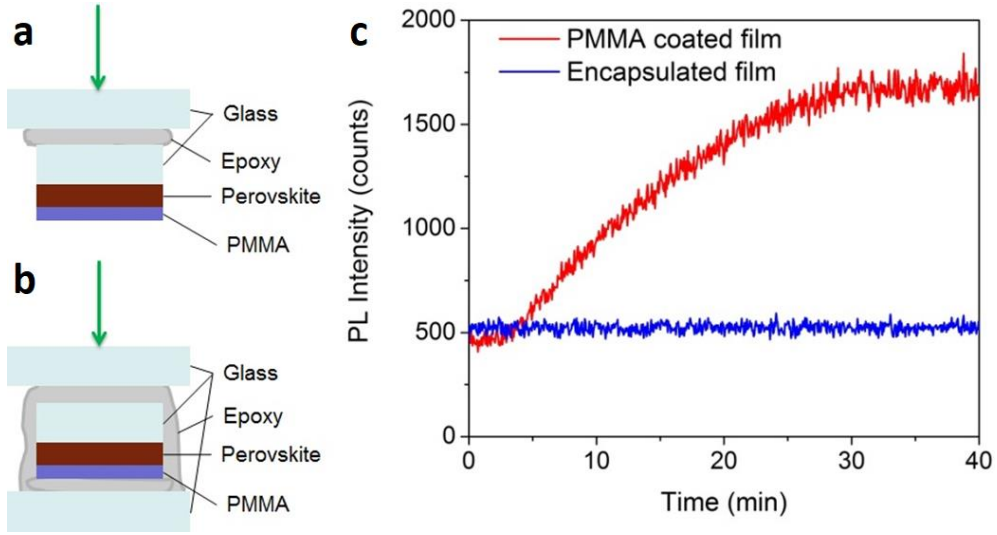

Figure 4.10 Schematic diagram of (a) PMMA coated perovskite film and (b) fully encapsulated perovskite film in this experiment. (c) Time-resolved PL changes of the two types of films under same test condition. The red line indicates a PL increase of the PMMA coated film with laser illumination; the blue line shows that the PL intensity of the encapsulated film does not change.

The PMMA coated perovskite films are then measured inside an enclosed chamber filled with N_2 gas. Both $CH_3NH_3PbI_3$ and $Cs_{0.07}Rb_{0.03}(FA_{0.85}MA_{0.15})_{0.9}Pb(I_{0.85}Br_{0.15})_3$ perovskite films show great stability in the N_2 environment (Figure 4.11). This proves that it is not the effect of N_2 that improves the PL intensity of perovskite films.

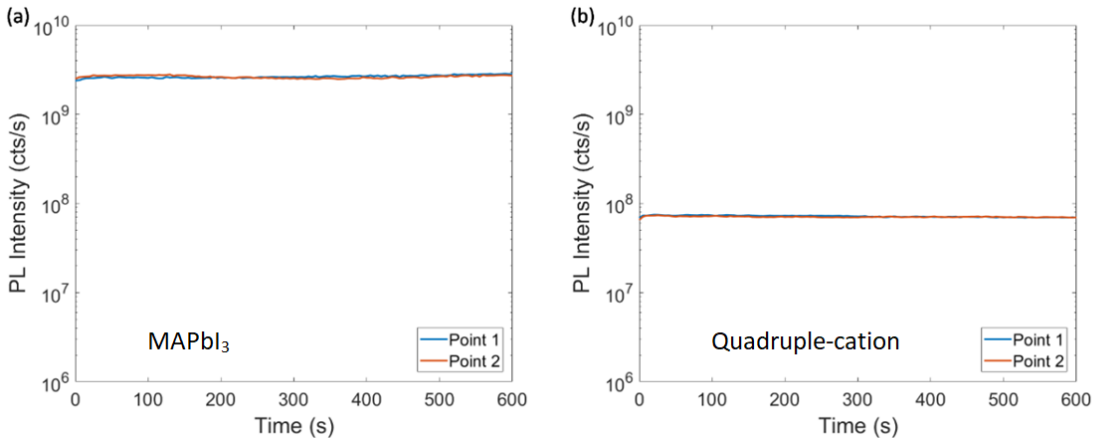

Figure 4.11 Time-dependent PL intensity measured on a single spot over 600 s on (a) $MAPbI_3$ film and (b) quadruple-cation film at the maximum laser intensity. The measurements are taken on the area of the sample that had been measured (Point 1) and on a non-exposed area (Point 2).

4.3.3 Conclusion

The decomposition of perovskite films is monitored by time-dependent Raman and PL measurements. The PL enhancement of perovskite films measured in air is also observed and a further study of this phenomenon will be discussed in Chapter 5. Comparing the bare films and the PMMA coated films, the PMMA coating appears to

be effective at protecting the perovskite films from degradation. Finally, to ensure the stability of the perovskite films during the experiments, the films must be fully encapsulated by epoxy or kept in a N_2 environment.

4.4 Summary

In this chapter, preliminary experimental and modelling results are shown to support the main purpose of this thesis – characterising perovskite films. Confocal reflectance and photocurrent mapping on Si thin film solar cells demonstrate the capability of high resolution optical and electrical characterisation using confocal scanning microscope. Laser-induced local heating estimation on perovskite films shows a negligible effect. The estimated temperature is also used to analyse the temperature-dependent parameters in the recombination model. Furthermore, a detailed stability analysis of perovskite films under different ambient environments has been investigated using confocal Raman and PL measurements. It suggests that PMMA coated perovskite films can survive for more than 40 min under standard experimental condition without degradation. However, PL enhancement cannot be avoided in this case. The samples should be kept in N_2 gas chambers to ensure their stability during the measurements.

Chapter 5 Photoluminescence study of trap de-activation in perovskite films

The contents of this chapter have been published in the following journal article: X. Fu, D. A. Jacobs, F. J. Beck, T. Duong, H. Shen, K. R. Catchpole and T. P. White, "Photoluminescence study of time- and spatial-dependent light induced trap de-activation in $CH_3NH_3PbI_3$ perovskite films," *Physical Chemistry Chemical Physics*, Vol. 18, No. 32, pp. 22557-22564, 2016. Section 5.2.6 is contributed by D. A. Jacobs.

This study was completed in June 2016. There have been a number of further studies of O_2-related PL enhancement mechanisms since the work was published, which will be discussed in Section 5.4.

5.1 Introduction

With a band gap of 1.6 eV, the theoretical maximum open circuit voltage (V_{OC}) of $CH_3NH_3PbI_3$ perovskite solar cells can reach ~1.3 V [110]; however, the highest reported V_{OC} is just over 1.1 V [111]. This gap indicates that non-radiative recombination losses in perovskite films have the potential to be reduced significantly. Non-radiative recombination in perovskite films is dominated by Shockley-Read-Hall (SRH) recombination at typical solar intensities, while the contribution of Auger recombination is considered to be very low [112]. In the bulk, the non-radiative recombination has been attributed to charged traps such as Pb vacancies, methylammonium and iodide interstitials, PbI_3^-, and I-Pb antisites [42, 113-116]. As a new photovoltaic material, there are still many unknown aspects related to the recombination kinetics under different conditions. In order to improve the V_{OC} of perovskite solar cells, it is important to develop a comprehensive understanding of their recombination mechanisms.

Stranks *et al* proposed a theoretical model to quantify radiative and SRH recombination in perovskite films, and fitted the model parameters using a combination of PL decay and Photoluminescence quantum efficiency (PLQE) measurements [72]. In their work, dynamic, short timescale (μs), interactions between free carriers and sub-gap defects in $CH_3NH_3PbI_xCl_{3-x}$ thin films were demonstrated.

Many groups have observed PL intensity enhancement in perovskite films with light exposure ranging over time scales from seconds to hours [41, 42, 67, 72, 117]. Several studies attributed this phenomenon to the slow filling of bulk traps by photogenerated carriers [67, 72, 117]. However, by measuring the PL emission of perovskite films that are exposed to different atmospheres, Galisteo-López and Tian found that with the help of oxygen-related species, photocarriers could effectively de-activate (or ‘‘cure’’) traps in the bulk of the perovskite film, resulting in a dramatic increase in PL intensity [41, 42]. The distinction between trap filling and trap deactivation requires some clarification. Both occur when photogenerated carriers interact with a defect, and once a carrier is trapped by a defect, it becomes temporarily inactive (i.e. it cannot trap another carrier) until the first is released. Here, charge trapping refers to the dynamic process whereby defects repeatedly trap and release carriers (either via non-radiative recombination or thermal excitation back into their excited state), reaching equilibrium when trapping and de-trapping rates balance. At equilibrium a constant proportion of traps are occupied at any given time, with the proportion depending on the trap and carrier densities, and the trapping and de-trapping rates. In contrast, the term trap de-activation is used to describe a (yet to be identified) photochemical reaction that reduces the overall density of unoccupied (‘active’) traps either permanently, or on a timescale many orders of magnitude larger than the typical trapping and de-trapping times extracted from experimental measurements [72]. This change in the trap density affects the charge trapping equilibrium conditions and thus the radiative and non-radiative recombination rates. The observed enhancement in PL intensity has also been correlated to an improvement in carrier diffusion length and lifetime [42, 67]. An increase in carrier lifetime from 3 ns to greater than 200 ns following exposure to light and oxygen was attributed to trap de-activation, leading to a deeper penetration of carriers into the perovskite film. Large lateral carrier diffusion has also been observed in perovskite films using a combination of localised excitation and PL imaging techniques. Handloser *et al* were able to detect PL emission several micrometres away from the excitation region in films of $CH_3NH_3PbI_xCL_{3-x}$ [67]. From these measurements, carrier diffusion lengths were estimated to lie in the region of 5.5–7.7 µm after 10 h of light exposure.

Numerous experiments with various samples and test environments have been performed to study the dramatic light-induced PL enhancement over long timescales; however no coherent model has yet been presented to quantitatively describe these observations. In this work confocal photoluminescence mapping technique is applied to investigate the temporal and spatial dependence of trap de-activation in perovskite films. In particular, it is shown that local illumination of $CH_3NH_3PbI_3$ films can produce a dramatic increase in photoluminescence emission over timescales of minutes, and that these changes can extend several microns beyond the illuminated region. These changes are attributed to a trap de-activation dominated mechanism involving photogenerated carriers and oxygen, where the lateral extent of these changes is determined by the local carrier diffusion properties, rather than the alternative possibility of trap diffusion. A previously proposed trap-filling model [72] is extended to include an additional trap de-activation term to describe the observed time-dependent PL changes in the excitation region. The model is fitted to experimental measurements to derive an estimate of the trap de-activation rate in the presence of photogenerated carriers and oxygen. Then, in the second part of this work trap de-activation is included in a rigorous numerical spatial and temporal diffusion model to demonstrate the plausibility of lateral trap de-activation outside the excitation region. This work has important implications for understanding the recombination mechanisms in perovskite films, and for improving the performance of perovskite solar cells.

5.2 Results and discussion

5.2.1 Observation of laser induced PL enhancement

All of the experiments in this work were performed on planar $CH_3NH_3PbI_3$ thin films deposited on glass (Figure 5.1b, inset) using a single-step solution process as described in Section 3.1. This produces a uniform, smooth film with few pinholes, and negligible light scattering from surface features. The size of the perovskite grains formed was around 200 nm, as shown in the SEM image (Figure 3.1). Planar perovskite cells produced by the same film fabrication process performed well with an efficiency of 14.65% (Figure 3.2), confirming the high quality of the material. The perovskite films were then coated with PMMA prior to performing photoluminescence measurements. Experiments (Section 4.3) suggest that a thin layer of PMMA (~200 nm) can effectively

protect perovskite films from moisture-related degradation at the timescale of the measurement (Figure 4.9), while still allow us to observe a strong increase in photoluminescence (Figure 4.10). It is inferred from this observation that sufficient oxygen can diffuse through the PMMA film to react with the photogenerated carriers in the perovskite. In Figure 5.1, the perovskite film was continuously illuminated by a 532 nm excitation laser, and the PL spectra were recorded in 10 minutes intervals. In single point PL measurements, a 10× objective lens was used to focus the laser beam. The laser spot size was around 8 µm (Figure 3.4a), much larger than the grain size (~200 nm), and as a result, the detected PL intensity is an average of signals from several grains and grain boundaries. For this sample, the peak PL intensity of perovskite increased by a factor of 8 and saturated after 30 minutes of illumination. It is noted, however that some films studied can display PL enhancement ratios of more than two orders of magnitude. It can be seen in Figure 5.1a that the peak emission wavelength remains constant throughout the measurement. If there was significant local heating by the excitation laser, a blue-shift of PL spectra should be observed [118, 119]. Furthermore, any thermally-induced structural or phase changes would likely result in a shift in the PL peak position or a change in the shape of the PL spectrum [120]. Therefore, the stable emission spectrum indicates that the sample temperature remains constant, and there are no significant structural or phase changes within the film.

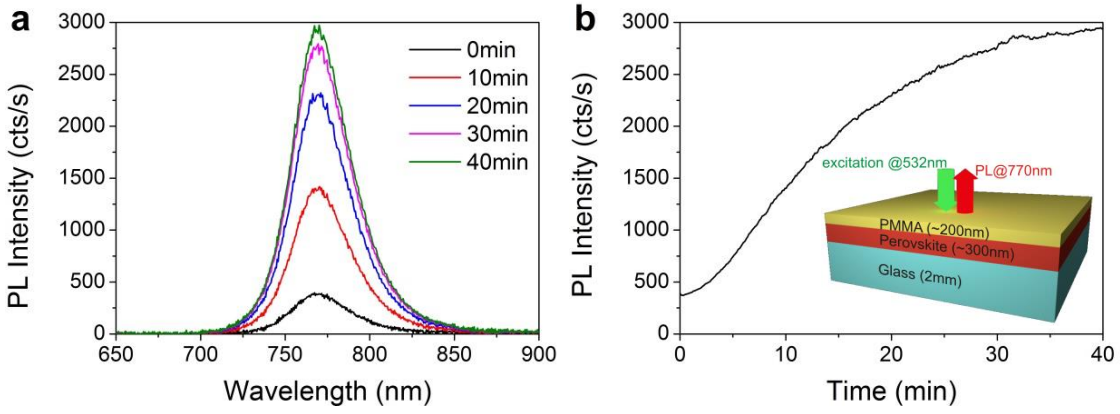

Figure 5.1(a) PL spectra of perovskite film during continuous laser exposure, measured at 0 min, 10 min, 20 min, 30 min and 40 min. (b) PL peak intensity as a function of laser exposure time. The laser intensity is approximately 150mWcm^{-2}. Inset is the schematic of the perovskite film sample measured in this experiment.

It is found that samples fully encapsulated under glass and epoxy in a nitrogen environment do not exhibit any significant PL enhancement under illumination

(Section 4.3). The strong PL enhancement is only observed for bare films exposed directly to air, or films coated in a thin layer of PMMA. This is in agreement with measurements performed by other groups under controlled atmosphere conditions which have identified the key role of oxygen in the PL enhancement process [41, 42]. It has been proposed that unknown product(s) generated by a photo-induced reaction with oxygen could de-activate traps in the bulk and/or on the surface of the perovskite films.

5.2.2 Modelling time-dependent PL enhancement

First, a simple recombination model described in ref. [72] is used to show that the long timescale light-induced PL enhancement observed in the region directly exposed to the laser illumination can be quantitatively described by including a trap de-activation term. Equation 5.1-5.3 are based on the recombination model from ref. [72] which was used in that work to fit PL decay and PLQE data. The original recombination model in ref. [72] only considered the role of trap filling processes in the carrier recombination, while treating total trap density N_T as a constant.

$$\frac{dn_e}{dt} = G - PL - R_{trap} n_e (N_T - n_T) \quad 5.1$$

$$\frac{dn_T}{dt} = R_{trap} n_e (N_T - n_T) - R_{detrap} n_h n_T \quad 5.2$$

$$PL = R_{PL} n_e n_h \quad 5.3$$

n_e, n_h, N_T and n_T represent the concentration of free electrons and holes, total trap density and the density of filled traps respectively. The parameters R_{trap} and R_{detrap} are the rate of free electrons trapped by defects and the rate of hole capture. R_{PL} is the radiative recombination rate of free electrons and holes. A detailed explanation of Equation 5.1-5.3 is given in ref. [72]. Here, an electron trapping nature is assumed as in ref. [72]. Electron traps have previously been identified as the dominant source of trap-assisted recombination in $CH_3NH_3PbI_3$ by comparing electron-only and hole-only devices [121] and directly characterising trap states [122, 123]. The contribution due to excitons is also ignored, since the exciton binding energy is low enough to enable charge separation at room temperature [124, 125]. As in the original model, thermal emission of electrons from the traps to the conduction band is ignored [72]. The values

deduced in ref. [72] from PL decay and PLQE experiments were listed in Table 5.1. With these parameters, the model predicts a rapid initial PL increase during the first 5–10 µs of exposure before saturating (Figure 5.2a). If the timescale is intended to fit to the experiment result shown in Figure 5.1b, all of the rates need to be reduced by more than ten orders of magnitude, which are far below the reasonable recombination rates (Figure 5.2b). Thus, trap filling alone does not appear to be sufficient to explain the much longer timescales of PL enhancement shown in Figure 5.1, although such a mechanism has been proposed [67, 72, 117]. Furthermore, a simple trap-filling mechanism is not consistent with the observed dependence on ambient conditions as shown in Figure 4.10. It should be noted that ref. [72] also reported PL increases over more than 20 s, but did not attempt to fit the recombination model to these results.

Table 5.1 Parameters used in the recombination model

Parameters	***Values***
R_{trap}	$2 \times 10^{-10}\ cm^3 s^{-1}$
R_{detrap}	$8 \times 10^{-12}\ cm^3 s^{-1}$
R_{PL}	$1.3 \times 10^{-10}\ cm^3 s^{-1}$
N_T	$2.5 \times 10^{16}\ cm^3$

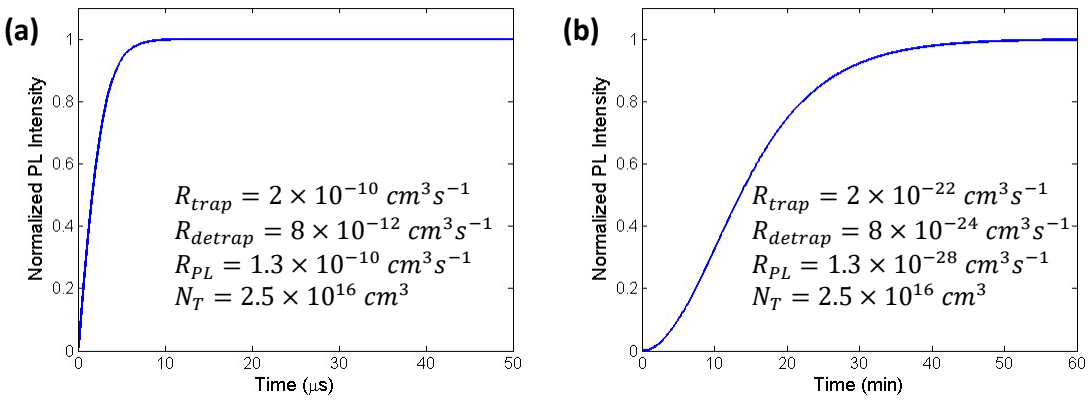

Figure 5.2 Modelled PL increase with constant trap density (a) using reasonable rates and (b) using rates that can fit the measured timescale.

Since it has been proposed that bulk traps can be de-activated by a combination of photogenerated carriers and oxygen, the situation should be considered where the total trap density N_T in Equation 5.1-5.3 decreases over time as a function of the

remaining trap density and the electron density. For simplicity, a constant trap de-activation rate R_{N_T} is assumed, and the time-dependent trap density can be expressed as

$$\frac{dN_T}{dt} = -R_{N_T} N_T n_e. \qquad 5.4$$

Note that the trap de-activation rate R_{N_T} should also be related to the concentration of oxygen in the film since it is assumed that this is an oxygen-related trap de-activation process. Using the same rate values quoted above for R_{trap}, R_{detrap}, R_{PL} and initial N_T, and setting $R_{N_T} = 2.5 \times 10^{-19}\, cm^3 s^{-1}$, the revised model can reproduce the slow increase of PL over tens of minutes (Figure 5.3). The rapid increase of PL intensity (from zero) due to trap filling can still be observed in the first 10 µs (Figure 5.3, inset), but this is too rapid to detect in the measurement set-up. This simple model shows that the addition of a time-dependent trap density to represent the trap de-activation due to photogenerated carriers and oxygen can qualitatively reproduce the observed slow increase in PL emission observed in Figure 5.1, and in reports by others [42, 117]. By varying the incident power for a single set of fitting parameters, the power dependent PL increase indicated in Figure 3(a) of ref. [41] is also reproduced without the degradation region (Figure 5.4).

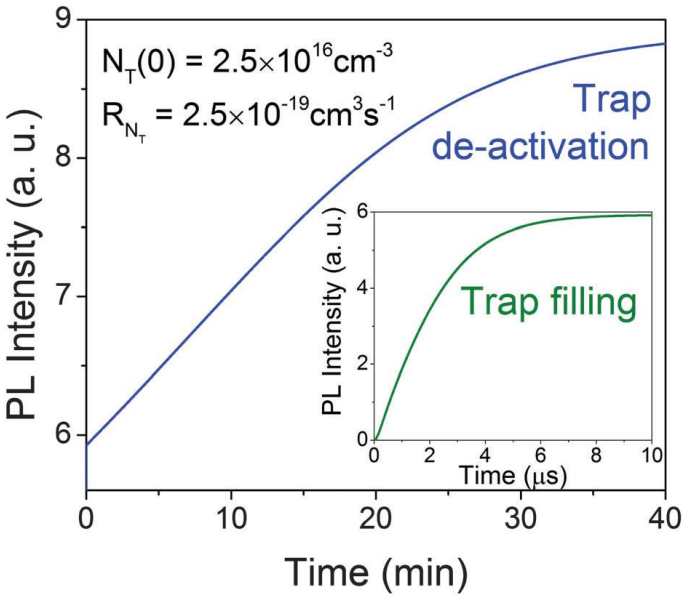

Figure 5.3 Modelled PL intensity enhancement using parameters from Table 5.1 with additional constant trap reduction rate R_{N_T}. The modelled PL increase can last for more than 40 min with de-activation rates in the range of $10^{-19}\, cm^3 s^{-1}$; the inset shows the initial rapid increase in PL during the first 10 µs of illumination due to trap filling.

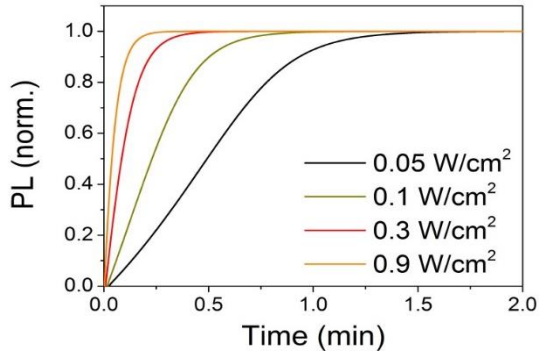

Figure 5.4 Modelled power-dependent PL increase as a function of time.

5.2.3 The reversibility of trap de-activation

The reversibility of the observed light-induced PL enhancement has already been discussed in several works. Ref. [42] and [117] concluded that the change can be, at least partially, recovered by placing the sample in the dark, although an apparent increase in PL has also been observed in some cases [42]. Ref. [41] and [42] also observed a reduction in the PL enhancement effect when isolating the films from oxygen. To investigate this further, a similar measurement was performed to that shown in Figure 5.1b, but the laser illumination was stopped at intervals during the initial exposure of the film. The detected PL emission right after 5min in the dark is always lower than that immediately before blocking the laser beam (Figure 5.5a). Figure 5.5b shows that the PL intensity will return to the original level if the pre-illuminated sample is stored in the dark for 30 min in an N_2 environment to protect it from degradation. This apparent reversibility of the enhanced PL suggests that either the surrounding active traps diffuse into the illuminated region, or the de-activated traps re-activate in the dark.

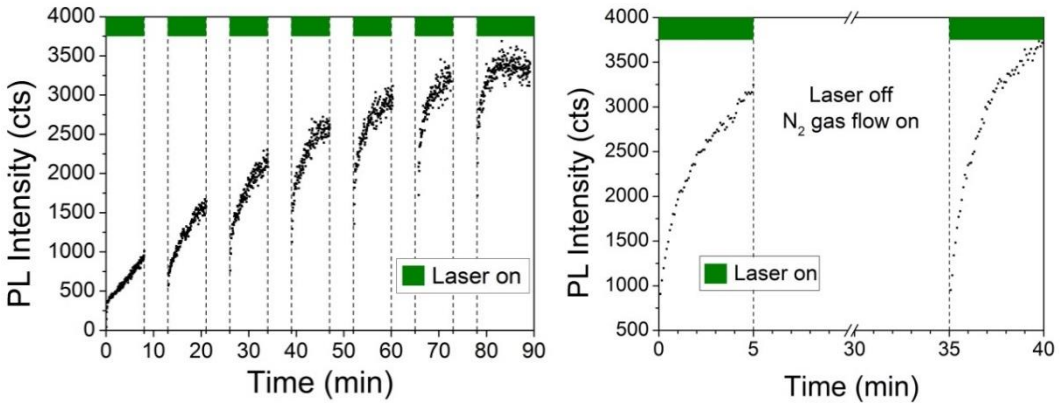

Figure 5.5 Single point PL intensity measurement with intervals of laser exposure. (a) The laser source is turned on for 8 min and then turned off for 5 min in each cycle. The overall PL intensity is enhanced over a period of 90 min, while the enhanced PL always reduces to some extent during the dark time. (b) The laser source is turned on for 5

min and then turned off for 30 min in each cycle. The PL intensity return to the origin level when the sample is stored in an N_2 environment.

The mobility of defects in $CH_3NH_3PbI_3$ has been frequently discussed in the literature [126, 127]. It has been suggested that ion vacancies and interstitial impurities can easily diffuse across perovskite crystals and along grain boundaries with activation energies less than 1 eV. Thus, trap diffusion could be potentially responsible for the reversibility. On the other hand, oxygen assisted trap de-activation has been suggested to represent an oxidation reaction of Pb^0 to form PbO in the bulk and/or passivation of traps on the surface [42]. Recent Raman-based studies have also shown that exposure of perovskite films to 532 nm laser light can effectively induce Pb-O inclusion into the $CH_3NH_3PbI_3$ framework [128]. In this scenario, the reversibility can be explained by Le Châtelier's principle [42], whereby traps are either de-activated or re-activated according to the relative abundance of oxygen and photocarriers in the light or the dark.

The following sections demonstrate the spatial characteristics of the PL enhancement both experimentally and numerically, and discuss that trap diffusion is not sufficient to explain the reduction in PL emission observed in Figure 5.5a when the illumination is turned off. Using a full two-dimensional numerical model that includes trap de-activation and re-activation in addition to carrier diffusion, it is shown that all of the experimentally-observed features can be accurately reproduced using physically-realistic parameter values.

5.2.4 Observation of lateral PL enhancement

The results in Figure 5.1 were measured at a single location using a fixed laser excitation spot and simultaneous PL detection, and thus only provide information about changes occurring in the directly-illuminated part of the film. Next, the spatial extent of the trap de-activation in the vicinity of the illuminated region is investigated by combining fixed-point illumination with rapid PL mapping over the surrounding area.

The measurement procedure is described below. First, a 50 μm × 50 μm area was scanned by a confocal microscope to produce a PL intensity image of the unexposed film (Figure 5.6a). Next, the near-diffraction limited laser spot was moved to the centre of this area and held there for 5 minutes, before repeating the area scan. In this way, a series of PL images were taken after every 5 minutes of laser exposure up to a total

exposure time of 20 minutes (Figure 5.6 b-e). An 100× objective lens was used for scanning in order to obtain high resolution, with a spot size of 930 nm. The green marker at the centre of the images indicates the size and position of the laser spot. The profile of the focussed laser beam and the measurement of laser spot size is shown in Figure 3.4b. The resolution of the images in Figure 5.6 is 200 pixel × 200 pixel; and the illumination time for each pixel is 1 ms. The time for PL imaging (~30 s) is much shorter than the 5 minutes continuous laser excitation in the centre; therefore light-induced changes during image scanning are negligible. This can be observed by the unchanged PL intensity at the edges of the scanned area.

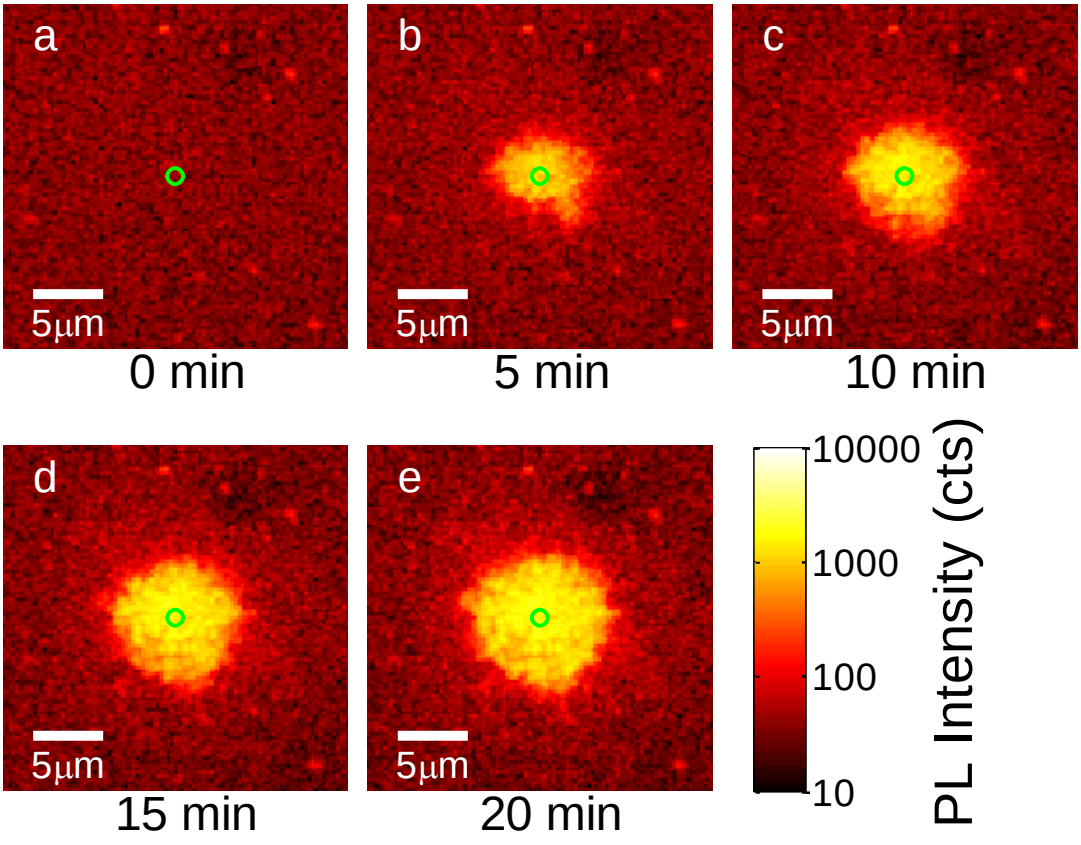

Figure 5.6 Spatial dependence of PL enhancement in a perovskite film due to laser exposure demonstrated by PL imaging. A tightly focussed laser spot was positioned in the centre of the image (green circle) for (a) 0 min, (b) 5 min, (c) 10 min, (d) 15 min and (e) 20 min, followed by a rapid scan of the PL emission. The diameter of laser spot is estimated to be 930 nm. The laser intensity is approximately 50 W cm^{-2}. The integration time of each pixel is 1 ms and there are 10 pixels per nanometre.

At the centre of this area, the PL intensity increases with exposure time as expected from the results in the previous section. Surprisingly, however, the region of PL enhancement extends far beyond the laser spot, with increased emission observed more than 5 μm from the centre after 20 minutes of exposure (Figure 5.6e). As discussed previously, it is believed that the PL enhancement is caused by the reaction

of three elements: photogenerated carriers, bulk traps and oxygen-related species. It can be assumed that a certain amount of oxygen gas has penetrated into the perovskite through the PMMA layer as the measurement was performed in air. Thus, the lateral spreading of the PL enhancement beyond the illuminated region may be a result of the outward diffusion of carriers (Figure 5.7a), the inwards diffusion of traps (Figure 5.7b), or a combination of both. Note that, the sample used in this experiment is planar perovskite film deposited on glass substrate, the surface roughness should be very small (Figure 3.1), and light scattering can be ignored in this case.

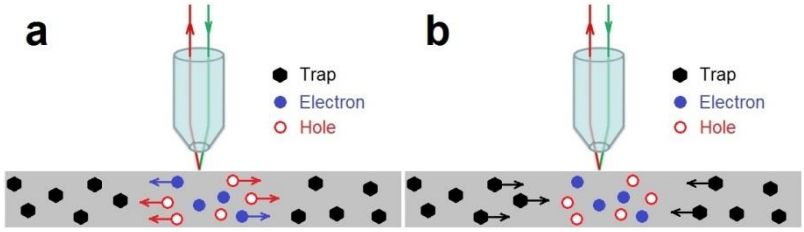

Figure 5.7 Schematic diagram of (a) carrier diffusion and (b) trap diffusion.

The carrier diffusion length of perovskites has been reported to vary from hundreds of nanometres to a few micrometres [62, 64, 67, 129-134], and is expected to increase locally as traps are de-activated in the presence of carriers and oxygen. Vertical carrier diffusion was proposed in ref. [42] as being responsible for an enlarged trap de-activation zone deeper inside the bulk of perovskite films during prolonged exposure. The same mechanism may allow photocarriers to diffuse laterally over the distances observed in Figure 5.6 during the trap de-activation process, as illustrated in Figure 5.7a. In addition, the possibility of trap diffusion has been identified in the previous section. Therefore, it is also possible that active traps may diffuse towards the centre of the exposed region, as the traps are de-activated close to the laser spot. This effect may further contribute to the lateral spread of the PL enhancement into unexposed areas (Figure 5.7b).

5.2.5 Investigating trap diffusion and trap re-activation

To investigate the possible contribution of trap diffusion to the lateral spread of PL enhancement, a modified version of the measurements is performed in Figure 5.5a. Instead of exposing a single point, a small area (20 μm × 20 μm) was continuously scanned for 5 min intervals to de-activate traps over a much larger area. The PL was mapped over a 50 μm × 50 μm area centred on the exposed region every 5 minutes

(Figure 5.8a). Note that the two bright spots in the left corners of the continuously scanned areas in Figure 5.8 a and b are the start point and end point of each scan, where the laser spot paused briefly. These two points received a longer exposure than the rest of the scanned area. Figure 5.8c shows the PL intensity of the cross-sections in Figure 5.8a, indicating that the PL increases dramatically in the exposed area, and extends several microns beyond. Exposure of the central area was stopped after 25 min, and the PL intensity is mapped continuously every 5 min (Figure 5.8b). During this period, the PL intensity of the entire scanned area decreased at the same rate (Figure 5.8d). Importantly, there is no evidence of the recovery starting from the edges and spreading inwards – the edges of the previously exposed area remain sharp and well-defined, indicating that either (a) the decrease in PL intensity is not due to active traps diffusing into the trap de-activated area; or (b) the diffusion of traps is negligible over length scales beyond a few micrometres and time scales of minutes.

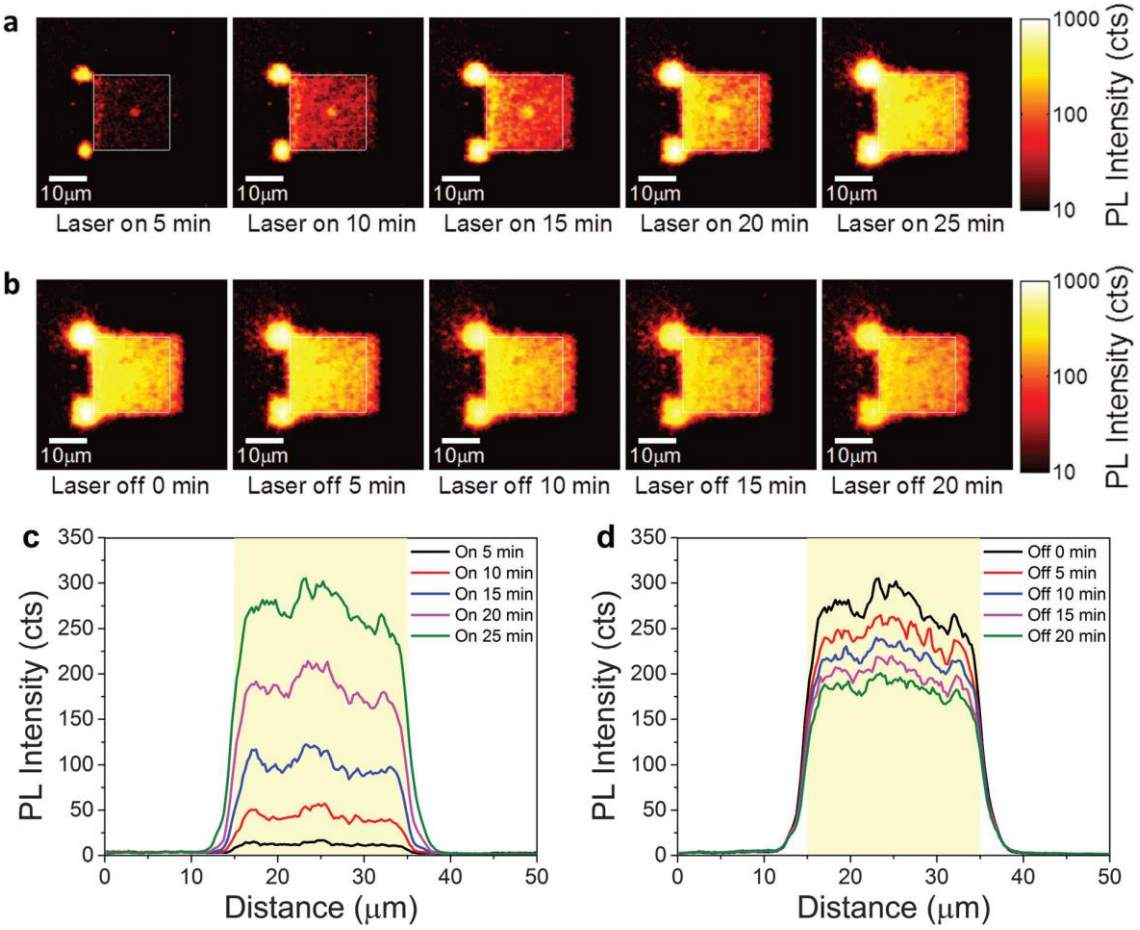

Figure 5.8 Small area de-activation and re-activating of traps: (a) 50 μm × 50 μm PL intensity images obtained after continuous scanning of a central 20 μm × 20 μm area for 5 min, 10 min, 15 min, 20 min and 25 min. (b) After a total expose time of 25 min the exposure was stopped and PL emission was imaged every 5 min for another 20 min. The white square indicates the illuminating region. Integrated cross-section for de-activation and re-activation are shown in (c) and (d) respectively. The light yellow region (15 μm to 35 μm) indicates the illuminated area. The laser

wavelength is 532 nm. The laser intensity is approximately 50 W cm^{-2}. The integration time of each pixel is 1 ms and there are 10 pixels per nanometre.

Therefore, it can be concluded that the lateral expansion of the PL enhanced region is dominated by photocarrier diffusion. Furthermore, these results strongly suggest that the reversibility of laser induced PL enhancement is dominated by the re-activation of de-activated traps after illumination is stopped, a result which is in agreement with ref. [42].

5.2.6 Modelling spatial-dependent PL enhancement

In this section, it is demonstrated that the key experimental observations presented above can be reproduced in a semiconductor model with realistic parameters. The model was designed to include the essential features of localised generation, 2-dimensional carrier diffusion, trap-assisted recombination, trap de-activation by photo-generated electrons, and trap re-activation. The resulting set of coupled non-linear partial differential equations was solved using the semiconductor module of COMSOL Multiphysics.

The semiconductor model developed for this study incorporated the 2-dimensional semiconductor drift-diffusion equations (although no electric field was present for the drift contribution) plus terms accounting for generation and recombination via traps, as well as radiative recombination. The semiconductor module of COMSOL Multiphysics was used to solve these equations for an input trap density profile which was determined by the competition between de-activation via free electrons and re-activation on a pre-set timescale:

$$\frac{\partial N_t}{\partial t} = -R_{deac} n_e N_t + \frac{N_{t0} - N_t}{\tau_{reac}}. \qquad 5.5$$

Starting from a trap distribution with uniform density N_{t0}, the semiconductor model was used to determine n_e, which was then used to update the trap distribution according to Equation 5.5 ready for input into the semiconductor module at the next time step. After generating a history of trap densities, a simulation of the PL imaging process is performed in a fully 2-dimensional model which accounted for the finite laser spot size and the focal width, both of which were found to be significant given the rapid spatial variation in recombination rates.

It is noted that in contrast with the 0-dimensional preparatory calculations of Figure 5.3, which assumed a constant carrier lifetime and permanent trap deactivation, this full model includes the possibility of both trap deactivation and re-activation, and a carrier lifetime which is directly related to a spatially varying trap density.

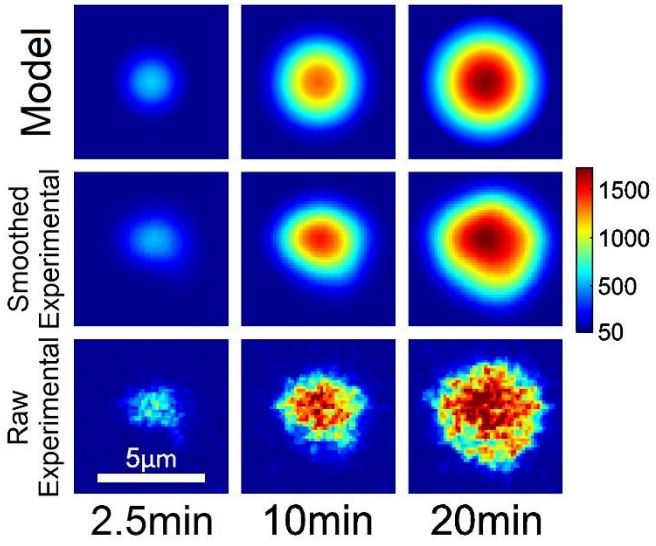

Figure 5.9 A full comparison between raw experimental PL intensity data (bottom row), spline-smoothed data (middle) and the modelled result (top) using the parameters in Table 5.2.

Figure 5.9 shows a comparison between the raw transient PL data, smoothed, and modelled data. Line plots of the averaged PL data at varying displacements from the central spot for both experimental and modelled results are also shown in Figure 5.10.

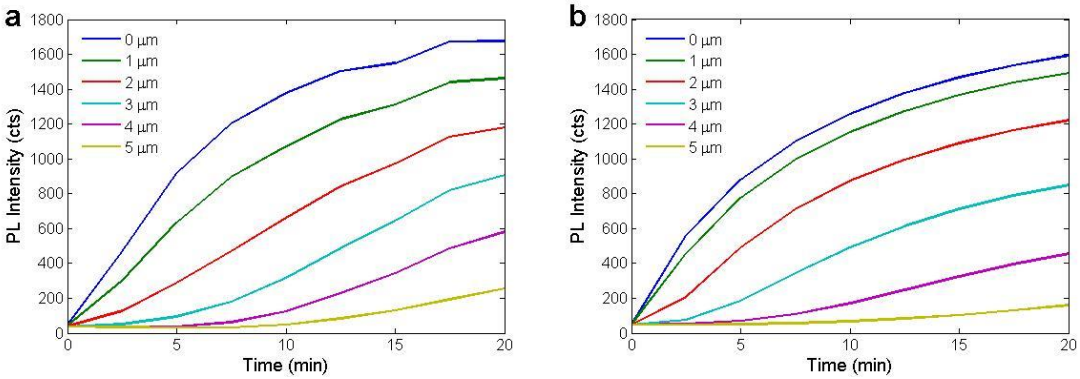

Figure 5.10 Line plots of the averaged PL data at varying displacements from the central spot for (a) experimental and (b) modelled results.

To obtain this agreement, an approximate fitting procedure was performed on parameters including the initial trap density, capture probabilities, and carrier mobilities (a summary of values is given in Table 5.2). The result successfully reproduces the most prominent features in the experimental data such as a total enhancement factor of ~50 for the central spot, the spread of enhanced PL efficiency

out to distances of 5 mm at long times and the distinctive S-shape of curves at larger radii (Figure 5.10). Most importantly, the model parameters all fall within known ranges for solution-deposited $CH_3NH_3PbI_3$, although it should be emphasised that there were too many unknowns in the fitting procedure for these to be used as reliable estimates. Instead, the above is considered as compelling quantitative evidence in favour of the theory that light- and oxygen-related trap de-activation is the source of PL enhancement in $CH_3NH_3PbI_3$ films.

Table 5.2 Parameters used in the semiconductor model.

N_{t0} (initial trap density)	2×10^{10} cm^{-3}
C_n, C_p (capture probabilities)	3×10^{-10} cm^{-3}s^{-1}
R_{deac} (rate of trap de-activation)	2×10^{-16} cm^{3}min^{-1}
τ_{reac} (fitted timescale of trap re-activation)	20 min
E_t (defect level)	0.7 E_g
μ_n, μ_p	4 cm^{3}V^{-1}s^{-1}
P_{soak}/P_{probe}	130Wcm^{-2}/80Wcm^{-2}
d_{soak}/d_{probe}	$2.1\mu m/0.7\mu m$
C (radiative coefficient)	1.7×10^{-10} s^{-1}cm^{-3}

As a bonus, this model can also reproduce the trend in Figure 5.5a, namely that the PL enhancement is accelerated after extended periods in the dark (Figure 5.11a). This can be understood by inspection of Figure 5.11b which shows that the most significant recovery after switching off the illumination occurs in the central region, whereas the de-activation "progress" further away is almost unaffected. After the recovery period a high photogenerated carrier density is able to rapidly de-activate the central region once more to resume the de-activation of defects at the expanding boundary.

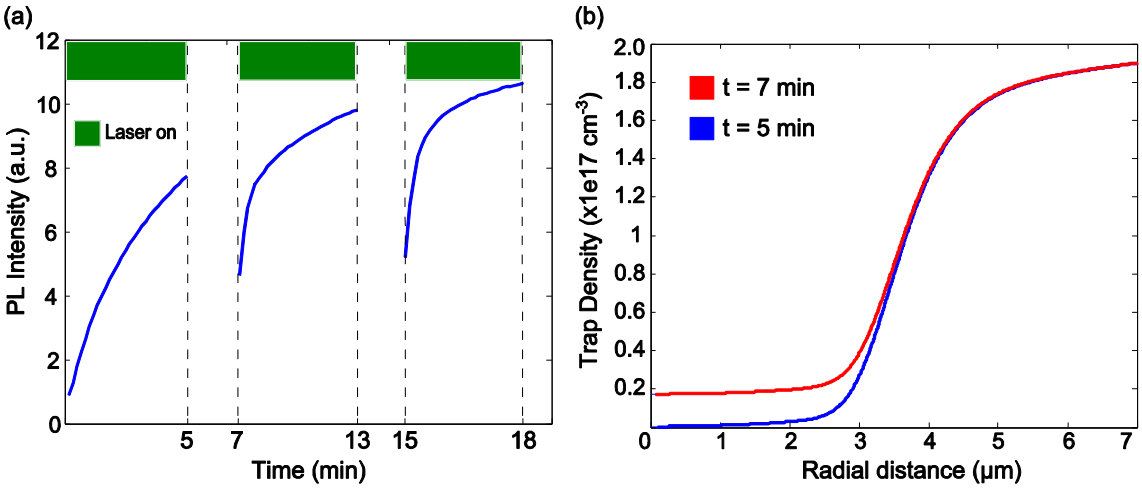

Figure 5.11 (a) Simulated PL intensity following periods when the illumination is switched off and traps are allowed to recover. (b) Trap densities immediately before and after the recovery period beginning at t=5min showing a rapid recovery in the central region where the density of de-activated traps is largest.

5.3 Conclusion

In summary, a combination of experimental photoluminescence measurements and numerical modelling have been used to investigate the dramatic enhancement in photoluminescence following prolonged light exposure with timescales ranging from minutes to hours. Expanding on previous work which attributed this phenomenon to trap de-activation in the presence of light and oxygen, it has been shown that the time and spatial dependence of the photoluminescence enhancement can be explained by a combination of trap de-activation and photogenerated carrier diffusion away from the light-exposed area. The trap de-activation process was directly observed by combining localised illumination with PL imaging, resulting in lateral carrier diffusion over several microns. Furthermore, it has been demonstrated that the trap de-activation is not a permanent change, and that de-activated traps re-activate once the illumination is turned off. The temporal and spatial dependence of laser induced PL enhancement was modelled in perovskite films, taking into account trap de-activation, carrier diffusion and trap re-activation and successfully reproduced the observed key features.

5.4 Published studies after this work

In the literature review of oxygen-related PL enhancement (2.3.2), the relevant studies after this publication have been discussed [43-46, 57]. First, the energy levels of the de-activated traps were investigated by Zhang and Meggiolaro. According to the limited penetration of O_2 into perovskite crystals, Zhang suggested that only surface traps are de-activated by oxygen [44]. However, the trap de-activation mechanism was considered as the formation of iodine oxides in Meggiolaro's study. By modelling the trap energy states of interstitial iodine based on hybrid density functional theory, a relatively deep trap energy level of 0.54 eV below the conduction band was obtained [45]. On the other hand, the type of oxygen species that de-activates traps was investigated by Feng *et al* [46]. They suggested that the penetrated O_2 would react with free carriers to generate superoxides O^{2-}, which could effectively passivate the traps in perovskites. Stoeckel proposed a potential application of this oxygen-related PL behaviour – perovskite oxygen sensor [57]. A perovskite device has been fabricated

to demonstrate the real-time change in current when placing the device in the atmosphere with different O_2 concentration (Figure 2.7).

Chapter 6 Characterisation of trap states in perovskite films

The contents of this chapter have been accepted as the following journal article: X. Fu, K. J. Weber and T. P. White, "Characterisation of trap states in perovskite films by simultaneous fitting of steady-state and transient photoluminescence measurements," Journal of Applied Physics.

6.1 Introduction

One of the defining characteristics of perovskite solar cells is their high open circuit voltage. The best mixed-cation, mixed-halide perovskite solar cells have achieved V_{OC} of 1.2 V with a bandgap of ~1.6 eV [135]. Such performance results from the excellent optoelectronic properties of solution-processed perovskite films, and in particular their high radiative efficiency. In two recent reviews, Tress [77] and Stranks [72] discussed the importance of radiative efficiency for cell performance, and identified further reductions in non-radiative recombination as the key to boosting cell efficiency toward theoretical limits.

Under normal operating conditions, non-radiative recombination in perovskite solar cells is dominated by trap-assisted recombination, referred to Chapter 2. The physical and chemical origin of such traps (or defects) in perovskite materials is an ongoing research topic, but intrinsic defects such as lattice vacancies and interstitial ionic species have been identified as likely contributors. Experimental characterisation of the recombination dynamics and trap properties is an essential step toward identifying and eventually mitigating specific trap states, and requires accurate and reliable methods for comparing different samples and material compositions.

The three main physical parameters that determine how a particular trap state will impact the non-radiative recombination rate are the trap density (N_t), energy level (E_t) and capture cross-sections for electrons and holes (σ_n and σ_p respectively) [77]. Measuring these parameters directly is challenging and few techniques allow all parameters to be extracted simultaneously. Electrical characterisation methods for measuring trap density and energy level include thermally stimulated current and

capacitance vs. frequency measurements at different temperatures [74-76, 136]. However, both techniques require electrical contacts on the sample which can introduce additional recombination, while the application of an electrical bias can also induce ion migration. Temperature-dependent measurements also present challenges for perovskites due to the possibility of phase transitions and/or thermal degradation.

Steady-state and transient photoluminescence measurements are widely used for studying carrier recombination in perovskite films and solar cells as they are fast, non-contact, and can be applied to films, partial devices and complete cells. Both types of measurements are commonly used to compare the relative quality of samples, where high PL intensity and/or long lifetimes are typically associated with improved cell performance. Alternatively, more detailed quantitative data can be extracted by fitting the experimental measurements to a theoretical recombination model. Ideally, such a model should not only provide a good fit to the experimental data, but should also allow relevant physical parameters to be extracted.

The most common recombination models used to fit transient measurements are based on the simple rate equation $\frac{dn}{dt} = G - k_1 n - k_2 n^2 - k_3 n^3$, where n is the electron density, G is the charge-carrier generation rate; k_1 is the trap-assisted recombination rate; k_2 is the radiative recombination rate; and k_3 is the Auger recombination rate [81, 82]. A major limitation of this approach is that the trap-assisted recombination is described by a single rate constant k_2, which does not directly relate to the relevant physical trap parameters (density, energy level, cross-section) identified above. Furthermore, the rate equation is strictly only valid when the electron density (n) and hole density (p) are equal, and when the concentration of generated carriers is much higher than the intrinsic carrier concentration (n_i). Only under these conditions is the radiative recombination rate proportional to n^2; more generally it scales as $(np - n_i^2)$.

The simple rate equation given above was extended by Stranks and Manger [72, 73] to include separate terms for capture and emission of free carriers, as well as dependence on trap density and capture cross-section (Section 2.5.2). These works provided new insights into carrier recombination dynamics, but the trap energy level was still not explicitly included in the model.

A complete physical model of SRH recombination including all three physical trap parameters was used by Wen *et al* [87] to fit steady-state PL measurements as a function of excitation level. However, as discussed below, steady-state PL measurements depend only weakly on trap energy level and capture cross-section, and thus the accuracy with which these parameters can be estimated with this approach is relatively low.

To overcome the limitations of the above methods, here a single, general transient recombination model is applied to fit simultaneously both steady-state and transient PL measurements as a function of excitation intensity. With this approach, it is possible to extract recombination coefficients, trap density, trap energy level, capture cross-section, and doping density, and to estimate the accuracy of the fitted parameters using a sensitivity analysis. The technique is demonstrated on both $CH_3NH_3PbI_3$ and high-performance quadruple-cation $Cs_{0.07}Rb_{0.03}(FA_{0.85}MA_{0.15})_{0.9}Pb(I_{0.85}Br_{0.15})_3$ perovskite films, providing a direct comparison of differences in trap properties in these two perovskite compositions. Interestingly, the most notable difference between the two film compositions is seen in the hole capture cross-section, which differ by two orders of magnitude. While further study is required to verify these observations, the results may provide new insights into the origin of the improved performance of mixed-cation/mixed-halide perovskites. These results demonstrate the utility of photoluminescence analysis for quantitatively studying trap states in perovskite films.

6.2 Theory

The detailed theory of recombination kinetics in non-degenerate semiconductors has been described in Section 3.3.2. Here, the dynamics of carriers and traps during transient and steady-state PL measurements are modelled based on Equations 3.16-3.34. For the required constants in the model, the semiconductor bandgap E_g was extracted from measured PL spectra (Figure 6.1). The effective density of states N_C and N_V of the perovskite materials are calculated according to the reported effective masses of electrons and holes (m_e^* and m_h^*) [137]. The absorption coefficients of $MAPbI_3$ and quadruple-cation perovskite films were taken from published values to be $1.5 \times 10^4\ cm^{-1}$ [105] and $1.2 \times 10^5\ cm^{-1}$ [138] respectively at a wavelength of approximately 500 nm for the purpose of calculating generation rates within the films.

Furthermore, following the approach of Stranks, Manger and Wen [72, 73, 87], it is assumed that the recombination is dominated by a single type of trap, although the presence of multiple traps has been reported [75, 76, 139].

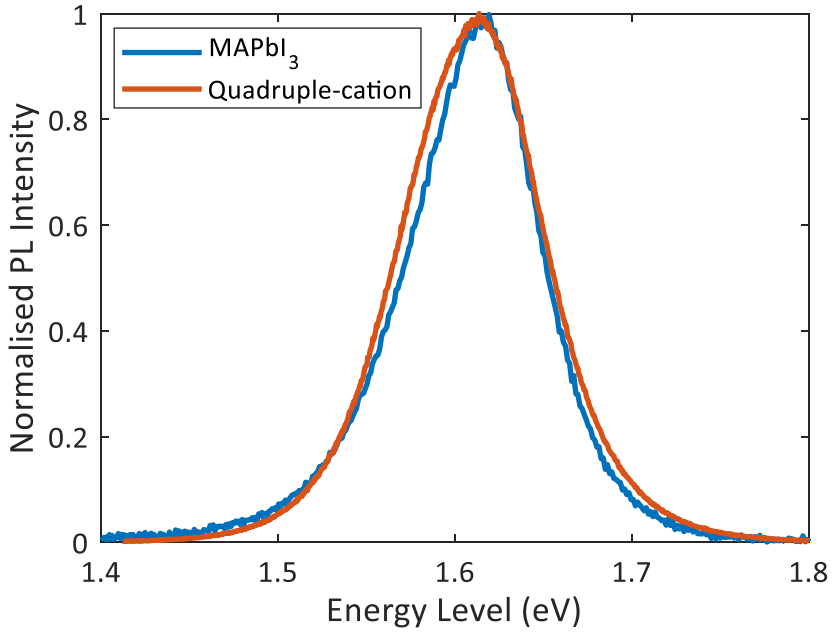

Figure 6.1 Normalised PL spectra extracted from $MAPbI_3$ film (red curve) and quadruple-cation film (blue curve).

This is sufficient to obtain very good fits to the experimental parameters, suggesting either that the assumption of a single trap state is valid, or that the extracted trap parameters correspond to 'effective' values with contributions from several different trap states. It is not possible to separate these two possibilities with the available data.

6.3 Numerical implementation

The recombination expressions summarised in Section 3.3.2 were implemented in a time-domain numerical model that could be used to simulate both steady-state and transient experimental conditions. To reproduce a steady-state PL intensity measurement in the model, a constant generation term was set at time $t = 0$, and the time-dependent recombination rates (Equations 3.26 and 3.27) were calculated until they reached equilibrium where the SRH recombination rates of electrons and holes were equal (Figure 6.2a). Intensity-dependent PL intensity curves were produced by repeating this calculation as a function of generation rate. Examples of such curves are shown in Figure 6.4 a, c and e, calculated for representative parameter values. When fitting the model to the experimental data, it was necessary to scale the modelled data

by a constant value as the experimental measurements were uncalibrated and included optical collection losses. Experimental generation rates were calculated from the laser wavelength, laser intensity and the absorption coefficient. The detailed experiment settings are described in the Section 3.2.2.

To simulate a transient PL measurement, the ~110 ps excitation laser pulse was approximated by a square generation profile and the transient radiative recombination rates were calculated following the pulse. The results of such a simulation are shown in Figure 6.2b. The normalised decay curve on the right-hand side of Figure 6.2b is equivalent to the measured PL decay. The excited carrier density was calculated from the laser wavelength, laser intensity, laser pulse width, and the absorption coefficient (See Section 3.2.2 for experiment details).

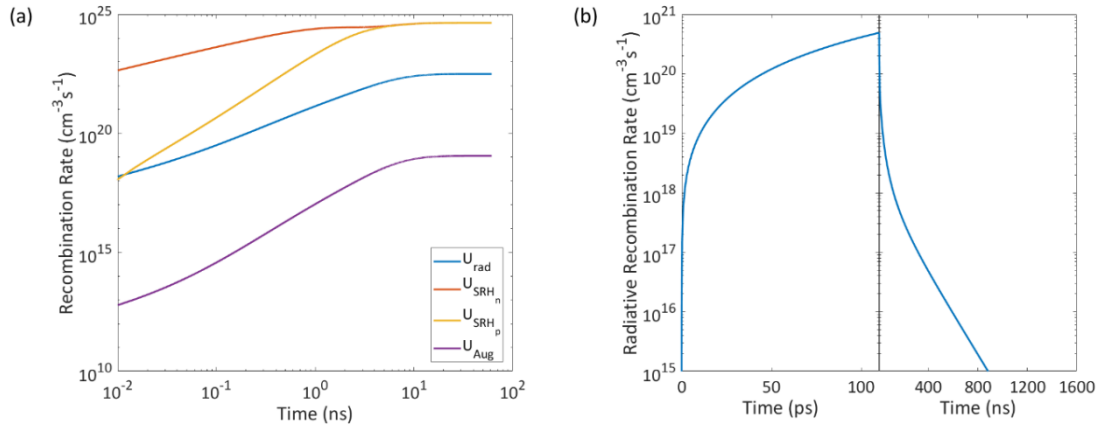

Figure 6.2 (a) Modelled recombination rates as a function of time after turning on a constant illumination at t = 0 until steady-state condition is reached; (b) Modelled radiative recombination rate as a function of time during one period of laser pulse (110 ps pulse width and 1600 ns repetition rate) in the transient PL measurement. Note that the time scales on the left hand side and right hand side of (b) are different.

It is common practice to normalise transient PL curves to the initial (t ≈ 0) data point in order to compare multiple measurements. However, this approach can be sensitive to the very rapid dynamics that occur during and within the first few ns following the excitation pulse. This is illustrated in Figure 6.3a using a simulated example. Normalising the PL decay curves with different starting points (Point 1, 2 and 3 in Figure 6.3a; which are separated by only 200 ps) leads to a vertical shift in the normalised results (Figure 6.3b). While this may not be significant when comparing relative decay rates between samples, it is a potential source of error when attempting to fit a numerical model to multiple decay curves measured under different conditions, as in this work. Thus, to minimise the uncertainty caused by normalisation, here both

the experimental and modelled transient PL curves are normalised at a later time of t = 50 ns where the decay curves are less steep, and there is no possibility of contribution from the excitation pulse.

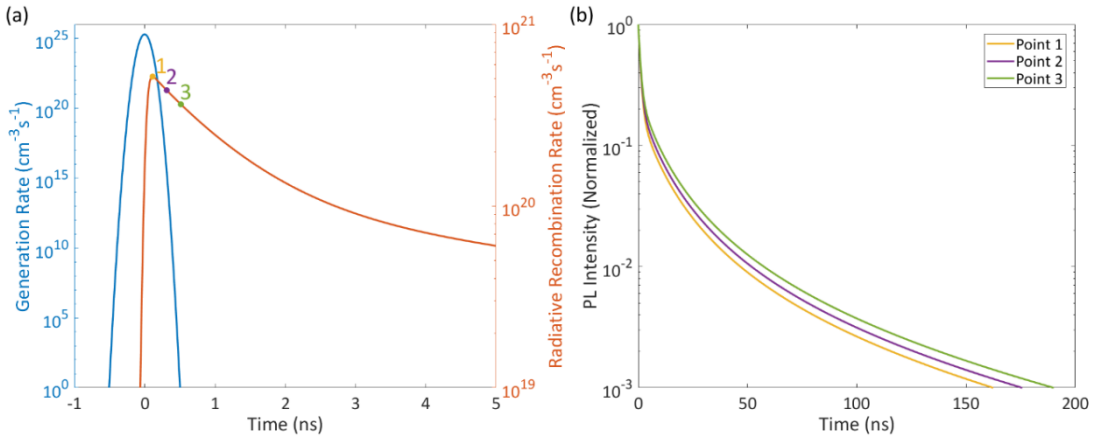

Figure 6.3 (a) Simulated generation rate and transient radiative recombination rate during pulsed excitation. (b) The transient radiative recombination rate normalised at different initial data points 1, 2, 3 shown in (a), where these points are separated by 200 ps.

Before attempting to fit the recombination model to the experimental data, the sensitivity of the steady-state and transient PL measurements to the trap parameters of interest is investigated using published parameter values as inputs to the model. For this part only $CH_3NH_3PbI_3$ is considered, as published experimental data on trap properties in multi-cation perovskite compositions is limited.

Table 6.1 Parameters of $CH_3NH_3PbI_3$ from literatures

Parameters	***Values***	
$B\ (cm^3s^{-1})$	1.3×10^{-10} [72], 5.9×10^{-13} [73]	
$N_t\ (cm^{-3})$	2.5×10^{16} [72], 7.44×10^{16} [87], 1.04×10^{17} [87]	
$E_t\ (eV)$	$E_c - E_t$ 0.62, 0.75, 0.76 [75], 0.24, 0.66 [76]	$E_t - E_v$ 0.129, 0.024, 0.16, 0.459, 0.508 [139]
$\langle c_n \rangle\ (cm^3s^{-1})$	2×10^{-10} [72], 9.1×10^{-13} [73]	
$\langle e_n \rangle\ (cm^3s^{-1})$	8×10^{-12} [72], 3.42×10^{-12} [73]	
$\Gamma\ (cm^6s^{-1})$	1.08×10^{-31} [73]	
$Doping\ Density\ (cm^{-3})$	$N_A = 4.0 \times 10^{16}$ [140], $N_D = 2.8 \times 10^{17}$ [140]	

Table 6.1 summarises the key material parameters of $CH_3NH_3PbI_3$ perovskite films from several different publications [72, 73, 75, 76, 87, 139, 140]. Significant variations (> two orders of magnitude) are noted in the published values of radiative coefficient (B), trap density (N_t), and electron capture coefficient ($\langle c_n \rangle$). Many different values have also been reported for trap energy levels (E_t), including both shallow hole and shallow electron traps, and deep (mid-gap) traps. This wide variation may indicate either wide sample-to-sample variation, or large experimental uncertainty (or both). The trap energy levels may also be influenced by whether the perovskite film is p-type or n-type, which has been found to vary depending on fabrication processes [140].

Table 6.2 Input parameters for the numerical implementation.

Parameter	***Values***
$B\ (cm^3 s^{-1})$	1×10^{-10}
$N_t\ (cm^{-3})$	1×10^{16}
$E_t\ (eV)$	0.20
$\langle c_n \rangle\ (cm^3 s^{-1})$	1×10^{-8}
$\langle e_n \rangle\ (cm^3 s^{-1})$	5×10^{-9}
$\Gamma\ (cm^6 s^{-1})$	1×10^{-31}
$N_A\ (cm^{-3})$	3×10^{14}

Using as input parameters representative values from Table 6.2, Figure 6.4 shows simulated PL intensity vs. excitation power curves (Figure 6.4 a, c and e) and simulated transient PL curves (Figure 6.4 b, d and f) for varying trap density (Figure 6.4 a and b), trap energy level (Figure 6.4 c and d) and electron capture coefficient (Figure 6.4 e and f). The range of generation rates in the excitation-dependent steady-state PL simulation and the excitation level used in the transient PL simulation (~ $1 \times 10^{24}\ cm^{-3} s^{-1}$) were chosen to approximate the experimental conditions. Note that the decision to normalise the transient PL curves at a time of 50 ns results in apparent trends that may appear different to the standard approach of normalising to the initial intensity. This does not affect the following parameter fitting procedure since the experimental and simulated curves are normalised in the same way.

As expected, Figure 6.4a shows that both the shape and magnitude of the steady-state PL intensity curves (radiative recombination rate) are relatively sensitive to changes in the trap density under the simulated conditions. The corresponding transient PL curves in Figure 6.4b also exhibit a dependence on these parameters, but this dependence

weakens at higher trap densities. This suggests that intensity-dependent steady-state PL measurements may be more accurate for extracting trap density when the density is high. In contrast, the steady-state PL curves plotted in Figure 6.4c show only a very weak dependence on trap energy level, whereas the transient PL curves have a much stronger dependence. This may be a consequence of the relatively high generation rates simulated for the steady-state case: when the density of photogenerated carriers is much higher than the trap density, the trap occupation rate becomes saturated. The stronger dependence in Figure 6.4d results from different rates of electron capture and emission at low excitation level, which are sensitive to trap energy level. Figure 6.4 e and f exhibit behaviour between the previous two cases: the steady-state PL curves are relatively sensitive to the electron capture coefficient at low generation rates, but converge as the generation rate is increased. The transient PL curves in Figure 6.4f show a transition from a single exponential (radiative recombination-dominated) decay when the capture coefficient is smaller than the emission coefficient (blue curve), to a non-exponential decay at higher capture coefficient values.

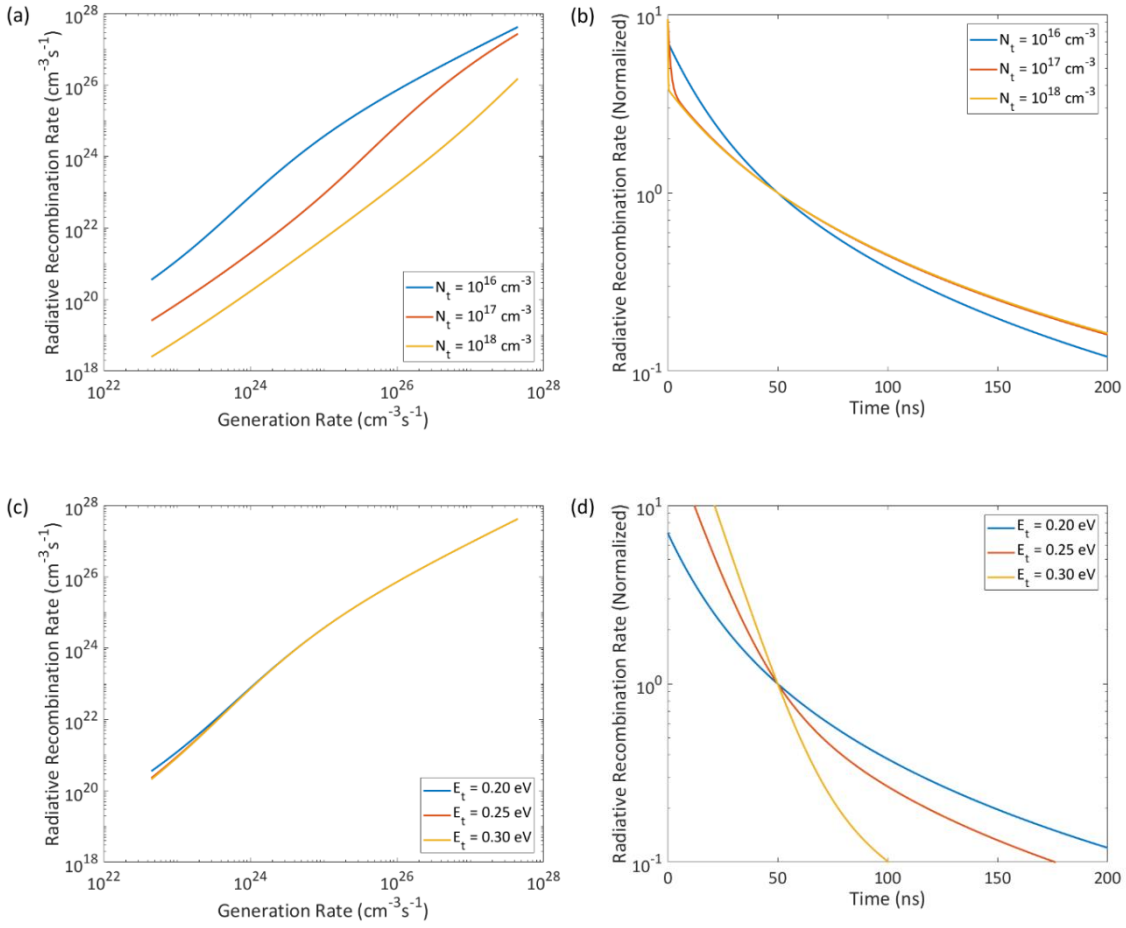

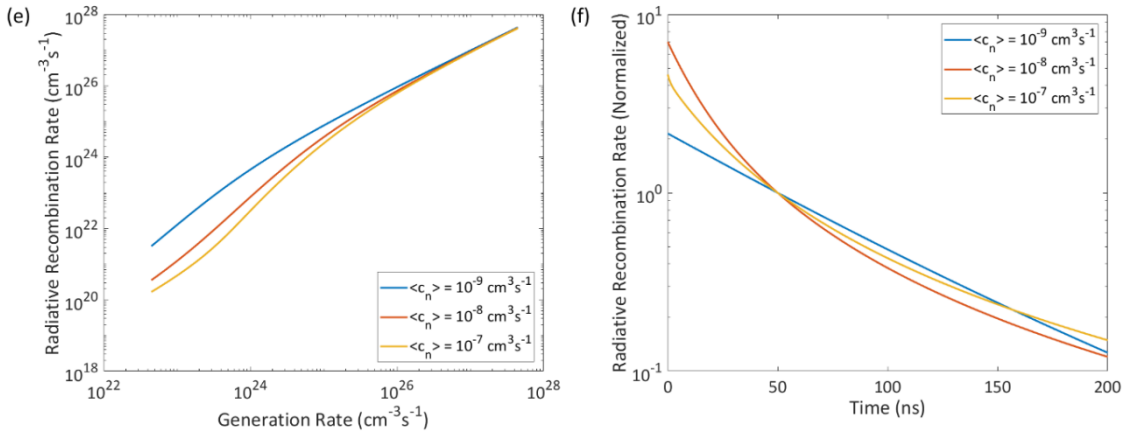

Figure 6.4 The simulated excitation-dependent steady-state PL measurement with different (a) trap density N_t, (c) trap energy level E_t, and (e) capture coefficient of electron $\langle c_n \rangle$; the simulated excitation-dependent transient PL measurement with different (b) trap density N_t, (d) trap energy level E_t, and (f) capture coefficient of electron $\langle c_n \rangle$.The input values are listed in Table 6.2.

The results in Figure 6.4 show that at least in some cases, transient PL measurements are relatively insensitive to N_t (Figure 6.4b), while excitation-dependent PL intensity shows little dependence on E_t (Figure 6.4c) within the experimental conditions simulated. Thus, attempting to extract values of trap properties using only one of these PL measurement techniques would result in large uncertainties. However, fitting a single recombination model to both sets of experiment data simultaneously, can significantly improve the accuracy of the fitted trap parameters, as shown below. In addition, the accuracy of the parameter extraction is further improved by including in the fitting routine three sets of transient PL spectra for each sample, measured at different excitation levels.

6.4 Experimental results

Two perovskite compositions were used in this experiment: the widely-studied $MAPbI_3$ and the more recently developed quadruple-cation/mixed halide perovskite $Cs_{0.07}Rb_{0.03}(FA_{0.85}MA_{0.15})_{0.9}Pb(I_{0.85}Br_{0.15})_3$. Both compositions were deposited as planar films on glass substrate as described in Section 3.1.2 and 3.1.3. Both films were coated with PMMA to protect them from moisture, and to passivate surface defects [96, 141]. The measurements were performed in a nitrogen environment.

Steady-state and transient PL measurements were carried out in a confocal microscope during a single measurement session. Further details of the experimental set-up and laser sources are provided in the Section 3.2.2. Steady-state PL spectra were collected first by varying the laser intensity over several orders of magnitude,

corresponding to generation rates from 10^{23} - 10^{28} $cm^{-3}s^{-1}$ (the calculation of generation rate is shown in Section 3.3.2). This range of generation rates spans operating regions previously identified as being dominated by monomolecular and bimolecular recombination [78, 79], and at the highest intensities starts to enter the Auger recombination regime. The PL peak intensities are plotted in Figure 6.5 a and c as a function of generation rate. Next, time-resolved PL spectra were measured at the same location on the sample under three different excitation levels (Figure 6.5 b and d).

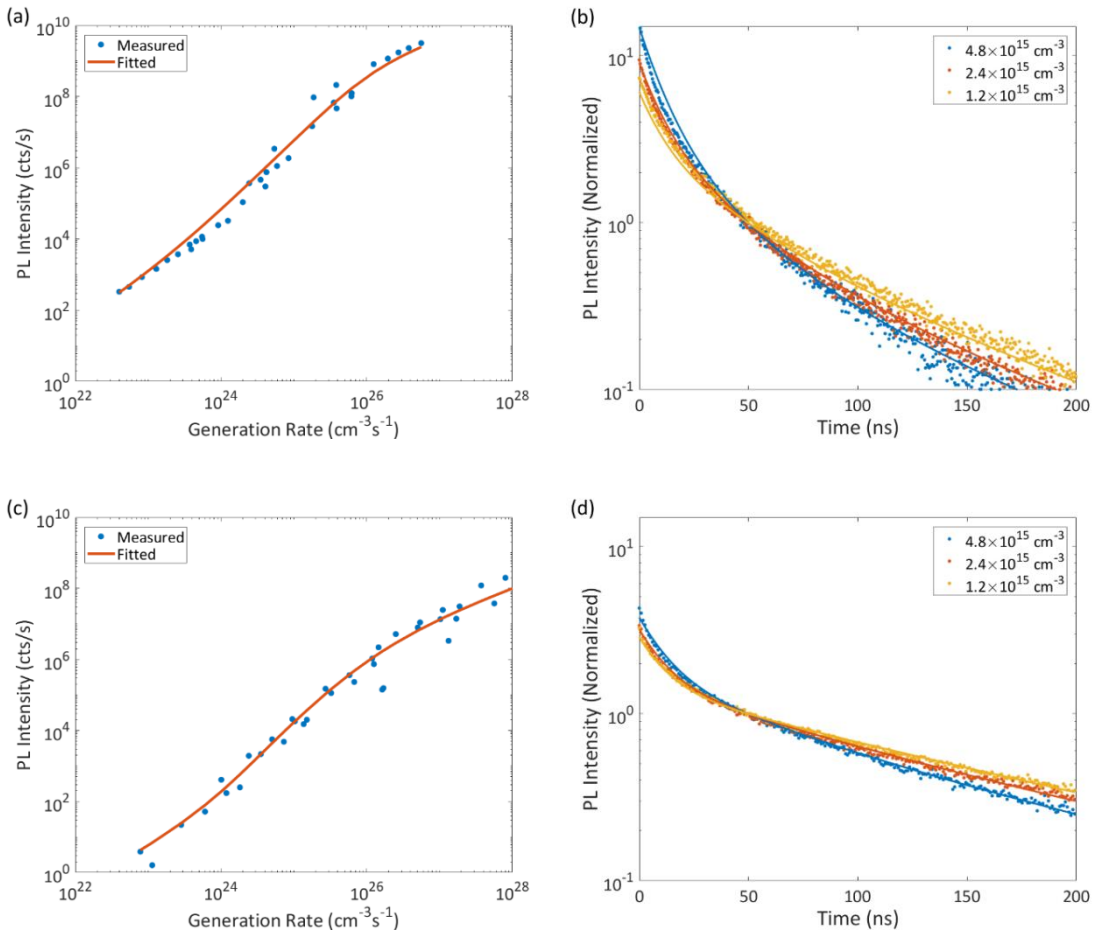

Figure 6.5 Measured (blue dots) and modelled (red line) steady-state PL peak intensity as a function of carrier generation rate on (a) $MAPbI_3$ perovskite film and (c) quadruple-cation perovskite film (Laser wavelength is 532 nm). Measured (dots) and modelled (lines) Transient PL with different excitation levels on (b) $MAPbI_3$ perovskite film and (d) quadruple-cation perovskite film (508 nm pulsed laser, 625 kHz repetition rate).

To confirm the sample stability during the experiment, films were exposed to the maximum laser intensity used in the steady-state PL measurements for 10 minutes and the PL emission was monitored. Samples were tested in two locations: first on an area of the sample that had already been measured, and also on a fresh (non-exposed) area. No significant change in the PL intensity was observed in either case (Figure 4.11).

In the recombination model, seven parameters (B, N_t, E_t, $\langle c_n \rangle$, $\langle e_n \rangle$, Γ, N_A) are unknown. Here, an electron trapping nature is assumed as in ref. [72] for p-type perovskite materials, corresponding to a trap energy level between the mid-gap and the conduction band. It is also assumed that the Auger coefficients are equal ($\Gamma_n = \Gamma_p = \Gamma$) to simplify the fitting, as has also been assumed in previous works [73].

The recombination model was fitted simultaneously to the four sets of experimental data (one set of steady state PL vs excitation level data and three sets of transient PL data):

For excitation-dependent PL peak intensity,

$$NRMSE_{PL} = \frac{\sqrt{\frac{1}{n}\sum_{i=1}^{n}\left(log_{10}(PL_{model}) - log_{10}(PL_{exp})\right)^2}}{\left|\frac{1}{n}\sum_{i=1}^{n} log_{10}(PL_{exp})\right|}. \quad 6.1$$

For time-resolved PL decay at each of the excitation level,

$$NRMSE_{Decay} = \frac{\sqrt{\frac{1}{n}\sum_{i=1}^{n}\left(log_{10}(Decay_{model}) - log_{10}(Decay_{exp})\right)^2}}{\left|\frac{1}{n}\sum_{i=1}^{n} log_{10}(Decay_{exp})\right|}. \quad 6.2$$

Then, the combined $NRMSE$ is calculated by taking the average of $NRMSE_{PL}$ and the average of three $NRMSE_{Decay}$ values for each sample.

$$NRMSE = NRMSE_{PL} + \frac{1}{n}\sum_{i=1}^{n} NRMSE_{Decay} \quad 6.3$$

Therefore, a single, combined value of normalised root mean square error ($NRMSE$) was defined, and minimised using a nonlinear optimisation routine. To improve the accuracy of the fitting, the logarithm of the data was taken since the measured PL intensities in both experiments are varied by several orders of magnitude. The process was repeated several times with different starting conditions to ensure that a stable, global minimum had been found. The fitted numerical results are plotted in Figure 6.5 as solid curves; and the fitted parameters are listed in Table 6.3.

Table 6.3 Fitted results and uncertainty bounds of each parameter.

Fitted Parameters	$CH_3NH_3PbI_3$			$Cs_{0.07}Rb_{0.03}FA_{0.765}MA_{0.135}PbI_{2.55}Br_{0.45}$		
	Fitted value	Lower bound	Upper bound	Fitted value	Lower bound	Upper bound
$B\ (cm^3s^{-1})$	7×10^{-12}	N/A	7.8×10^{-11}	3×10^{-12}	N/A	3.0×10^{-11}
$N_t\ (cm^{-3})$	1×10^{16}	8.6×10^{15}	2.3×10^{16}	8×10^{16}	6.4×10^{16}	1.1×10^{17}
$E_t\ (eV)$	0.20	0.188	0.202	0.17	0.161	0.172
$\langle c_n \rangle\ (cm^3s^{-1})$	8×10^{-9}	6.6×10^{-9}	1.1×10^{-8}	1×10^{-9}	8.7×10^{-10}	1.2×10^{-9}
$\langle e_n \rangle\ (cm^3s^{-1})$	4×10^{-8}	3.8×10^{-8}	4.5×10^{-8}	4×10^{-10}	3.4×10^{-10}	3.9×10^{-10}
$\Gamma\ (cm^6s^{-1})$	1×10^{-30}	N/A	3.6×10^{-29}	8×10^{-32}	N/A	8.0×10^{-31}
$N_A\ (cm^{-3})$	3×10^{14}	2.5×10^{14}	3.3×10^{14}	2×10^{16}	1.7×10^{16}	1.9×10^{16}

When comparing the experimental data to the numerical model, there are two distinct sources of error that contribute to the $NRMSE$. The first is noise in the raw experimental data that can be seen clearly in Figure 6.5. The second source of error is related to how accurately the numerical model describes the recombination kinetics. In the discussion below these are referred to as the *experimental error* and *fitting error* respectively. The presence of experimental error means that even if the model captures all of the relevant physical processes, the total $NRMSE$ will remain non-zero. Thus, it is desirable to separate the two error contributions. To approximate this, firstly a smoothed set of experimental data is generated by applying a moving average function. The experimental uncertainty is then defined as the $NRMSE$ between the smoothed moving average curve and the raw (noisy) data; while the fitting error is defined as the $NRMSE$ between the model and the smoothed experimental data. With this definition experimental $NRMSE$ values of 0.1 for both the $MAPbI_3$ and quadruple-cation perovskite films are calculated. Using this estimated experimental error as an upper error limit, the uncertainty of individual fitted parameters is defined as the range of parameter values within which the fitted $NRMSE$ remains smaller than the experimental $NRMSE$. Although this is a somewhat arbitrary choice, it provides a consistent definition for assigning an uncertainty to the fitted parameters. These uncertainties are expressed as upper and lower bounds on each parameter in Table 6.3.

As can be seen in Table 6.3, the above approach for defining uncertainties results in undefined lower bounds on the radiative recombination coefficient B and Auger recombination coefficient Γ. To investigate this further, the sensitivities of the fitted

parameters to the two different types of experimental measurements: excitation-dependent steady-state PL and transient PL are considered.

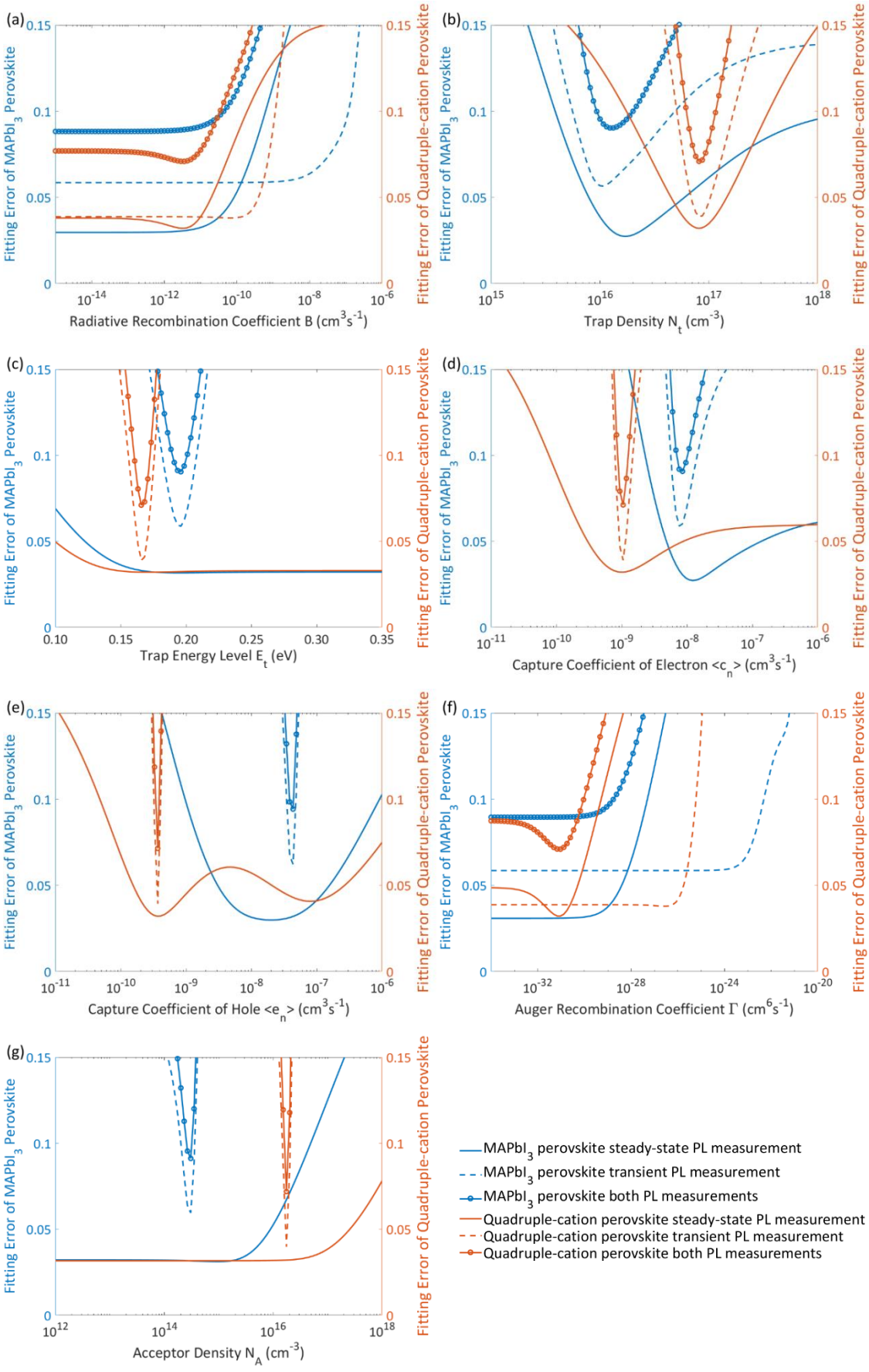

Figure 6.6 The fitting error (NRMSE) of steady-state PL measurements (solid lines), transient PL measurements (dash lines) and combined experiments (solid line with marker) on $MAPbI_3$ perovskite film (blue curves) and quadruple-cation perovskite film (red curves) when sweeping (a) radiative recombination coefficient B, (b) trap density N_t, (c) trap energy level E_t, (d) capture coefficient of electron $\langle c_n \rangle$, (e) capture coefficient of hole $\langle e_n \rangle$, (f) Auger recombination coefficient Γ, and (g) acceptor density N_A.

The blue curves in each sub figure of Figure 6.6 show the individual fitted NRMSE contributions associated with the steady-state PL data (solid curves), the transient PL data (dashed curves), and the total (combined) NRMSE contributions (solid curve with circles), for the $MAPbI_3$ sample as a function of a specific fitting parameter. The equivalent data is also shown for the quadruple-cation perovskite sample (red curves). Consider first the blue curves in Figure 6.6a. In this case, the quality of the fit to both types of PL measurements is seen to be insensitive to the value of the radiative recombination coefficient B except in cases of very large values of B. Thus, it is only possible to identify an upper bound for the value of B, but no lower bound. A similar situation is seen in Figure 6.6f for the Auger recombination coefficient Γ.

The remaining plots in Figure 6.6 demonstrate that the fitted parameters are generally more sensitive to one type of experimental measurement than another, illustrated by a narrow, well-defined minimum. This observation further justifies the value of using both steady-state PL and transient PL data to fit the recombination model. This is particularly obvious in the case of the electron and hole capture coefficients (Figure 6.6 d and e), where the transient PL data shows a much higher sensitivity to these parameters than does the steady-state data. This is also the case for the trap energy level (Figure 6.6c). Note also that there is a local minimum in the NRMSE when sweeping $\langle e_n \rangle$ which illustrates the importance of finding the global minimum during the fitting procedure (Figure 6.6e). This analysis demonstrates that it is indeed possible to extract constrained parameter values for all of the key trap parameters by fitting a single general recombination model to both steady-state and transient PL measurements.

The parameter values extracted for $MAPbI_3$ are generally consistent with those from the literature in Table 6.1. The value of E_t indicates the existence of relatively shallow traps close to the conduction band level. The extracted capture coefficients of electrons and holes are much larger than the reported values. The differences of these parameters between the two measured films are also obvious. Given the wide range of

material parameters typically reported for perovskite materials, it is not particularly surprising that the reported capture coefficients of perovskite films from only two papers differ from the extracted values in this work.

6.5 Discussion

Having extracted the trap parameters, and estimated the uncertainties, now a comparison of the two perovskite compositions can be made. As reported by a number of groups, quadruple-cation perovskite solar cells can achieve higher open-circuit voltage than $MAPbI_3$-based cells. The open-circuit voltage of a solar cell depends strongly on the relative rates of radiative and non-radiative recombination in the active layer. In order to maximise the V_{OC}, the non-radiative recombination – SRH recombination and Auger recombination should be minimised. Under standard one-sun illumination recombination in perovskite films is dominated by SRH recombination. Therefore, N_t, E_t, $\langle c_n \rangle$ and $\langle e_n \rangle$ are the most important parameters for determining recombination properties.

Considering the fitted results of these four parameters in Table 6.3, the trap densities of the two samples are similar; but the trap energy level of $MAPbI_3$ film is deeper than that of the quadruple-cation perovskite film which means that the fraction of traps working as recombination centres is higher in the $MAPbI_3$ film. The most significant difference between the two samples is in the capture coefficient of holes. The extracted capture cross-section of the quadruple-cation perovskite is up to two orders of magnitude smaller than that of the $MAPbI_3$ film. Theoretically, the capture cross-section of traps is related to the static dielectric constant of the material. The larger the dielectric constant, the smaller is the capture cross-section. By applying a Coulomb model, it suggests that the radius of the Coulomb well around a charged trap will be reduced when the dielectric constant is high [77]. As a result, it is more difficult for the charged carriers to be trapped, leading to a significantly lower non-radiative recombination rate. The reported dielectric constant of $MAPbI_3$ ranges from 18 to 70 [142, 143]. This variation is thought to be mainly caused by crystal formation during different fabrication processes.

While this single observation from one sample of each material is insufficient to draw firm conclusions, it suggests that the improved performance of mixed cation

perovskites may result from less active trap states rather than from a lower density of traps. If confirmed by further studies, this finding could provide new insights into the apparent defect-tolerance of perovskite materials.

6.6 Conclusion

This work has demonstrated an improved method for extracting recombination parameters by fitting a generalised model for recombination kinetics to excitation-dependent steady-state and transient PL measurements. Sensitivity analysis shows that fitting a single model to the two different PL measurements provides improved accuracy in fitting multiple trap parameters compared to fitting to a single type of measurement. Consequently, recombination coefficients and trap parameters, and the associated uncertainties of these fitted parameters are extracted. The quality of the fits obtained with a single trap state suggest that non-radiative recombination is either dominated by a single trap species, or that the combined contribution of active traps can be approximated by a single set of 'effective' trap parameters. Further studies are required to resolve which of these interpretations is correct. Nevertheless, the analysis techniques presented here provide a simple, non-contact method to rapidly characterise the key trap properties of perovskite films, and may lead to new insights into recombination kinetics.

Chapter 7 Carrier Lifetime Interpretation

In this chapter, the recombination model described in Section 3.3.2 is used to simulate the expected PL intensities and PL lifetimes of perovskite films in steady-state and transient measurements. Two different interpretations of carrier lifetime – bi-exponentially fitted time constants and excitation-dependent effective carrier lifetime, are investigated. The origins of the numerically fitted time constants are revealed using the recombination model. A method of estimating recombination coefficients from the relationship between carrier density and carrier lifetime is proposed.

7.1 Introduction

Carrier lifetime is generally extracted from transient measurements of photoluminescence decay or photoconductance decay after excitation with a known generation rate. The decay curves are fitted by an exponential equation to extract the effective carrier lifetimes [62, 65, 66]. As discussed in Section 2.6, the most commonly used method of measuring carrier lifetime in perovskite films is transient PL decay. From transient PL measurements presented in the last Chapter, it was found that under typical measurement conditions the PL decay curves of perovskite films do not follow a single exponential decay (Figure 6.5 b and d). This behaviour is also observed by many other groups [62, 65]. Therefore, a bi-exponential equation (Equation 7.1) is frequently applied to fit the experimental data of lifetime measurements, where τ_1 and τ_2 are the fitted time constants, and a is the weighting factor of the initial fast decay.

$$PL = aexp\left(-\frac{t}{\tau_1}\right) + (1-a)exp\left(-\frac{t}{\tau_2}\right) \qquad 7.1$$

This interpretation of carrier lifetimes simply extracts two time constants numerically. However, the underlying physical significance of τ_1 and τ_2 is not obvious. Many researchers explained that τ_1 is related to trap-assisted recombination and τ_2 is related to radiative recombination [65, 130, 144, 145].

When measuring the transient PL of perovskite solar cells, variations in the initial time constant τ_1 have been observed for perovskite films with different interfaces: pure

$CH_3NH_3PbI_3$ film, $CH_3NH_3PbI_3$/PCBM film, and $CH_3NH_3PbI_3$/Spiro-OMeTAD film [130]. τ_2 almost remains the same in these cases. Lewis Base treatment has been used to passivate the surface recombination of perovskite films [144]. The initial fast decay process was effectively removed by the surface passivation comparing the PL decay curves measured before and after the treatment.

These results imply that the fast decay could be dominated by surface recombination and the slow decay is related to the bulk radiative recombination within the perovskite layer. Surface recombination is one type of trap-assisted recombination, since the surfaces and interfaces are more likely to contain a large amount of recombination centres such as impurities and dangling bonds. Thus, surface recombination rate can be written as a similar equation as the steady-state SRH recombination rate (Equation 3.25) when a single surface state is assumed [146].

$$U_A = \frac{S_{e0}S_{h0}(np - n_i^2)}{S_{e0}(n + n_1) + S_{h0}(p + p_1)}, \qquad 7.2$$

where U_A is the net surface recombination rate per unit area, and S_{e0} and S_{h0} are surface recombination velocities of electrons and holes, respectively. A number of recent works focussing on surface passivation suggest that surface recombination may be the dominant source of trap-assisted recombination in high-efficiency perovskite cells.

Time-resolved PL has also been measured on perovskite single crystals, where the laser beam can be focussed at the surface or into the bulk of the crystal [145].The weighting of the initial fast decay is obviously larger for the measurements performed at the crystal surface. Here, the surface of a single crystal could be considered as grain boundaries where dangling bonds, surface dislocations, under-coordinated atoms and chemical impurities exist. Thus, τ_1 of a perovskite single crystal depends on trap-assisted recombination dominated by the recombination at the crystal surfaces; and τ_2 depends on the radiative recombination inside the crystal.

Dane W. de Quilettes once conducted spatially transient PL decay measurements across polycrystalline perovskite films [65]. The decay curves extracted at grain boundaries showed an obvious transition from fast decay to slow decay; while the PL decay measured in the middle of the grain follows a slow decay process (Figure 2 in

[65]). On polycrystalline perovskite films, traps are thought to accumulate at grain boundaries, where trap-assisted recombination dominates due to the high trap density. Therefore, this bi-exponential PL decay is also detected on perovskite films, and trap-assisted recombination at the grain boundaries leads to a fast decay of carrier lifetime before the slow decay, dominated by charge carrier radiative recombination, appears.

The mechanism of bi-exponential decay of the time-resolved PL measurements has been observed and discussed on perovskite solar cells [130, 144], single crystals [145] and thin films [65]. It is generally agreed that the transition in decay rate is due to the high trap density which leads to an initial fast decay due to carrier trapping. Thus, time constants τ_1 and τ_2 may be related to trap-assisted recombination and band-to-band radiative recombination, respectively [147]. This interpretation of carrier lifetime with bi-exponential decay is useful to compare the quality of perovskites between samples. However, the physics of recombination kinetics is much more complicated and the two time constants are insufficient to explain the mechanisms of recombination in perovskites.

As discussed in Section 2.6, the carrier lifetime in a film is not a constant value, since it strongly depends on the carrier density during the measurement. Therefore, excitation-dependent transient lifetime is a way to interpret the carrier lifetime from the physical origins. This approach is widely used for evaluating silicon materials under steady-state conditions [88, 148]. Since the carrier lifetime of perovskite films is measured by the transient PL decay, where the carrier density varies by orders of magnitude during the measurement, the physical meaning of the transient lifetime extracted from the slope of the decay curve should be studied. Also, it is important to understand whether the carrier lifetime extracted from transient measurements is equivalent to steady-state carrier lifetime in order to analyse the relationship between carrier density and carrier lifetime in perovskite materials.

In this chapter, the general recombination model presented in Section 3.3.2 will be applied to investigate the interpretation of carrier lifetime extracted from time-resolved PL decay measurements on perovskite films. The parameters of recombination coefficients and trap properties used in this model are within the range of the fitted parameters discussed in Chapter 6. Here, the time constants extracted

from the bi-exponential fitting (Equation 7.1) are investigated by varying the input recombination parameters. This analysis indicates that the fitted time constants and weighting factor are strongly related to trap density, doping density and trap energy levels. Additionally, the effective carrier lifetime extracted from the slope of transient PL decay curves turns out to be very similar to the minority carrier lifetime. The excitation-dependent carrier lifetimes generated from both steady-state and transient model are compared. The result demonstrates that the transient lifetimes modelled at both conditions are equal only at high excitation levels. This can be used to analyse radiative and Auger recombination rate since these recombination mechanisms dominate at high excitation levels. The excitation-dependent carrier lifetime at low excitation levels is also investigated to illustrate the effects of trap energy levels on the shape of the curve.

7.2 Investigation of fitted time constants

In Chapter 6, a general model for transient recombination kinetics was presented and applied to both steady-state and transient PL measurements. With this recombination model, the PL lifetime decay curves can be simulated with experimentally-determined parameters, thus providing a way to understand the effects of trap properties on the effective carrier lifetime.

Firstly, the modelled decay curve is fitted to Equation 7.1 for extracting the weighting factor a and time constants τ_1 and τ_2. The fixed parameters in this model are listed in Table 7.1 and the modelled and fitted curves are shown in Figure 7.1. The fitted results are $a = 0.896$, $\tau_1 = 10.3$ ns and $\tau_2 = 164.3$ ns. With these values as a starting point, further investigation has been done to sweep the pre-set values of some of the parameters in the model to better understand the physical parameters that determine the general shape of PL decay curves.

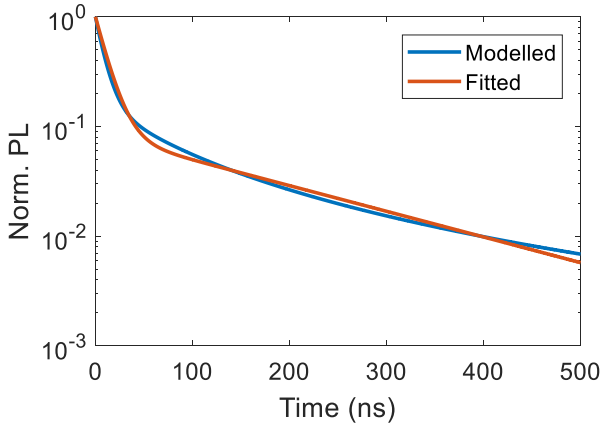

Figure 7.1 The blue line is the PL decay curve generated by the recombination model described in Section 3.3.2 using parameters listed in Table 7.1. The red line is the fitted curve of the blue line using Equation 7.1.

Table 7.1 Parameters used in the recombination model.

$B\ (cm^3 s^{-1})$	1×10^{-11}
$N_t\ (cm^{-3})$	1×10^{16}
$E_t\ (eV)$	0.20
$\langle c_n \rangle\ (cm^3 s^{-1})$	1×10^{-8}
$\langle e_n \rangle\ (cm^3 s^{-1})$	5×10^{-9}
$\Gamma\ (cm^6 s^{-1})$	1×10^{-31}
$N_A\ (cm^{-3})$	3×10^{14}
$Excitation\ level\ (cm^{-3})$	1.4×10^{15}

First, the trap density is increased from $1 \times 10^{16}\ cm^{-3}$ to $8 \times 10^{16}\ cm^{-3}$, and all the other parameters remain the same as listed in Table 7.1. It is obvious that the initial decay constant τ_1 decreases as the trap density increases (Figure 7.2). This trend is clearly demonstrated from the fitted parameters listed in Table 7.2. Doubling the trap density (N_t) in the perovskite film almost reduces the fast decay constant τ_1 to half. However, τ_2 in this case does not show obvious change, implying that the fast decay τ_1 scales approximately with $1/N_t$ in the perovskite film.

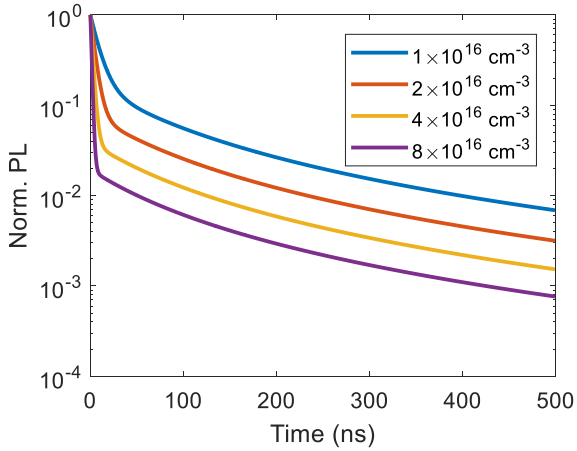

Figure 7.2 The modelled PL decay curves with trap density N_t varied from $1 \times 10^{16}\ cm^{-3}$ to $8 \times 10^{16}\ cm^{-3}$.

Table 7.2 The fitted values of a, τ_1 and τ_2 for different input trap densities.

$N_t\ (cm^{-3})$	a	$\tau_1 (ns)$	$\tau_2 (ns)$
1×10^{16}	0.896	10.3	164.3
2×10^{16}	0.946	5.2	154.1
4×10^{16}	0.972	2.6	147.4
8×10^{16}	0.985	1.3	142.8

When sweeping the doping density N_A, only the slow decay time constant τ_2 is changed (Figure 7.3 and Table 7.3). The increase in doping density leads to a reduction of equilibrium minority carrier density (electron is the minority carrier in this case). The rate of fast decay, which is considered to be related to the trapping of free electrons, will not be affected by the reduction of equilibrium electron density, since it is

negligibly small compared to the high density of photogenerated free electrons. However, after the fast recombination of free carriers, the equilibrium electron density is no longer negligible, and as a result, the radiative recombination rate decreases with the reduction of equilibrium minority carrier density in the slow decay regime.

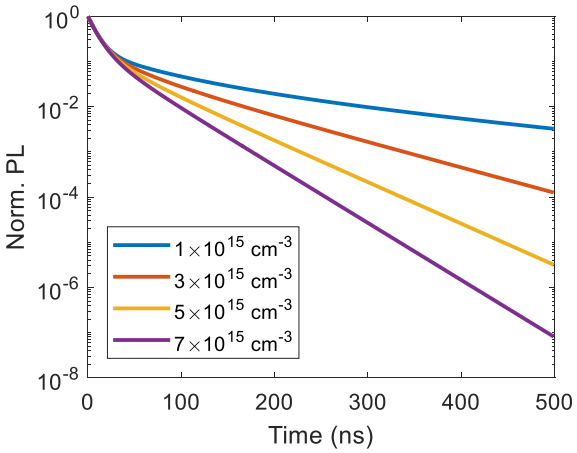

Figure 7.3 The modelled PL decay curves with doping density N_A varied from $1 \times 10^{15}\ cm^{-3}$ to $7 \times 10^{15}\ cm^{-3}$.

Table 7.3 The fitted values of a, τ_1 and τ_2 for different input doping densities.

$N_A\ (cm^{-3})$	a	$\tau_1(ns)$	$\tau_2(ns)$
1×10^{15}	0.899	10.4	133.3
3×10^{15}	0.885	10.2	71.4
5×10^{15}	0.857	9.8	46.2
7×10^{15}	0.820	9.4	34.1

Interestingly, the variation of trap energy levels E_t does not affect the time constants. It only changes the weighting of fast and slow decay (Figure 7.4 and Table 7.4). The initial fast decay lasts longer when the trap energy level approaches the midgap, which is indicated by the increase of the weighting factor a. When the traps become deeper, more traps act as recombination centres. Therefore, the trap-assisted recombination rate increases and radiative recombination rate decreases, resulting in a reduction of PL intensity throughout the decay. In the meantime, due to the increased trap energy level, more carriers are recombined via traps rather than band-to-band. Since the densities of electrons, holes and traps, and the capture cross-section of electrons and holes are fixed, the increase of SRH recombination rate comes from the increased percentage of carriers involved in this recombination mechanism. Thus, the carrier lifetimes remain the same, and the recombination weighting factor a increases.

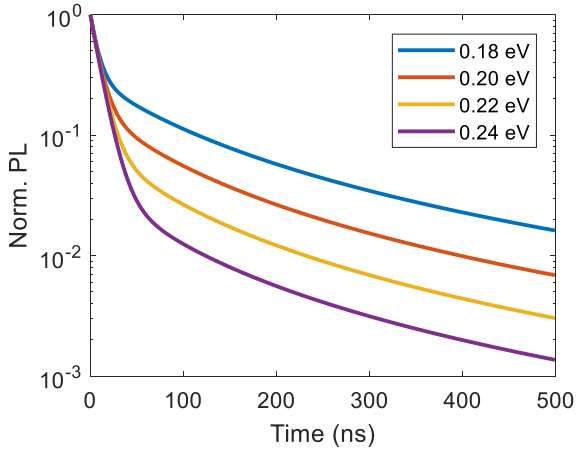

Figure 7.4 The modelled PL decay curves with trap energy level E_t varied from $0.18\ eV$ to $0.24\ eV$.

Table 7.4 The fitted values of a, τ_1 and τ_2 for different input trap energy levels.

$E_t\ (eV)$	a	$\tau_1(ns)$	$\tau_2(ns)$
0.18	0.793	9.4	175.0
0.20	0.896	10.3	164.3
0.22	0.951	10.6	160.8
0.24	0.978	10.7	160.7

From the demonstrated relationships between the recombination parameters and the fitted numerical parameters, it can be summarised that the initial fast decay is due to free carriers being captured by traps in the perovskite film and the following slow decay is dominated by the charge carrier radiative recombination which purely depends on the density of free carriers.

7.3 Investigation of effective carrier lifetime

As shown in the previous section, the fitting of exponential decay constants τ_1 and τ_2 to PL decay curves provides a simple parameterisation of the decay curves, but it is difficult to infer direct physical meaning from the extracted values. As discussed in Section 2.6, the effective lifetime of minority carriers changes along with the measurement conditions. This effective carrier lifetime can be described as a function of carrier density. From this relationship, Auger recombination coefficients can be extracted from the gradient of the curve at high excitation levels.

Since the carrier density and lifetime at each time point of the decay are calculated in the model, the total lifetime of electrons and holes can be plotted as a function of time (red and yellow curves in Figure 7.5a). This shows that the lifetime of electrons and holes are not equal during the first 50 ns when fast decay occurs (see Figure 7.1); during the slow PL decay, the difference in lifetimes between electrons and holes is negligible. Alternatively, the transient effective lifetime can also be extracted from the slope of the PL decay curve (blue curve in Figure 7.5a). This approach could be used to extract a time-dependent lifetime from experimental data, which might be a more justified method for extracting lifetime than exponential fits. The lifetime calculated

from the slope of the PL decay curve follows the trend of minority carrier lifetime (electrons are the minority carriers in the model). The fraction of occupied traps (f_t) is plotted as a function of time in Figure 7.5b, showing that an increasing number of electrons are captured by traps during the first 50 ns (fast decay region in Figure 7.1). This further supports the conclusion of the previous section that the fast decay is dominated by the kinetics of free carrier trapping.

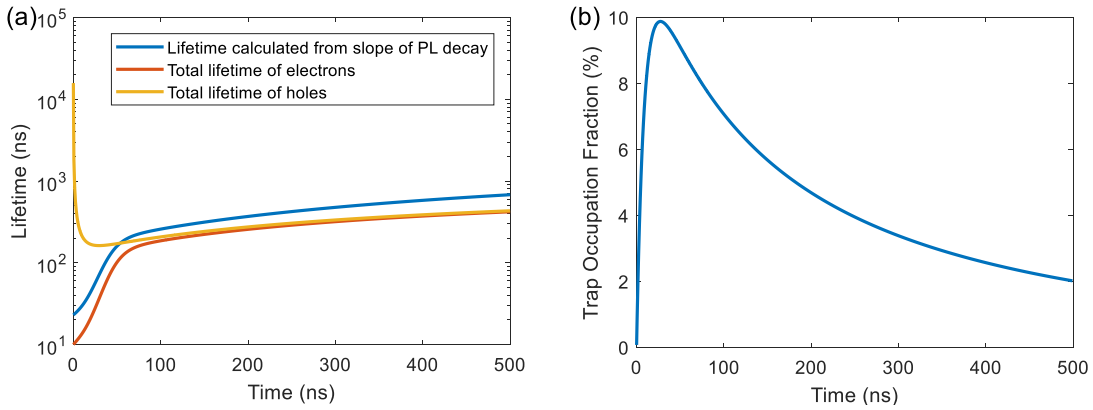

Figure 7.5 (a) The modelled total lifetimes of electrons and holes as a function of time during the PL decay (red and yellow lines, respectively), and the transient lifetime calculated from the slope of the PL decay curve (blue line). (b) The modelled fraction of occupied traps f_t as a function of time during the PL decay.

From the study of silicon wafers, the effective carrier lifetime strongly depends on the carrier density during the measurement [88]. The simulated excitation-dependent steady-state PL is demonstrated in Chapter 6. During the simulation, steady-state recombination rates and carrier densities are also calculated for each excitation level (Figure 7.6a). Thus, the carrier lifetime can be plotted as a function of excess minority carrier density (Δn) in Figure 7.6b.

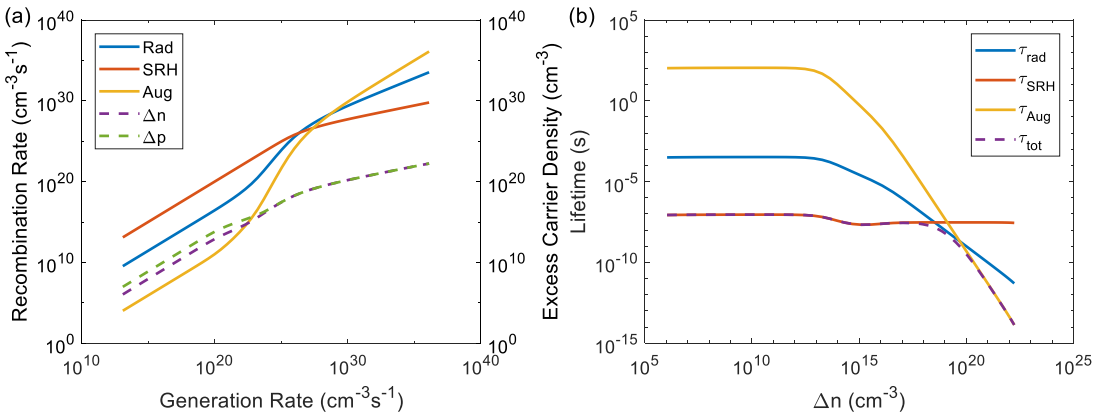

Figure 7.6 (a) The modelled steady-state radiative (blue solid line), SRH (red solid line) and Auger (yellow solid line) recombination rates, and the modelled excess densities of electrons (purple dash line) and holes (green dash line) as

a function of generation rate. (b) The modelled radiative (blue solid line), SRH (red solid line), Auger (yellow solid line) and total (purple dash line) lifetimes of electrons as a function of excess electron density.

It is shown in Figure 7.6a that the excess densities of electrons and holes are equal when $\Delta n = \Delta p > 10^{18}\ cm^{-3}$. The measured transient lifetimes above this excitation level can be used to estimate the coefficients of recombination kinetics. At extremely high excitation levels ($\Delta n > 10^{20}\ cm^{-3}$), Auger recombination dominates, and as a result, the total lifetime is approximated by the Auger recombination lifetime (Figure 7.6b). Also, the excess carrier densities (Δn and Δp) are much larger than the equilibrium carrier densities (n_0 and p_0). Thus, the sum of Auger recombination coefficients ($\Gamma_n + \Gamma_p$) can be approximated to $1/(\tau_{tot}\Delta n^2)$ (Equation 7.3).

$$\frac{\Delta n}{\tau_{tot}} = U_{Aug} = \Gamma_n n(np - n_i^2) + \Gamma_p p(np - n_i^2) \approx (\Gamma_n + \Gamma_p)\Delta n^3 \qquad 7.3$$

The expression of $1/(\tau_{tot}\Delta n^2)$ was plotted as a function of the excess density of electrons in Figure 7.7a (blue solid curve), and the input value of ($\Gamma_n + \Gamma_p$) has been shown as red dash line in the figure. The minimum value of $1/(\tau_{tot}\Delta n^2)$ is achieved and stabilised when Δn is greater than $10^{20}\ cm^{-3}$, which equals to the sum of Auger recombination coefficients in the model.

In a small range of excitation levels ($10^{18}\ cm^{-3} < \Delta n < 10^{20}\ cm^{-3}$), the total lifetime of electrons is approximately the same as the radiative recombination lifetime. Applying a similar approach to Auger recombination coefficients, an estimation of the radiative recombination coefficient B can be expressed as $1/(\tau_{tot}\Delta n)$ derived from Equation 7.4.

$$\frac{\Delta n}{\tau_{tot}} = U_{rad} = B(np - n_i^2) \approx B\Delta n^2 \qquad 7.4$$

The expression of $1/(\tau_{tot}\Delta n)$ was plotted as a function of the excess density of electrons in Figure 7.7b (blue solid curve), and the input value of B has been shown as red dash line in the figure. The minimum value of $1/(\tau_{tot}\Delta n)$ is achieved when Δn is close to $10^{19}\ cm^{-3}$, and the estimated radiative recombination coefficient from the relationship between carrier density and carrier lifetime is close to the input value. This small overestimation indicates that the excess carrier densities (Δn and Δp) at this excitation level are not high enough so that the equilibrium carrier densities (n_0 and p_0) can be completely ignored.

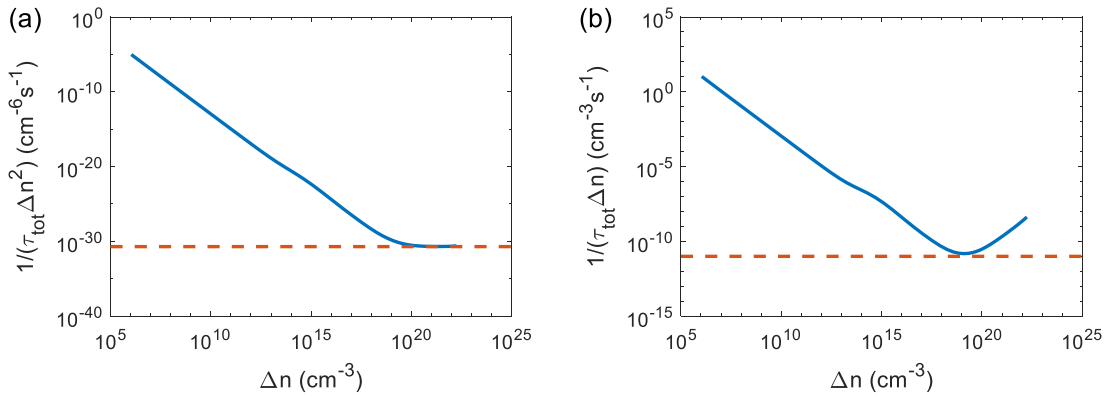

Figure 7.7 (a) The plot of $1/(\tau_{tot}\Delta n^2)$ as a function of excess minority carrier density for estimating the sum of Auger recombination coefficients ($\Gamma_n + \Gamma_p$). The red dash line is the input value of ($\Gamma_n + \Gamma_p$). (b) The plot of $1/(\tau_{tot}\Delta n)$ as a function of excess minority carrier density for estimating the radiative recombination coefficient B. The red dash line is the input value of B.

At low excitation levels, SRH recombination dominates the total recombination kinetics (Figure 7.6b). However, Δn and Δp are not equal and are smaller than the doping density N_A. Therefore, SRH recombination coefficients are difficult to estimate from the excitation-dependent carrier lifetime. This raises the question: *does the slope of τ_{tot} (the purple dash line in Figure 7.6b) have any meaning at low excitation levels?* Khama derived the differential dependence of carrier lifetime on excess carrier density for a single trap state from the expression of lifetime at low-level injection (Eq. (57) in [148]):

$$\frac{d\tau_{tot}}{d\Delta n} = \frac{\tau_{p0}(p_0 - n_1) + \tau_{n0}(n_0 - p_1)}{(n_0 + p_0 + \Delta n)^2}, \qquad 7.5$$

showing the relationship between the gradient of transient carrier lifetime and the trap energy levels. In the model of perovskite film used in this thesis, it is assumed that the material is a p-type semiconductor (the value of N_A is indicated in Table 7.1) as reported by other groups [72], thus the equilibrium hole density (p_0) is much higher than the equilibrium electron density (n_0). Four different cases of trap energy levels are considered below:

- When the trap energy level is close to the conduction band, p_1 is very small. So, the second term of the numerator is negligible. While in the first term, n_1 increases as E_t approaches to E_C, until it is larger than p_0. Thus, the gradient of the lifetime should be negative as is seen for the blue curve ($E_C - E_t = 0.2\ eV$) in Figure 7.8.

- When the trap energy level is close to the midgap, the values of n_1 and p_1 are close to the intrinsic carrier density n_i. Thus, the first term of the numerator is positive and the second term is negative. In a heavily doped p-type semiconductor, p_0 is much larger than n_i, therefore, the positive term dominates, showing an increase of lifetime when increasing carrier density (red curve in Figure 7.8).
- When the trap energy level is close to the valence band, n_1 is small and p_1 is large. Still, the first term is positive and the second term is negative. In the p-type semiconductor, the Fermi level E_F is below the intrinsic level E_i ($E_C - E_F = 1.35\ eV$ in this case). For the traps lying between E_F and E_i, the first positive term of the numerator dominates, thus the gradient of the yellow curve is also positive.
- For shallow traps close to valence band, it can be assumed that E_t lies even below E_F. In this case, the negative term dominates, shown as the purple curve ($E_C - E_t = 1.4\ eV$) in Figure 7.8.

Therefore, the dependence of carrier lifetime on carrier density at low excitation levels can be used to estimate the energy level of the traps.

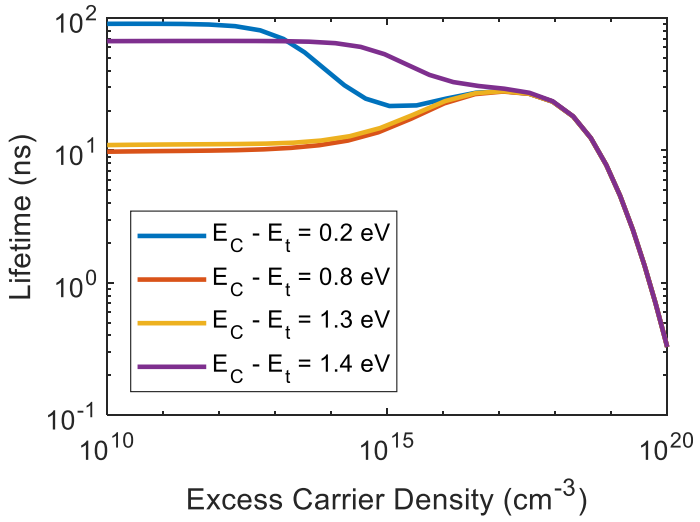

Figure 7.8 The modelled minority carrier lifetime as a function of excess minority carrier density with different input trap energy levels.

Although steady-state carrier lifetime plots such as those simulated in Figure 7.6 and Figure 7.8 provide information about recombination kinetics, it is difficult to extract these values experimentally. In practice, the effective carrier lifetime is usually

measured by transient PL decay. As illustrated in Figure 7.5, an effective carrier lifetime can be directly extracted from the slope of the PL decay curve. Before interpreting such data, it is necessary to verify that the carrier lifetime extracted from transient PL measurements is equivalent to the steady-state excitation-dependent minority carrier lifetime. Due to the large trap density in perovskite films, the minority carrier lifetime in the transient condition is expected to be affected by carrier trapping, especially when the excitation density is lower than the trap density [147]. In Figure 7.9a, the transient PL is modelled with an extremely high initial excitation level, so that a wider range of carrier densities can be covered in a single transient PL decay curve. In this case, most traps are filled during the pulsed laser excitation, so that the carrier lifetimes of electrons and holes are similar. The effective carrier lifetime extracted from the slope of the curve in Figure 7.9a can also be used to represent the minority carrier lifetime (Figure 7.9b).

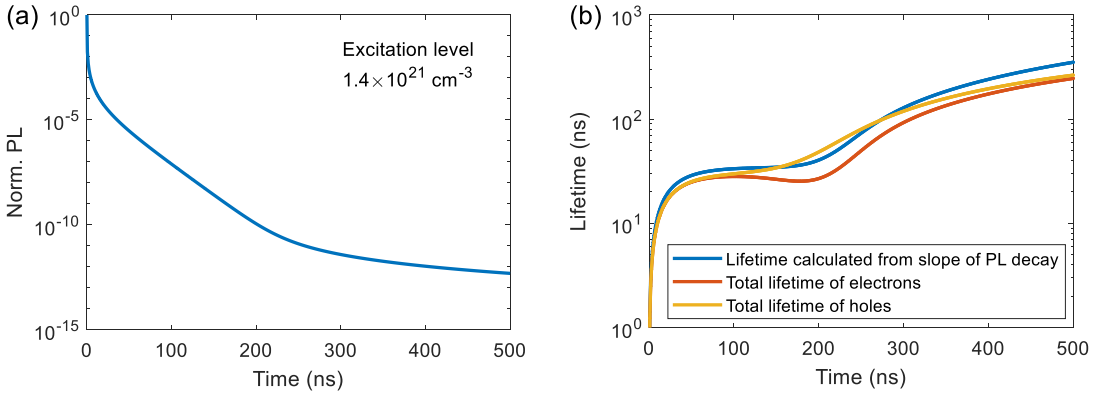

Figure 7.9 (a) The modelled PL decay curve at an excitation density of $1.4 \times 10^{21}\ cm^{-3}$*. (b) The modelled total lifetimes of electrons and holes as a function of time during the PL decay in (a) (red and yellow lines, respectively), and the transient lifetime calculated from the slope of the PL decay curve in (a) (blue line).*

Replotting the time-dependent total lifetime of electrons in Figure 7.9b (the red curve) as a function of excess minority carrier density generates the solid red curves in Figure 7.10. The effective carrier lifetime extracted from the steady-state model (the purple curve in Figure 7.6b) is also plotted in the same figure as blue dots. This comparison indicates that at high excitation levels where radiative recombination or Auger recombination is dominant, the relationship between excess minority carrier density and carrier effective lifetime generated by both the steady-state model and transient model are almost identical. However, the effective lifetime is overestimated in the transient model at low excitation levels. The reason for this is that, unlike the steady-

state equilibrium SRH recombination rate, the SRH recombination rates of electrons and holes are not always equal in the transient condition, especially at low excitation levels. The SRH recombination rate of minority carriers is reduced due to trapping, and thus the lifetime of minority carriers will be prolonged ($\tau_n = \frac{\Delta n}{U_n}$). Therefore, the effective carrier lifetime extracted from the time-resolved PL decay measurement can only be used to represent the steady-state effective lifetime at high excitation levels ($\Delta n \geq N_t = 10^{16}\ cm^{-3}$ in the model), which is sufficient to estimate radiative and Auger recombination coefficients from the relationship between carrier lifetime and carrier density. However, due to the difference between the steady-state lifetime and transient lifetime at low excitation levels ($\Delta n < N_t$), it is risky to use the shape of transient lifetime to infer information about the trap states.

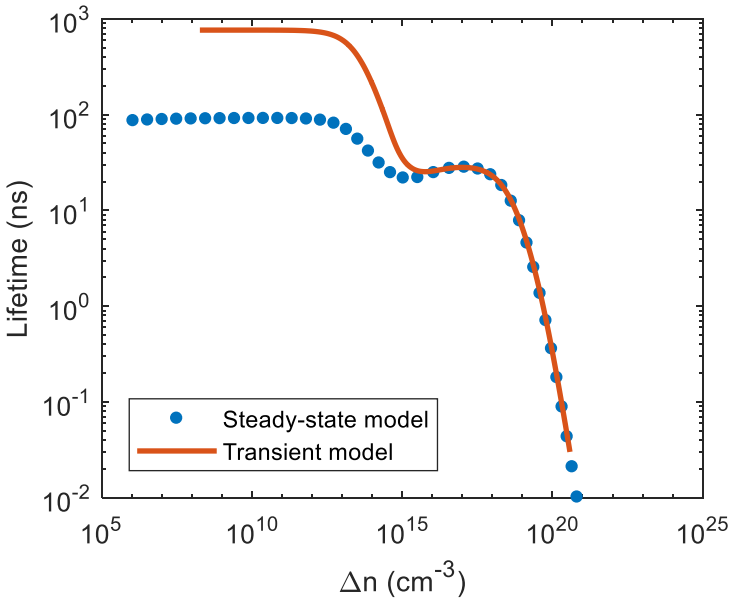

Figure 7.10 The minority carrier lifetime as a function of excess minority carrier density extracted from the modelling of excitation-dependent steady-state PL (blue dots) and the minority carrier lifetime as a function of excess minority carrier density extracted from the modelling of time-resolved PL decay (red line).

Another challenge associated with extracting lifetime data from transient PL measurements is the estimation of the excess carrier density as a function of time. The excess carrier density of electrons and holes during the modelled PL decay (Figure 7.9a) is plotted in Figure 7.11, which shows that the equality of electron density and hole density is valid at high excitation levels ($\Delta n = \Delta p \geq 10^{16}\ cm^{-3}$). Thus, the excess carrier density at this injection range is proportional to $\sqrt{PL}$, and the excitation-dependent carrier lifetime can be extracted from the slope of PL decay curve.

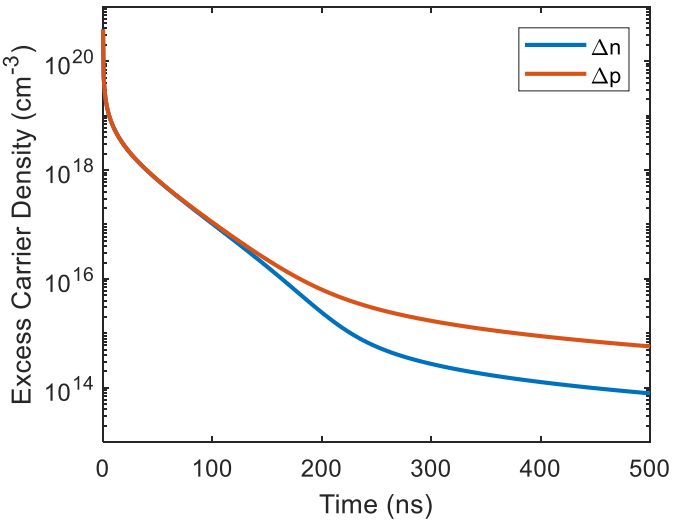

Figure 7.11 The modelled transient excess densities of electrons (blue line) and holes (red line) during the PL decay in Figure 7.9(a).

However, the excess carrier densities of electrons and holes at low excitation levels are no longer equal in this case. Both values cannot be easily determined directly from the transient PL measurement. This further increases the difficulties of estimating trap energy levels from the relationship between carrier density and lifetime at low excitation levels.

7.4 Summary

To summarise, carrier lifetime is an important parameter for analysing recombination kinetics of semiconductor materials. The numerical interpretation of carrier lifetimes extracted by fitting the time-resolved PL decay curve to a bi-exponential equation demonstrates that the fast and slow decays are dominated by trap-assisted recombination and radiative recombination respectively. The physical meaning of carrier lifetime extracted from the gradient of PL decay is also investigated. The extraction and interpretation of transient lifetime, and its relationship to steady-state minority carrier lifetime over a wide excitation range is also discussed. The work in this chapter was solely based on a theoretical analysis of carrier recombination in perovskite films, but the modelled relationships can also be observed experimentally. Further measurements, for example real-time detection of carrier density, could be performed along with the measurement of carrier lifetime to provide a better understanding of recombination kinetics in perovskite materials.

Chapter 8 Conclusion

In this last chapter, key findings and their significance will be summarised in the first section. However, there are still problems that remain unsolved; thus, future work that can be done will be discussed in the second section of this chapter.

8.1 Summary of the thesis

In this work, confocal microscopy was applied to characterise thin film solar cells. The capability of the confocal scanning microscope has been tested by the reflectance and photocurrent mapping of a thin film silicon solar cell coated with silver nanoparticles. The extracted images at a wide range of excitation spectra (from visible to near inferred) visually demonstrated that the photocurrent of the solar cell was enhanced by the surface nanostructure when the excitation wavelength larger than 750 nm due to the light trapping. This observation was verified by the optical simulation on Lumerical FDTD Solution.

Perovskite thin films are unstable in high temperature, high intensity exposure and humid air. Firstly, the potential local heating that could occur due to the laser illumination has been simulated showing only a few degrees of temperature rise under the typical confocal measurement conditions. Next, time-dependent photoluminescence measurements were compared for bare perovskite films, PMMA coated films, fully encapsulated films and films stored in an N_2 environment. These measurements demonstrated that the PMMA coating could effectively protect the perovskite films from rapid degradation, but not the oxygen-induced PL enhancement. Full encapsulation and/or measuring films under ambient N_2 gas can ensure the stability of perovskite films for several tens of minutes of laser exposure during photoluminescence characterisation. The stability tests verified that the perovskite films were sufficiently stable to allow for reliable and repeatable measurements in a single location using a wide range of illumination intensities.

During the stability tests, light- and oxygen-induced PL enhancements were observed. Further studies indicated that this observation was caused by the de-activation of traps in the perovskite films, as had also been proposed by several other groups at the time

[41, 42]. With the reduction of active trap density, the trap-assisted recombination rate was reduced, so that the radiative recombination rate, which is proportional to the PL intensity, increases. This oxygen-assisted trap de-activation process is reversible. Keeping the PL enhanced sample in the dark with N_2 gas flow for a sufficiently long time, the PL emission of the film was observed to drop back to the original intensity, indicating that the traps were only temporarily de-activated by the oxygen species. Additionally, confocal scanning PL measurements were applied to extract images of the PL enhanced area which demonstrated the lateral expansion of the PL enhancement over more than 5 μm within a 20 min laser exposure. This has been attributed to photogenerated charge carrier diffusion away from the illuminated area. A recombination model was used to simulate the dynamics of photocarriers and traps, which provided solid theoretical support to the discussion and analysis of time-and spatial-dependent light induced trap de-activation in perovskite films.

The second major piece of research reported in this thesis focussed on understanding the recombination kinetics of perovskite films from the results of excitation-dependent steady-state and transient PL measurements. Here, a general recombination model was used to simulate the radiative recombination rate, taking into account the fundamental properties of trap states and intrinsic recombination mechanisms. By fitting the experimental results to the recombination model, the recombination coefficients, trap properties and doping density of the perovskite films could be extracted. This method has been applied to widely-studied $MAPbI_3$ perovskite films and the high-performance $Cs_{0.07}Rb_{0.03}FA_{0.765}MA_{0.135}PbI_{2.55}Br_{0.45}$ perovskite films. A detailed sensitivity analysis was also performed to check the goodness of fit of each parameter. Comparison of the fitted parameters of the two perovskite compositions suggests that a significant reduction in capture cross-section was the major reason of the high open-circuit voltage measured on quadruple-cation perovskite solar cells.

Using the comprehensive recombination model, the theoretical interpretation of carrier lifetime for perovskites was discussed in Chapter 7. Two time constants were extracted from the bi-exponential fit of the PL decay curve measured on perovskite films. By varying the trap density, doping density and trap energy level in the model, it was demonstrated that the fast decay constant was related to the trap-assisted

recombination kinetic and the slow decay constant was dominated by the band-to-band radiative recombination rate of the perovskite films.

The model also indicated that the transient carrier lifetime extracted from the slope of the PL decay curve was associated with the minority carrier lifetime. From the gradient of the curve plotted by the steady-state carrier lifetime as a function of minority carrier density, the radiative and Auger recombination coefficients were extracted from the slope at high excitation levels, which agreed with the input values of the model. Additionally, the trap energy level can be roughly estimated from the shape of the steady-state excitation-dependent carrier lifetime curve at low excitation level. Comparing the effective lifetimes simulated under steady-state and transient conditions, we found that at high excitation levels the carrier lifetime extracted from transient PL decay curves matched the steady-state carrier lifetime, which could be used to estimate Auger recombination coefficient experimentally.

In this thesis, the investigation of oxygen-induced PL enhancement in perovskite films implies the potential of improving film quality by de-activating traps, which provides a new insight for improving the performance of perovskite solar cells. A new characterisation method has been developed to extract recombination parameters from a combination of steady-state and transient PL measurements. The comparison of recombination parameters between perovskite films illustrates the origins of perovskite solar cells with better performance. Finally, the fundamentals of carrier lifetime in semiconductors have been investigated, which provides a deeper understanding of recombination in perovskite materials.

8.2 Future work

For the research of perovskite solar cells, characterisation of perovskite thin films is one of the most important aspects for improving the device performance. There are still many follow-up studies can be undertaken if the experiments can be set up.

i. In the study of oxygen-assisted light induced PL enhancement (Chapter 5), the time-dependent PL intensity could be measured in an O_2 environment in order to unambiguously observe the effect of O_2 on the perovskite films. Such measurements could also be used to estimate the diffusivity of oxygen species in the perovskite films.

ii. From the sensitivity analysis of the curve fitting in Chapter 6, it was found that radiative and Auger recombination coefficients are not very sensitive in the fitting of present measurement results. If the excitation levels could be further extended in both steady-state and transient PL measurements, the domination of radiative recombination would be more obvious at extremely low excitation levels and the effect of Auger recombination would be stronger at extremely high excitation levels. Thus, those two parameters can be estimated more accurately.

iii. In Chapter 7, the theoretical interpretation of carrier lifetime has been introduced; however, experimental analysis is required to support these interpretations. Measuring excess carrier density is challenging in perovskite films, which is normally extracted from the relationship between photoconductance and carrier mobility. However, the estimation of carrier mobility requires one to know the value of carrier density at the measurement condition. Therefore, the development of a reliable method to independently estimate excess electron and hole densities in perovskite films would be very useful for more detailed recombination studies.

iv. From the measurements of trap states reviewed in Chapter 2, it is known that there are multiple types of traps located at different energy states in perovskite materials. However, a single trap state was assumed in the recombination model for simplification (as has also been done in many other works [72, 73]). The parameter sensitivity of the current model fitting would be reduced if more uncertainties were introduced into the model. Therefore, more measurement results associated with trap-assisted recombination should be used to fit the model to ensure the accuracy of the fitting. This potential study could further improve a more fundamental understanding of recombination kinetics perovskite materials.

List of Figures

List of Tables

List of Publications

Journal papers

1. **X. Fu**, K. J. Weber and T. P. White, Characterization of Trap States in Perovskite Films by Simultaneous Fitting of Steady-state and Transient Photoluminescence Measurements, Journal of Applied Physics, 2018, **124** (7), 073102.
2. H. Shen, T. Duong, J. Peng, D. Jacobs, N. Wu, J. Gong, Y. Wu, S. K. Karuturi, **X. Fu**, K. J. Weber, X. Xiao, T. P. White and K. R. Catchpole, Mechanically-stacked Perovskite/CIGS Tandem Solar Cells with Efficiency of 23.9% and Reduced Oxygen Sensitivity, Energy & Environmental Science, 2018, **11** (2), 394-406.
3. Y. Wu, D. Yan, J. Peng, T. Duong, Y. Wan, S. P. Phang, H. Shen, N. Wu, C. Barugkin, **X. Fu**, S. Surve, D. Grant, D. Walter, T. P. White, K. R. Catchpole and K. J. Weber, Monolithic Perovskite/Silicon-Homojunction Tandem Solar Cell with over 22% Efficiency, Energy & Environmental Science, 2017, **10** (11), 2472-2479.
4. N. Wu, Y. Wu, D. Walter, H. Shen, T. Duong, D. Grant, C. Barugkin, **X. Fu**, J. Peng, T. P. White, K. R. Catchpole and K. J. Weber, Identifying the Cause of Voltage and Fill Factor Losses in Perovskite Solar Cells by Using Luminescence Measurements, Energy Technology, 2017, **5** (10), 1827-1835.
5. T. Duong, H. K. Mulmudi, Y. Wu, **X. Fu**, H. Shen, J. Peng, N. Wu, H. T. Nguyen, D. H. MacDonald, M. N. Lockrey, T. P. White, K. J. Weber and K. R. Catchpole, Light and Electrically Induced Phase Segregation and Its Impact on the Stability of Quadruple Cation High Bandgap Perovskite Solar Cells, ACS Applied Materials and Interfaces, 2017, **9** (32), 26859-26866.
6. J. Peng, Y. Wu, W. Ye, D. A. Jacobs, H. Shen, **X. Fu**, Y. Wan, T. Duong, N. Wu, C. Barugkin, H. T. Nguyen, D. Zhong, J. Li, T. Lu, Y. Liu, M. N. Lockrey, K. J. Weber, K. R. Catchpole and T. P. White, Interface Passivation Using Ultrathin Polymer-fullerene Films for High-efficiency Perovskite Solar Cells with Negligible Hysteresis, Energy & Environmental Science, 2017, **10** (8), 1792-1800.
7. H. Shen, D. A. Jacobs, Y. Wu, T. Duong, J. Peng, X. Wen, **X. Fu**, S. K. Karuturi, T. P. White, K. J. Weber and K. R. Catchpole, Inverted Hysteresis in $CH_3NH_3PbI_3$ Solar

Cells: Role of Stoichiometry and Band Alignment, Journal of Physical Chemistry Letters, 2017, **8** (12), 2672-2680.

8. T. Duong, Y. Wu, H. Shen, J. Peng, **X. Fu**, D. A. Jacobs, E.-C. Wang, T. C. Kho, K. C. Fong, M. Stocks, E. Franklin, A. W. Blakers, N. Zin, K. R. McIntosh, W. Li, Y.-B. Cheng, T. P. White, K. J. Weber and K. R. Catchpole, Rubidium Multication Perovskite with Optimized Bandgap for Perovskite-Silicon Tandem with over 26% Efficiency, Advanced Energy Materials, 2017, **7** (14), 1700228.
9. H. Shen, Y. Wu, J. Peng, T. Duong, **X. Fu**, C. Barugkin, T. P. White, K. Weber and K. R. Catchpole, Improved Reproducibility for Perovskite Solar Cells with 1 cm^2 Active Area by a Modified Two-Step Process, ACS Applied Materials & Interfaces, 2017, **9** (7), 5974-5981.
10. **X. Fu**, D. A. Jacobs, F. J. Beck, T. Duong, H. Shen, K. R. Catchpole and T. P. White, Photoluminescence Study of Time- and Spatial-dependent Light Induced Trap De-activation in $CH_3NH_3PbI_3$ Perovskite Films, Physical Chemistry Chemical Physics, 2016, **18** (32), 22557-22564.
11. D. Jacobs, **X. Fu**, K. Weber, K. Catchpole and T. White, Modelling of Slow Transient Processes in Organo-metal Halide Perovskites, 2016 International Conference on Numerical Simulation of Optoelectronic Devices (NUSOD), 2016, 185-186.
12. Z. Li, X. Yuan, L. Fu, K. Peng, F. Wang, **X. Fu**, P. Caroff, T. P White, H. H. Tan and C. Jagadish, Room Temperature GaAsSb Single Nanowire Infrared Photodetectors, Nanotechnology, 2015, **26** (44), 445202.

Conference papers

1. **X. Fu** and T. P. White, Investigating Transient Recombination in Perovskite Film and Extracting Material Properties by Fitting Steady-state PL and Transient PL, International Conference on Perovskite Solar Cells and Optoelectronics, 2017.
2. **X. Fu**, J. Cong, H. Shen, K. J. Weber, K. R. Catchpole and T. P. White, Time-and excitation-dependent photoluminescence characterisation of $CH_3NH_3PbI_3$

perovskite films, Optical Nanostructures and Advanced Materials for Photovoltaics, PTh3B. 4, 2015.

3. **X. Fu**, E. C. Wang, K. R. Catchpole and T. P. White, High-resolution photocurrent imaging of light trapping by plasmonic nanoparticles on thin film Si solar cells, Optical Nanostructures and Advanced Materials for Photovoltaics, JW6A. 27, 2014.

Bibliography

[1] World Meteorological Organisation, “WMO statement on the state of the global climate in 2017,” [Online]. Available: https://public.wmo.int/en/our-mandate/climate/wmo-statement-state-of-global-climate. [Accessed 18 Jun 2018].

[2] “Best research-cell efficiencies,” National Renewable Energy Laboratory, [Online]. Available: https://www.nrel.gov/pv/assets/images/efficiency-chart.png. [Accessed 18 Jun 2018].

[3] T. Tiedje, E. Yablonovitch, G. D. Cody and B. G. Brooks, “Limiting efficiency of silicon solar cells,” *IEEE Transactions on Electron Devices,* vol. 31, no. 5, pp. 711-716, 1984.

[4] W. Shockley and H. J. Queisser, “Detailed balance limit of efficiency of p-n junction solar cells,” *Journal of Applied Physics,* vol. 32, no. 3, p. 510, 1961.

[5] “International technology roadmap for photovoltaic (ITRPV) 2017 results,” [Online]. Available: http://www.itrpv.net. [Accessed 18 Jun 2018].

[6] J. Greulich, A.-K. Volk, N. Wöhrle, I. Haedrich, M. Wiese, M. Hermle and S. Rein, “Optical simulation and analysis of iso-textured silicon solar cells,” *Energy Procedia,* vol. 77, pp. 69-74, 2015.

[7] A. Delamarre, L. Lombez and J.-F. Guillemoles, “Characterisation of solar cells using electroluminescence and photoluminescence hyperspectral images,” *Journal of Photonics for Energy,* vol. 2, no. 1, p. 027004, 2012.

[8] E. Klimov, W. Li, X. Yang, G. G. Hoffmann and J. Loos, “Scanning near-field and confocal raman microscopic investigation of P3HT−PCBM systems for solar cell applications,” *Macromolecules,* vol. 39, no. 13, pp. 4493-4496, 2006.

[9] A. Kojima, K. Teshima, Y. Shirai and T. Miyasaka, “Organometal halide perovskites as visible-light sensitisers for photovoltaic cells,” *Journal of the American Chemical Society,* vol. 131, no. 17, pp. 6050-6051, 2009.

[10] M. Minsky, “Microscopy apparatus”. Patent US003013467, 1961.

[11] K. Carlsson, P. E. Danielsson, R. Lenz, A. Liljeborg, L. Majlof and N. Aslund, “Three-dimensional microscopy using a confocal laser scanning microscope,” *Optical Letters,* vol. 10, no. 2, pp. 53-55, 1985.

[12] J.-H. Im, C.-R. Lee, J.-W. Lee, S.-W. Park and N.-G. Park, “6.5% efficiency perovskite quantum-dot-sensitized solar cell,” *Nanoscale,* vol. 3, no. 10, pp. 4088-4093, 2011.

[13] H.-S. Kim, C.-R. Lee, J.-H. Im, K.-B. Lee, T. Moehl, A. Marchioro, S.-J. Moon, R. Humphry-Baker, J.-H. Yum, J. E. Moser, M. Gratzel and N.-G. Park, “Lead iodide perovskite sensitized all-solid-state submicron thin film mesoscopic solar cell with efficiency exceeding 9%,” *Science Reports,* vol. 2, p. 591, 2012.

[14] G. S. Han, Y. H. Song, Y. U. Jin, J.-W. Lee, N.-G. Park, B. K. Kang, J.-K. Lee, I. S. Cho, D. H. Yoon and H. S. Jung, “Reduced graphene oxide/mesoporous TiO_2 nanocomposite based perovskite solar cells,” *ACS Applied Materials & Interfaces,* vol. 7, no. 42, pp. 23521-23526, 2015.

[15] F. Di Giacomo, V. Zardetto, G. Lucarelli, L. Cinà, A. Di Carlo, M. Creatore and T. M. Brown, “Mesoporous perovskite solar cells and the role of nanoscale compact layers for remarkable all-round high efficiency under both indoor and outdoor illumination,” *Nano Energy,* vol. 30, pp. 460-469, 2016.

[16] J. Y. Seo, R. Uchida, H.-S. Kim, Y. Saygili, J. Luo, C. Moore, J. Kerrod, A. Wagstaff, M. Eklund, R. McIntyre, N. Pellet, S. M. Zakeeruddin, A. Hagfeldt and M. Grätzel, “Boosting the efficiency of perovskite solar cells with CsBr-modified mesoporous TiO_2 beads as electron-selective contact,” *Advanced Functional Materials,* vol. 28, no. 15, p. 1705763, 2017.

[17] M. Liu, M. B. Johnston and H. J. Snaith, “Efficient planar heterojunction perovskite solar cells by vapour deposition,” *Nature,* vol. 501, pp. 395-398, 2013.

[18] S. Colella, E. Mosconi, P. Fedeli, A. Listorti, F. Gazza, F. Orlandi, P. Ferro, T. Besagni, A. Rizzo, G. Calestani, G. Gigli, F. De Angelis and R. Mosca, “$MAPbI_{3-x}Cl_x$ mixed halide perovskite for hybrid solar cells: the role of chloride as dopant on the transport and structural properties,” *Chemistry of Materials,* vol. 25, no. 22, pp. 4613-4618, 2013.

[19] D. P. McMeekin, G. Sadoughi, W. Rehman, G. E. Eperon, M. Saliba, M. T. Hörantner, A. Haghighirad, N. Sakai, L. Korte, B. Rech, M. B. Johnston, L. M. Herz and H. J. Snaith, “A mixed-cation lead mixed-halide perovskite absorber for tandem solar cells,” *Science,* vol. 351, no. 6269, pp. 151-155, 2016.

[20] Y. Cai, S. Wang, M. Sun, X. Li and Y. Xiao, “Mixed cations and mixed halide perovskite solar cell with lead thiocyanate additive for high efficiency and long-term moisture stability,” *Organic Electronics,* vol. 53, pp. 249-255, 2018.

[21] L. Gil-Escrig, C. Momblona, M.-G. La-Placa, P. P. Boix, M. Sessolo and H. J. Bolink, “Vaccum deposited triple-cation mixed-halide perovskite solar cells,” *Advanced Energy Materials,* vol. 8, no. 14, p. 1703506, 2018.

[22] R. G. Balakrishna, S. M. Kobosko and P. V. Kamat, “Mixed halide perovskite solar cells. consequence of iodide treatment on phase segregation recovery,” *ACS Energy Letters,* vol. 3, no. 9, pp. 2267-2272, 2018.

[23] W. S. Yang, B.-W. Park, E. H. Jung, N. J. Jeon, Y. C. Kim, D. U. Lee, S. S. Shin, J. Seo, E. K. Kim, J. H. Noh and S. I. Seok, “Iodide management in formamidinium-lead-halide-based perovskite layers for efficient solar cells,” *Science,* vol. 356, no. 6345, pp. 1376-1379, 2017.

[24] J. Zhao, X. Zheng, Y. Deng, T. Li, Y. Shao, A. Gruverman, J. Shield and J. Huang, “Is Cu a stable electrode material in hybrid perovskite solar cells for a 30-year lifetime,” *Energy & Environmental Science,* vol. 9, no. 12, pp. 3650-3656, 2016.

[25] X. Zheng, B. Chen, J. Dai, Y. Fang, Y. Bai, Y. Lin, H. Wei, X. C. Zeng and J. Huang, "Defect passivation in hybrid perovskite solar cells using quaternary ammonium halide anions and cations," *Nature Energy,* vol. 2, p. 17102, 2017.

[26] W. Chen, Y. Wu, Y. Yue, J. Liu, W. Zhang, X. Yang, H. Chen, E. Bi, I. Ashraful, M. Grätzel and L. Han, "Efficient and stable large-area perovskite solar cells with inorganic charge extraction layers," *Science,* vol. 350, no. 6263, pp. 944-948, 2015.

[27] K. A. Bush, A. F. Palmstrom, Z. J. Yu, M. Boccard, R. Cheacharoen, J. P. Mailoa, D. P. McMeekin, R. L. Z. Hoye, C. D. Bailie, T. Leijtens, I. M. Peters, M. C. Minichetti, N. Rolston, R. Prasanna, S. Sofia, D. Harwood, W. Ma, F. Moghadam, H. J. Snaith, T. Buonassisi, Z. C. Holman, S. F. Bent and M. D. McGehee, "23.6%-efficiency monolithic perovskite/silicon tandem solar cells with improved stability," *Nature Energy,* vol. 2, p. 17009, 2017.

[28] D. Luo, W. Yang, Z. Wang, A. Sadhanala, Q. Hu, R. Su, R. Shivanna, G. F. Trindade, J. F. Watts, Z. Xu, T. Liu, K. Chen, F. Ye, P. Wu, L. Zhao, J. Wu, Y. Tu, Y. Zhang, X. Yang, W. Zhang, R. H. Friend, Q. Gong, H. J. Snaith and R. Zhu, "Enhanced photovoltage for inverted planar heterojunction perovskite solar cells," *Science,* vol. 360, no. 6396, pp. 1442-1446, 2018.

[29] T. A. Berhe, W.-N. Su, C.-H. Chen, C.-J. Pan, J.-H. Cheng, H.-M. Chen, M.-C. Tsai, L.-Y. Chen, A. A. Dubale and B.-J. Hwang, "Organometal halide perovskite solar cells: degradation and stability," *Energy & Environmental Science,* vol. 9, no. 2, pp. 323-356, 2016.

[30] M. I. Asghar, J. Zhang, H. Wang and P. D. Lund, "Device stability of perovskite solar cells - a review," *Renewable and Sustainable Energy Reviews,* vol. 77, pp. 131-146, 2017.

[31] M. Ledinský, P. Löper, B. Niesen, J. Holovský, S.-J. Moon, J.-H. Yum, S. De Wolf, A. Fejfar and C. Ballif, "Raman spectroscopy of organic-inorganic halide perovskites," *Journal of Physical Chemistry Letters,* vol. 6, no. 3, pp. 401-406,

2015.

[32] J. A. Christians, P. A. Miranda Herrera and P. V. Kamat, “Transformation of the excited state and photovoltaic efficiency of $CH_3NH_3PbI_3$ perovskite upon controlled exposure to humidified air,” *Journal of the American Chemical Society,* vol. 137, no. 4, pp. 1530-1538, 2015.

[33] A. M. A. Leguy, Y. Hu, M. Campoy-Quiles, M. I. Alonso, O. J. Weber, P. Azarhoosh, M. van Schilfgaarde, M. T. Weller, T. Bein, J. Nelson, P. Docampo and P. R. F. Barnes, “Reversible hydration of $CH_3NH_3PbI_3$ in films, single crystals, and solar cells,” *Chemistry of Materials,* vol. 27, no. 9, pp. 3397-3407, 2015.

[34] J. Yang, B. D. Siempelkamp, D. Liu and T. L. Kelly, “Investigation of $CH_3NH_3PbI_3$ degradation rates and mechanisms in controlled humidity environments using in situ techniques,” *ACS Nano,* vol. 9, no. 2, pp. 1955-1963, 2015.

[35] T. Leijtens, G. E. Eperon, S. Pathak, A. Abate, M. M. Lee and H. J. Snaith, “Overcoming ultraviolet light instability of sensitised TiO_2 with meso-superstructured organometal tri-halide perovskite solar cells,” *Nature Communications,* vol. 4, p. 2885, 2013.

[36] S. N. Habisreutinger, T. Leijtens, G. E. Eperon, S. D. Stranks, R. J. Nicholas and H. J. Snaith, “Carbon nanotube/polymer composites as a highly stable hole collection layer in perovskite solar cells,” *Nano Letters,* vol. 14, no. 10, pp. 5561-5568, 2014.

[37] I. C. Smith, E. T. Hoke, D. Solis-Ibarra, M. D. McGehee and H. I. Karunadasa, “A layered hybrid perovskite solar cell absorber with enhanced moisture stability,” *Angewandte Chemie International Edition,* vol. 53, no. 42, pp. 11232-11235, 2014.

[38] A. Dualeh, P. Gao, S. I. Seok, M. K. Nazeeruddin and M. Grätzel, “Thermal behavior of methylammonium lead-trihalide perovskite photovoltaic light harvesters,” *Chemisty of Materials,* vol. 26, no. 21, pp. 6160-6164, 2014.

[39] G. Liu, B. Yang, B. Liu, C. Zhang, S. Xiao, Y. Yuan, H. Xie, D. Niu, J. Yang, Y. Gao and C. Zhou, “Irreversible light-soaking effect of perovskite solar cells caused by light-induced oxygen vacancies in titanium oxide,” *Applied Physics Letters,* vol. 111, no. 15, p. 153501, 2017.

[40] X. Deng, X. Wen, J. Zheng, T. Young, C. F. J. Lau, J. Kim, M. A. Green, S. Huang and A. Ho-Baillie, “Dynamic study of the light soaking effect on perovskite solar cells by in-situ photoluminescence microscopy,” *Nano Energy,* vol. 46, pp. 356-364, 2018.

[41] J. F. Galisteo-López, M. Anaya, M. E. Calvo and H. Miguez, “Environmental effects on the photophysics of organic–inorganic halide perovskites,” *Journal of Physical Chemistry Letters,* vol. 6, no. 12, pp. 2200-2205, 2015.

[42] Y. Tian, M. Peter, E. Unger, M. Abdellah, K. Zheng, T. Pullerits, A. Yartsev, V. Sundström and I. G. Scheblykin, “Mechanistic insights into perovskite photoluminescence enhancement: light curing with oxygen can boost yield thousandfold,” *Physical Chemistry Chemical Physics,* vol. 17, no. 38, pp. 24978-24987, 2015.

[43] S. G. Motti, M. Gandini, A. J. Barker, J. M. Ball, A. R. Srimath Kandada and A. Petrozza, “Photoinduced emissive trap states in lead halide perovskite semiconductors,” *ACS Energy Letters,* vol. 1, no. 4, pp. 726-730, 2016.

[44] H. Zhang, Y. Liu, H. Lu, W. Deng, K. Yang, Z. Deng, X. Zhang, S. Yuan, J. Wang, J. Niu, X. Zhang, Q. Jin, H. Feng, Y. Zhan and L. Zheng, “Reversible air-induced optical and electrical modulation of methylammonium lead bromide ($MAPbBr_3$) single crystals,” *Applied Physics Letters,* vol. 111, no. 10, p. 103904, 2017.

[45] D. Meggiolaro, E. Mosconi and F. De Angelis, “Mechanism of reversible trap passivation by molecular oxygen in lead-halide perovskites,” *ACS Energy Letters,* vol. 2, no. 12, pp. 2794-2798, 2017.

[46] X. Feng, H. Su, Y. Wu, H. Wu, J. Xie, X. Liu, J. Fan, J. Dai and Z. He, “Photon-generated carriers excite superoxide species inducing long-term

photoluminescence enhancement of $MAPbI_3$ perovskite single crystals," *Journal of Materials Chemistry A,* vol. 5, no. 24, pp. 12048-12053, 2017.

[47] G. Niu, W. Li, F. Meng, L. Wang, H. Dong and Y. Qiu, "Study on the stability of $CH_3NH_3PbI_3$ films and the effect of post-modification by aluminum oxide in all-solid-state hybrid solar cells," *Journal of Materials Chemistry A,* vol. 2, pp. 705-710, 2014.

[48] X. Dong, X. Fang, M. Lv, B. Lin, S. Zhang, J. Ding and N. Yuan, "Improvement of the humidity stability organic–inorganic perovskite solar cells using ultrathin Al_2O_3 layers prepared by atomic layer deposition," *Journal of Materials Chemistry A,* vol. 3, pp. 5360-5367, 2015.

[49] A. Dualeh, N. Tétreault, T. Moehl, P. Gao, M. K. Nazeeruddin and M. Grätzel, "Effect of annealing temperature on film morphology of organic–inorganic hybrid pervoskite solid-state solar cells," *Advanced Functional Materials,* vol. 24, no. 21, pp. 3250-3258, 2014.

[50] N. Onoda-Yamamuro, T. Matsuo and H. Suga, "Calorimetric and IR spectroscopic studies of phase transitions in methylammonium trihalogenoplumbates (II)," *Journal of Physics and Chemistry of Solids,* vol. 51, no. 12, pp. 1383-1395, 1990.

[51] B. Conings, J. Drijkoningen, N. Gauquelin, A. Babayigit, J. D'Haen, L. D'Olieslaeger, A. Ethirajan, J. Verbeeck, J. Manca, E. Mosconi, F. De Angelis and H. Boyen, "Intrinsic thermal instability of methylammonium lead trihalide perovskite," *Advanced Energy Materials,* vol. 5, no. 15, p. 1500477, 2015.

[52] A. Pisoni, J. Jaćimović, O. S. Barišić, M. Spina, R. Gaál, L. Forró and E. Horváth, "Ultra-low thermal conductivity in organic–inorganic hybrid perovskite $CH_3NH_3PbI_3$," *Journal of Physical Chemistry Letters,* vol. 5, no. 14, pp. 2488-2492, 2015.

[53] A. Seemann, H.-J. Egelhaaf, C. J. Brabec and J. A. Hauch, "Influence of oxygen on semi-transparent organic solar cells with gas permeable electrodes," *Organic Electronics,* vol. 10, no. 8, pp. 1424-1428, 2009.

[54] M. O. Reese, A. M. Nardes, B. L. Rupert, R. E. Larsen, D. C. Olson, M. T. Lloyd, S. E. Shaheen, D. S. Ginley, G. Rumbles and N. Kopidakis, “Photoinduced degradation of polymer and polymer–fullerene active layers: experiment and theory,” *Advanced Functional Materials,* vol. 20, no. 20, pp. 3476-3483, 2010.

[55] M. Manceau, S. Chambon, A. Rivaton, J.-L. Gardette, S. Guillerez and N. Lemaître, “Effects of long-term UV–visible light irradiation in the absence of oxygen on P3HT and P3HT:PCBM blend,” *Solar Energy Materials and Solar Cells,* vol. 94, no. 10, pp. 1572-1577, 2010.

[56] J. Kim, G. Kim, Y. Choi, J. Lee, S. H. Park and K. Lee, “Light-soaking issue in polymer solar cells: Photoinduced energy level alignment at the sol-gel processed metal oxide and indium tin oxide interface,” *Journal of Applied Physics,* vol. 111, no. 11, p. 114511, 2012.

[57] M. Stoeckel, M. Gobbi, S. Bonacchi, F. Liscio, L. Ferlauto, E. Orgiu and P. Samorì, “Reversible, fast, and wide-range oxygen sensor based on nanostructured organometal halide perovskite,” *Advanced Materials,* vol. 29, no. 38, p. 1702469, 2017.

[58] C. B. Norris and J. F. Gibbons, “Measurement of high-field carrier drift velocities in silicon by a time-of-flight technique,” *IEEE Transactions on Electron Devices,* vol. 14, no. 1, pp. 38-43, 1967.

[59] B. Chen and S. Liu, “Measurement of electron/hole mobility in organic/polymeric thin films using modified time-of-flight apparatus,” *Synthetic Metals,* vol. 91, pp. 169-171, 1997.

[60] E. Lebedev, “Charge carrier mobility in poly(p-phenylenevinylene) studied by the time-of-flight technique,” *Applied Physics Letters,* vol. 71, no. 18, p. 2686, 1997.

[61] B. Chen, C.-s. Lee, S.-t. Lee, P. Webb, Y.-c. Chan, W. Gambling, H. Tian and W. Zhu, “Improved time-of-flight technique for measuring carrier mobility in thin films of organic electroluminescent materials,” *Japanese Journal of Applied*

Physics, vol. 39, pp. 1190-1192, 2000.

[62] D. Shi, V. Adinolfi, R. Comin, M. Yuan, E. Alarousu, A. Buin, Y. Chen, S. Hoogland, A. Rothenberger, K. Katsiev, Y. Losovyj, X. Zhang, P. A. Dowben, O. F. Mohammed, E. H. Sargent and O. M. Bakr, "Low trap-state density and long carrier diffusion in organolead trihalide perovskite single crystals," *Science,* vol. 347, no. 6221, pp. 519-522, 2015.

[63] D. K. Schroder, "Mobility," in *Semiconductor Material and Device Characterisation*, 3rd ed., Wiley-IEEE Press, 2005, pp. 482-484.

[64] Q. Dong, Y. Fang, Y. Shao, P. Mulligan, J. Qiu, L. Cao and J. Huang, "Electron-hole diffusion lengths > 175 μm in solution-grown $CH_3NH_3PbI_3$ single crystals," *Science,* vol. 347, no. 6225, pp. 967-970, 2015.

[65] D. W. de Quilettes, S. M. Vorpahl, S. D. Stranks, H. Nagaoka, G. E. Eperon, M. E. Ziffer, H. J. Snaith and D. S. Ginger, "Impact of microstructure on local carrier lifetime in perovskite solar cells," *Science,* vol. 348, no. 6235, pp. 683-686, 2015.

[66] W. Peng, B. Anand, L. Liu, S. Sampat, B. E. Bearden, A. V. Malko and Y. J. Chabal, "Influence of growth temperature on bulk and surface defects in hybrid lead halide perovskite films," *Nanoscale,* vol. 8, no. 3, pp. 1627-1634, 2016.

[67] K. Handloser, N. Giesbrecht, T. Bein, P. Docampo, M. Handloser and A. Hartschuh, "Contactless visualization of fast charge carrier diffusion in hybrid halide perovskite thin films," *ACS Photonics,* vol. 3, no. 2, pp. 255-261, 2016.

[68] G. W. P. Adhyaksa, L. W. Veldhuizen, Y. Kuang, S. Brittman, R. E. I. Schropp and E. C. Garnett, "Carrier diffusion lengths in hybrid perovskites: processing, composition, aging, and surface passivation effects," *Chemistry of Materials,* vol. 28, no. 15, pp. 5259-5263, 2016.

[69] P. Calado, A. M. Telford, D. Bryant, X. Li, J. Nelson, B. C. O'Regan and P. R. F. Barnes, "Evidence for ion migration in hybrid perovskite solar cells with minimal hysteresis," *Nature Communications,* vol. 7, p. 13831, 2016.

[70] D. Webber, C. Clegg, A. W. Mason, S. A. March, I. G. Hill and K. C. Hall, “Carrier diffusion in thin-film $CH_3NH_3PbI_3$ perovskite measured using four-wave mixing,” *Applied Physics Letters,* vol. 111, no. 12, p. 121905, 2017.

[71] G. Yang, R. A. C. M. M. van Swaaij, S. Dobrovolskiy and M. Zeman, “Determination of defect density of state distribution of amorphous silicon solar cells by temperature derivative capacitance-frequency measurement,” *Journal of Applied Physics,* vol. 115, no. 3, p. 034512, 2014.

[72] S. D. Stranks, V. M. Burlakov, T. Leijtens, J. M. Ball, A. Goriely and H. J. Snaith, “Recombination kinetics in organic-inorganic perovskites: excitons, free Charge, and subgap states,” *Physics Review Applied,* vol. 2, p. 034007, 2014.

[73] L. H. Manger, M. B. Rowley, Y. Fu, A. K. Foote, M. T. Rea, S. L. Wood, S. Jin, J. C. Wright and R. H. Goldsmith, “Global analysis of perovskite photophysics reveals importance of geminate pathways,” *Journal of Physical Chemistry C,* vol. 121, pp. 1062-1071, 2017.

[74] G. Gordillo, C. A. Otálora and M. A. Reinoso, “Trap center study in hybrid organic-inorganic perovskite using thermally stimulated current (TSC) analysis,” *Journal of Applied Physics,* vol. 122, no. 7, p. 075304, 2017.

[75] S. Heo, G. Seo, Y. Lee, D. Lee, M. Seol, J. Lee, J.-B. Park, K. Kim, D.-J. Yun, Y. S. Kim, J. K. Shin, T. K. Ahn and M. K. Nazeeruddin, “Deep level trapped defect analysis in $CH_3NH_3PbI_3$ perovskite solar cells by deep level transient spectroscopy,” *Energy & Environmental Science,* vol. 10, no. 5, pp. 1128-1133, 2017.

[76] M. Samiee, S. Konduri, B. Ganapathy, R. Kottokkaran, H. A. Abbas, A. Kitahara, P. Joshi, L. Zhang, M. Noack and V. Dalal, “Defect density and dielectric constant in perovskite solar cells,” *Applied Physics Letters,* vol. 105, no. 15, p. 153502, 2014.

[77] W. Tress, “Perovskite solar cells on the way to their radiative efficiency limit – insights into a success story of high open-circuit voltage and low recombination,”

Advanced Energy Materials, vol. 7, no. 14, p. 1602358, 2017.

[78] M. Saba, M. Cadelano, D. Marongiu, F. Chen, V. Sarritzu, N. Sestu, C. Figus, M. Aresti, R. Piras, A. G. Lehmann, C. Cannas, A. Misinu, F. Quochi, A. Mura and G. Bongiovanni, "Correlated electron–hole plasma in organometal perovskites," *Nature Communications,* vol. 5, p. 5049, 2014.

[79] C. M. Sutter-Fella, Y. Li, M. Amani, J. W. Ager III, F. M. Toma, E. Yablonovitch, I. D. Sharp and A. Javey, "High photoluminescence quantum yield in band gap tunable bromide containing mixed halide perovskites," *Nano Letters,* vol. 16, no. 1, pp. 800-806, 2016.

[80] J. Blancon, W. Nie, A. J. Neukirch, G. Gupta, S. Tretiak, L. Cognet, A. D. Mohite and J. J. Crochet, "The effects of electronic impurities and electron–hole recombination dynamics on large-grain organic–inorganic perovskite photovoltaic efficiencies," *Advanced Functional Materials,* vol. 26, no. 24, pp. 4283-4292, 2016.

[81] J. S. Manser and P. V. Kamat, "Band filling with free charge carriers in organometal halide perovskites," *Nature Photonics,* vol. 8, pp. 737-743, 2014.

[82] C. Wehrenfennig, M. Liu, H. J. Snaith, M. B. Johnston and L. M. Herz, "Charge-carrier dynamics in vapour-deposited films of the organolead halide perovskite $CH_3NH_3PbI_{3-x}Cl_x$," *Energy & Environmental Science,* vol. 7, no. 7, pp. 2269-2275, 2014.

[83] S. K. Pal, T. Kesti, M. Maiti, F. Zhang, O. Inganäs, S. Hellström, M. R. Andersson, F. Oswald, F. Langa, T. Österman, T. Pascher, A. Yartsev and V. Sundström, "Geminate charge recombination in polymer/fullerene bulk heterojunction films and implications for solar cell function," *Journal of the American Chemical Society,* vol. 132, no. 35, pp. 12440-12451, 2010.

[84] W. Shockley and W. T. Read, Jr., "Statistics of the recombinations of holes and electrons," *Physical Review,* vol. 87, no. 5, pp. 835-842, 1952.

[85] R. N. Hall, “Germanium rectifier characteristics,” *Physical Review,* vol. 83, p. 228, 1951.

[86] R. Schmolke, D. Gräf, R. Kirchner, R. Schauer, N. Werner, E.-P. Mayer and P. Wagner, “Observation of extremely low defect densities in silicon wafers,” *Japanese Journal of Applied Physics,* vol. 38, pp. 1852-1857, 1999.

[87] X. Wen, Y. Feng, S. Huang, F. Huang, Y.-B. Cheng, M. Green and A. Ho-Baillie, “Defect trapping states and charge carrier recombination in organic–inorganic halide perovskites,” *Journal of Materials Chemistry C,* vol. 4, pp. 793-800, 2016.

[88] A. Cuevas and D. Macdonald, “Measuring and interpreting the lifetime of silicon wafers,” *Solar Energy,* vol. 76, pp. 255-262, 2004.

[89] R. A. Sinton and A. Cuevas, “Contactless determination of current–voltage characteristics and minority-carrier lifetimes in semiconductors from quasi-steady-state photoconductance data,” *Applied Physics Letters,* vol. 69, no. 17, pp. 2510-2512, 1996.

[90] M. V. Khenkin, D. V. Amasev, S. A. Kozyukhin, A. V. Sadovnikov, E. A. Katz and A. G. Kazanskii, “Temperature and spectral dependence of $CH_3NH_3PbI_3$ films photoconductivity,” *Applied Physics Letters,* vol. 110, no. 22, p. 222107, 2017.

[91] R. Gottesman, E. Haltzi, L. Gouda, S. Tirosh, Y. Bouhadana, A. Zaban, E. Mosconi and F. De Angelis, “Extremely slow photoconductivity response of $CH_3NH_3PbI_3$ perovskites suggesting structural changes under working conditions,” *Journal of Physical Chemistry Letters,* vol. 5, no. 15, pp. 2662-2669, 2014.

[92] V. Sarritzu, N. Sestu, D. Marongiu, X. Chang, Q. Wang, S. Masi, S. Colella, A. Rizzo, A. Gocalinska, E. Pelucchi, M. L. Mercuri, F. Quochi, M. Saba, A. Mura and G. Bongiovanni, “Direct or indirect bandgap in hybrid lead halide perovskites?,” *Advanced Optical Materials,* vol. 6, no. 10, p. 1701254, 2018.

[93] L. Kong, G. Liu, J. Gong, Q. Hu, R. D. Schaller, P. Dera, D. Zhang, Z. Liu, W. Yang, K. Zhu, Y. Tang, C. Wang, S.-H. Wei, T. Xu and H.-K. Mao, “Simultaneous band-gap

narrowing and carrier-lifetime prolongation of organic–inorganic trihalide perovskites," *PNAS,* vol. 113, no. 32, pp. 8910-8915, 2016.

[94] F. Staub, H. Hempel, J.-C. Hebig, J. Mock, U. W. Paetzold, U. Rau, T. Unold and T. Kirchartz, "Beyond bulk lifetimes: insights into lead halide perovskite films from time-resolved photoluminescence," *Physical Review Applied,* vol. 6, p. 044017, 2016.

[95] T. Duong, D. Grant, S. Rahman, A. Blakers, K. J. Weber, K. R. Catchpole and T. P. White, "Filterless spectral splitting perovskite–silicon tandem system with >23% calculated efficiency," *IEEE Journal of Photovoltaics,* vol. 6, no. 6, pp. 1432-1439, 2016.

[96] J. Peng, Y. Wu, W. Ye, D. A. Jacobs, H. Shen, X. Fu, Y. Wan, T. Duong, N. Wu, C. Barugkin, H. T. Nguyen, D. Zhong, J. Li, T. Lu, Y. Liu, M. N. Lockrey, K. J. Weber, K. R. Catchpole and T. P. White, "Interface passivation using ultrathin polymer–fullerene films for high-efficiency perovskite solar cells with negligible hysteresis," *Energy & Environmental Science,* vol. 10, no. 8, pp. 1792-1800, 2017.

[97] "WITec alpha300 S user manual," WITec, [Online]. Available: https://witec.de/. [Accessed 20 11 2018].

[98] D. W. Bäuerle, "Temperature distributions and surface melting," in *Laser Processing and Chemistry*, 3rd ed., Springer, 2000, pp. 101-135.

[99] M. A. Green, in *Solar cells : operating principles, technology and system applications*, 4th ed., University of New South Wales, 1998, pp. 50-52.

[100] P. Auger, "Sur les rayons β secondaires produits dans un gaz par des rayons X," *C.R.A.S.,* vol. 177, pp. 169-171, 1923.

[101] E.-C. Wang, S. Mokkapati, T. Soderstrom, S. Varlamov and K. R. Catchpole, "Effect of nanoparticle size distribution on the performance of plasmonic thin-film solar cells: monodisperse versus multidisperse arrays," *IEEE Journal of Photovoltaics,* vol. 3, no. 1, pp. 267-270, 2013.

[102] K. Nakayama, K. Tanabe and H. A. Atwater, “Plasmonic nanoparticle enhanced light absorption in GaAs solar cells,” *Applied Physics Letters,* vol. 93, no. 12, p. 121904, 2008.

[103] P. Spinelli, M. Hebbink, R. de Waele, L. Black, F. Lenzmann and A. Polman, “Optical impedance matching using coupled plasmonic nanoparticle arrays,” *Nano Letters,* vol. 11, no. 4, pp. 1760-1765, 2011.

[104] F. J. Beck, E. Verhagen, S. Mokkapati, A. Polman and K. R. Catchpole, “Resonant SPP modes supported by discrete metal nanoparticles on high-index substrates,” *Optics Express,* vol. 19, no. S2, pp. A146-A156, 2011.

[105] N.-G. Park, “Perovskite solar cells: an emerging photovoltaic technology,” *Materials Today,* vol. 18, no. 2, pp. 65-72, 2015.

[106] P. Löper, M. E. Stuckelberger, B. Niesen, J. Werner, M. Filipič, S.-J. Moon, J.-H. Yum, M. Topic, S. De Wolf and C. Ballif, “Complex refractive index spectra of CH3NH3PbI3 perovskite thin films determined by spectroscopic ellipsometry and spectrophotometry,” *Journal of Physical Chemistry Letters,* vol. 6, no. 1, pp. 66-71, 2015.

[107] M. F. Ashby, “Material profiles,” in *Materials and the Environment: Eco-Informed Material Choice*, 2nd ed., Elsevier, 2013, p. 536.

[108] F. Brivio, J. M. Frost, J. M. Skelton, A. J. Jackson, O. J. Weber, M. T. Weller, A. R. Goni, A. M. A. Leguy, P. R. F. Barnes and A. Walsh, “Lattice dynamics and vibrarional spectra of the orthorhombic, tetragonal, and cubic phase of methylammonium lead iodide,” *Physical Review B,* vol. 92, p. 144308, 2015.

[109] S. Kundu and T. L. Kelly, “Improving the moisture stability of perovskite solar cells by using PMMA/P3HT based hole-transport layers,” *Materials Chemistry Frontiers,* vol. 2, no. 1, pp. 81-89, 2018.

[110] W. E. I. Sha, X. Ren, L. Chen and W. C. H. Choy, “The efficiency limit of $CH_3NH_3PbI_3$ perovskite solar cells,” *Applied Physics Letters,* vol. 106, no. 22, p.

221104, 2015.

[111] D. Bi, W. Tress, M. Ibrahim Dar, P. Gao, J. Luo, C. Renevier, K. Schenk, A. Abate, F. Giordano, J.-P. Correa Baena, J.-D. Decoppet, S. M. Zakeeruddin, M. K. Nazeeruddin, M. Grätzel and A. Hagfeldt, "Efficient luminescent solar cells based on tailored mixed-cation perovskites," *Science Advances,* vol. 2, no. 1, p. e1501170, 2016.

[112] G. Xing, N. Mathews, S. S. Lim, N. Yantara, X. Liu, D. Sabba, M. Grätzel, S. Mhaisalkar and T. C. Sum, "Low-temperature solution-processed wavelength-tunable perovskites for lasing," *Nature Materials,* vol. 13, pp. 476-480, 2014.

[113] Y. Shao, Y. Fang, T. Li, Q. Wang, Q. Dong, Y. Deng, Y. Yuan, H. Wei, M. Wang, A. Gruverman, J. Shield and J. Huang, "Grain boundary dominated ion migration in polycrystalline organic–inorganic halide perovskite films," *Energy & Environmental Science,* vol. 9, no. 5, pp. 1752-1759, 2016.

[114] W.-J. Yin, T. Shi and Y. Yan, "Unusual defect physics in $CH_3NH_3PbI_3$ perovskite solar cell absorber," *Applied Physics Letters,* vol. 104, no. 6, p. 063903, 2014.

[115] T. Tachikawa, I. Karimata and Y. Kobori, "Surface charge trapping in organolead halide perovskites explored by single-particle photoluminescence imaging," *Journal of Physical Chemistry Letters,* vol. 6, no. 16, pp. 3195-3201, 2015.

[116] J. Xu, A. Buin, A. H. Ip, W. Li, O. Voznyy, R. Comin, M. Yuan, S. Jeon, Z. Ning, J. J. McDowell, P. Kanjanaboos, J.-P. Sun, X. Lan, L. N. Quan, D. H. Kim, I. G. Hill, P. Maksymovych and E. H. Sargent, "Perovskite–fullerene hybrid materials suppress hysteresis in planar diodes," *Nature Communications,* vol. 6, p. 7081, 2015.

[117] C. Zhao, B. Chen, X. Qiao, L. Luan, K. Lu and B. Hu, "Revealing underlying processes involved in light soaking effects and hysteresis phenomena in perovskite solar cells," *Advanced Energy Materials,* vol. 5, no. 14, p. 1500279, 2015.

[118] K. Wu, A. Bera, C. Ma, Y. Du, Y. Yang, L. Li and T. Wu, "Temperature-dependent

excitonic photoluminescence of hybrid organometal halide perovskite films," *Physical Chemistry Chemical Physics,* vol. 16, no. 41, pp. 22476-22481, 2014.

[119] C. Barugkin, J. Cong, T. Duong, S. Rahman, H. T. Nguyen, D. Macdonald, T. P. White and K. R. Catchpole, "Ultralow absorption coefficient and temperature dependence of radiative recombination of $CH_3NH_3PbI_3$ perovskite from photoluminescence," *Journal of Physical Chemistry Letters,* vol. 6, no. 5, pp. 767-772, 2015.

[120] W. Kong, Z. Ye, Z. Qi, B. Zhang, M. Wang, A. Rahimi-Iman and H. Wu, "Characterization of an abnormal photoluminescence behavior upon crystal-phase transition of perovskite $CH_3NH_3PbI_3$," *Physical Chemistry Chemical Physics,* vol. 17, no. 25, pp. 16405-16411, 2015.

[121] G. A. H. Wetzelaer, M. Scheepers, A. M. Sempere, C. Momblona, J. Ávila and H. J. Bolink, "Trap-assisted non-radiative recombination in organic–inorganic perovskite solar cells," *Advanced Materials,* vol. 27, no. 11, pp. 1837-1841, 2015.

[122] H.-S. Duan, H. Zhou, Q. Chen, P. Sun, S. Luo, T.-B. Song, B. Bob and Y. Yang, "The identification and characterisation of defect states in hybrid organic–inorganic perovskite photovoltaics," *Physical Chemistry Chemical Physics,* vol. 17, no. 1, pp. 112-116, 2015.

[123] A. Baumann, S. Väth, P. Rieder, M. C. Heiber, K. Tvingstedt and V. Dyakonov, "Identification of trap states in perovskite solar cells," *Journal of Physical Chemistry Letters,* vol. 6, no. 12, pp. 2350-2354, 2015.

[124] V. D'Innocenzo, G. Grancini, M. J. P. Alcocer, A. R. Srimath Kandada, S. D. Stranks, M. M. Lee, G. Lanzani, H. J. Snaith and A. Petrozza, "Excitons versus free charges in organo-lead tri-halide perovskites," *Nature Communications,* vol. 5, p. 3586, 2014.

[125] S. Collavini, S. F. Völker and J. L. Delgado, "Understanding the outstanding power conversion efficiency of perovskite-based solar cells," *Angewandte Chemie*

International Edition, vol. 54, no. 34, pp. 9757-9759, 2015.

[126] J. M. Azpiroz, E. Mosconi, J. Bisquert and F. De Angelis, "Defect migration in methylammonium lead iodide and its role in perovskite solar cell operation," *Energy & Environmental Science,* vol. 8, no. 7, pp. 2118-2127, 2015.

[127] C. Eames, J. M. Frost, P. R. F. Barnes, B. C. O'Regan, A. Walsh and M. Saiful Islam, "Ionic transport in hybrid lead iodide perovskite solar cells," *Nature Communications,* vol. 6, p. 7497, 2015.

[128] W. Kong, A. Rahimi-Iman, G. Bi, X. Dai and H. Wu, "Oxygen intercalation induced by photocatalysis on the surface of hybrid lead halide perovskites," *Journal of Physical Chemistry C,* vol. 120, no. 14, pp. 7606-7611, 2016.

[129] S. D. Stranks, G. E. Eperon, G. Grancini, C. Menelaou, M. J. P. Alcocer, T. Leijtens, L. M. Herz, A. Petrozza and H. J. Snaith, "Electron-hole diffusion lengths exceeding 1 micrometer in an organometal trihalide perovskite absorber," *Science,* vol. 342, no. 6156, pp. 341-344, 2013.

[130] G. Xing, N. Mathews, S. Sun, S. S. Lim, Y. M. Lam, M. Grätzel, S. Mhaisalkar and T. C. Sum, "Long-range balanced electron- and hole-transport lengths in organic-inorganic $CH_3NH_3PbI_3$," *Science,* vol. 342, no. 6156, pp. 344-347, 2013.

[131] Y. Zhao, A. M. Nardes and K. Zhu, "Solid-state mesostructured perovskite $CH_3NH_3PbI_3$ solar cells: charge transport, recombination, and diffusion length," *Journal of Physical Chemistry Letter,* vol. 5, no. 3, pp. 490-494, 2014.

[132] Y. Li, W. Yan, Y. Li, S. Wang, W. Wang, Z. Bian, L. Xiao and Q. Gong, "Direct observation of long electron-hole diffusion distance in $CH_3NH_3PbI_3$ perovskite thin film," *Scientific Reports,* vol. 5, p. 14485, 2015.

[133] W. Tian, C. Zhao, J. Leng, R. Cui and S. Jin, "Visualizing carrier diffusion in individual single-crystal organolead halide perovskite nanowires and nanoplates," *Journal of the American Chemical Society,* vol. 137, no. 39, pp. 12458-12461, 2015.

[134] Z. Guo, J. S. Manser, Y. Wan, P. V. Kamat and L. Huang, “Spatial and temporal imaging of long-range charge transport in perovskite thin films by ultrafast microscopy,” *Nature Communications,* vol. 6, p. 7471, 2015.

[135] Y. Li, B. Ding, Q.-Q. Chu, G.-Y. Yang, M. Wang, C.-X. Li and C.-J. Li, “Ultra-high open-circuit voltage of perovskite solar cells induced by nucleation thermodynamics on rough substrates,” *Scientific Reports,* vol. 7, p. 46141, 2017.

[136] G. Landi, H. C. Neitzert, C. Barone, C. Mauro, F. Lang, S. Albrecht, B. Rech and S. Pagano, “Correlation between electronic defect states distribution and device performance of perovskite solar cells,” *Advanced Science,* vol. 4, no. 10, p. 1700183, 2017.

[137] G. Giorgi, J.-I. Fujisawa, H. Segawa and K. Yamashita, “Small photocarrier effective masses featuring ambipolar transport in methylammonium lead iodide perovskite: a density functional analysis,” *Journal of Physcical Chemistry Letters,* vol. 4, pp. 4213-4216, 2013.

[138] Y. Sun, J. Peng, Y. Chen, Y. Yao and Z. Liang, “Triple-cation mixed-halide perovskites: towards efficient, annealing-free and air-stable solar cells enabled by $Pb(SCN)_2$ additive,” *Scientific Reports,* vol. 7, p. 46193, 2017.

[139] G. Gordillo, C. A. Otálora and A. A. Ramirez, “A study of trap and recombination centers in $MAPbI_3$ perovskites,” *Physical Chemistry Chemical Physics,* vol. 18, no. 48, pp. 32862-32867, 2016.

[140] T. Zhao, W. Shi, J. Xi, D. Wang and Z. Shuai, “Intrinsic and extrinsic charge transport in $CH_3NH_3PbI_3$ perovskites predicted from first-principles,” *Scientific Reports,* vol. 6, p. 19968, 2016.

[141] F. Wang, A. Shimazaki, F. Yang, K. Kanahashi, K. Matsuki, Y. Miyauchi, T. Takenobu, A. Wakamiya, Y. Murata and K. Matsuda, “Highly efficient and stable perovskite solar cells by interfacial engineering using solution-processed polymer layer,” *Journal of Physical Chemistry C,* vol. 121, pp. 1562-1568, 2017.

[142] F. Brivio, A. B. Walker and A. Walsh, “Structual and electronic properties of hybrid perovskites for high-efficiency thin-film photovoltaics from first-principles,” *APL Materials,* vol. 1, p. 042111, 2013.

[143] Q. Lin, A. Armin, R. C. R. Nagiri, P. L. Burn and P. Meredith, “Electro-optics of perovskite solar cells,” *Nature Photonics,* vol. 9, pp. 106-112, 2015.

[144] N. K. Noel, A. Abate, S. D. Stranks, E. S. Parrott, V. M. Burlakov, A. Goriely and H. J. Snaith, “Enhanced photoluminescence and solar cell performance via Lewis base passivation of organic–inorganic lead halide perovskites,” *ACS Nano,* vol. 8, no. 10, pp. 9815-9821, 2014.

[145] B. Wu, H. T. Nguyen, Z. Ku, G. Han, D. Giovanni, N. Mathews, H. J. Fan and T. C. Sun, “Discerning the surface and bulk recombination kinetics of organic–inorganic halide perovskite single crystals,” *Advanced Energy Materials,* vol. 6, no. 14, p. 1600551, 2016.

[146] M. A. Green, “Recombination at surfaces,” in *Solar cells: operation principles, technology and system applications*, University of New South Wales, p. 55.

[147] Z.-Y. Zhang, H.-Y. Wang, Y.-X. Zhang, Y.-W. Hao, C. Sun, Y. Zhang, B.-R. Gao, Q.-D. Chen and H.-B. Sun, “The role of trap-assisted recombination in luminescent properties of organometal halide $CH_3NH_3PbBr_3$ perovskite films and quantum dots,” *Scientific Reports,* vol. 6, p. 27286, 2016.

[148] V. K. Khanna, “Physical understanding and technological control of carrier lifetimes in semiconductor materials and devices: A critique of conceptual development, state of the art and applications,” *Progress in Quantum Electronics,* vol. 29, no. 2, pp. 59-163, 2005.